CHARACTERIZATION OF Gd_2O_2S: Tb^{3+} PHOSPHOR POWDER AND THIN FILMS

By

Jappie Jafta Dolo
(MSc)

A thesis submitted in fulfillment of the requirements for the degree

PHILOSOPHIAE DOCTOR

in the

Faculty of Natural and Agricultural Sciences
Department of Physics

at the

University of the Free State
(Bloemfontein)

JUNE 2011

Prof. H.C. Swart (Promoter), Profs. F.B. Dejene and J.J. Terblans
(Co-promoters)

DECLARATION

I declare that the thesis hereby submitted to the University of the Free State for the degree Philosophiae Doctor has not been previously submitted by me for a degree at this or any other University; that it is my work in design and execution, and that all material contained therein has been duly acknowledged.

Jappie Jafta Dolo

Signature **Date**

Dedicated to the memory of the late
MABOKELA IGNATIUS DOLO

ACKNOWLEDGEMENTS

I thank *God* for giving me strength and courage to complete this study.

I am indebted to my promoter, *Prof. Hendrik C. Swart* for his professional guidance and endless support. Most importantly, I thank him for his suggestions in organization of chapters and ideas. Thanks Prof., you are indeed my role model.

I am grateful to my co-promoters *Proffs. J.J. Terblans and B.F. Dejene* for their discussions and advice.

I thank all *staff members of the Department of Physics* (UFS) and post graduate students (in particular, *Mart-Marie Duvenhage and Gugu Mhlongo*) for their assistance and support and also Shaun Cronje for his assistance in annealing of thin films.

I thank *Prof. Martin Ntwaeaborwa* for introducing me to luminescent phosphors, and for his fruitful discussions and guidance in all the papers published from this study.

I am thankful to *Drs. Simon Dhlamini and Liza Coetsee* for introducing me to the degradation of phosphors and the pulsed laser deposition technique and for their continued support for the duration of this study. I also like to thank *Dr Moses Mothudi and Dr D.B. Bem* for their assistance during my research leaves.

I owe a special word of gratitude to my wife *Mapule Dolo* and our daughter *Bokamoso Dolo* for their moral and inspirational support. Without their encouragement and understanding it would have been impossible for me to finish this work. My special gratitude is due to my parents (Salome and late father Ignatius Dolo), my brothers, Jossy, Thabi, Solly, my Sister (Grace) and their respective families for their moral support and encouragement. I would also like to thank my cousin *Pinky Mangope* for putting more efforts and encouragements in this study.

I would also like to thank, *Tsholofelo Mashigo, Mosa Mashigo, Neo Moletsane and Rethabile Moletsane* for their endless support in this study. Entire families of

the in-laws are gratefully acknowledged as well. A special thanks to CSIR (National Laser Center-Pretoria) for allowing me to use their facilities. I am grateful for the financial support from the *South African National Research Foundation*.

ABSTRACT

Under Ultra violet (UV), cathode-ray and X-ray excitation, terbium activated rare earth oxysulphide ($Gd_2O_2S:Tb^{3+}$) phosphors shows bright green luminescence. Due to its superior luminescent performance, $Gd_2O_2S:Tb^{3+}$ phosphor is used in the manufacturing of TV screens. The degradation of commercially available $Gd_2O_2S:Tb^{3+}$ phosphor powder and pulsed laser deposited (PLD) thin films were studied with Auger Electron Spectroscopy (AES) and Cathodoluminescence (CL). The surface reactions were monitored with AES while the light output was measured with a PC2000-UV spectrometer. The CL of the $Gd_2O_2S:Tb^{3+}$ was excited with a 2 keV energy electron beam with a beam current density of 26 mA/cm^2. The CL and AES were measured simultaneously while the sample was bombarded with the electrons in an oxygen atmosphere. A comparison between the low energy peaks of the AES spectra before and after degradation showed significant differences in the shape of the peaks. A linear least squares (LLS) method was applied to resolve the peaks. Elemental standards from Goodfellow were used in conjunction with the measured data to subtract the S and Gd peaks. A direct correlation between the surface reactions and the CL output was found for both the thin films and the powder. The adventitious C was removed from the surface as volatile gas species, which is consistent with the electron stimulated surface chemical reactions (ESSCR) model. The CL decreased while the S was removed from the surface during electron bombardment. A new non-luminescent surface layer that formed during electron bombardment was responsible for the degradation in light intensity. X-ray photoelectron (XPS) indicated that Gd_2O_3 and Gd_2S_3 thin films are formed on the surfaces of the $Gd_2O_2S:Tb^{3+}$ powder and thin films during prolonged electron bombardment.

Luminescent $Gd_2O_2S:Tb^{3+}$ thin film phosphors were successfully grown by the PLD technique. The effects of oxygen pressure and substrate temperature on the morphology and the PL emission intensity were investigated. The films grown in a higher O_2 ambient consist of smaller but more densely packet particles relative to the films grown at a lower O_2 ambient. The PL intensity of the films increased relatively with an increase in deposition O_2 pressure. The PL of the films grown at a higher substrate temperature was generally also more intense than those grown at a lower substrate temperature. It was clear from the Atomic Force Microscopy (AFM) images that spherical nanoparticles were deposited during the deposition process. X-ray diffraction (XRD) indicated that the broadening of the XRD peaks is reduced with an increase in annealing temperature.

KEY WORDS

Cathodoluminescence, degradation, photoluminescence

ACRONYMS

- AES – Auger electron spectroscopy
- APPHs – Auger peak-to-peak heights
- CL – Cathodoluminescence
- PL – Photoluminescence
- PLD – Pulsed laser deposition
- RGA - Residual gas analyser
- TEM – Transmission electron microscopy
- XPS – X-ray photoelectron spectroscopy
- XRD – X-ray diffraction
- ESSCR – Electron stimulated surface chemical reaction
- EDX – Energy dispersive X-ray spectroscopy

TABLE OF CONTENTS

LIST OF FIGURES

CHAPTER 1

Introduction

1.1 Overview

Under UV, cathode-ray and X-ray excitation, Tb^{3+} or Eu activated rare earth oxysulphide phosphors show bright green or red luminescence originating from the activator ions that are distributed in the well-formed crystalline host lattice. Due to their superior luminescent performances, rare earth oxysulphide phosphors are predominatly used in the manufacture of X-ray intensifying screens for medical diagnosis or cathode-ray screens for TV set [1- 4].

By improving illumination, life's activities are significantly prolonged into the night hours, especially by application of PL light from phosphor screens [5]. Life's activities are supported by communication with others. Communication of information has evolved from the faces of rock cliffs, to the walls of caves, clay tablets, parchment, wood and bamboo plates, sheets of paper, magnetic tapes (and disks), and electronic chips. Electronic devices have significantly increased the speed of the communication of information. Information stored on tapes and chips in electronic devices (e.g., TV sets and computers) are invisible to the human eye. Display devices have been developed as an interface between human and electronic devices for the visualization of invisible information in electronic devices [6].

Phosphor utilization depends both on luminescence properties, e.g. luminescence efficiency and colour, and powder characteristics, e.g. particle size and morphology that are regulated during the synthesis stage. High luminescence output and especially well defined morphology (round particles are preferred for their high close-packing ability) and dimension of particle (between 2.5 and 25μm, depending on the screen geometry and image resolution) are the main requirements for rare earth oxysulphide phosphors [7-10].

Field emission displays are one class of displays that aims to replace the existing cathode ray tube. The success of the cathode ray tube lies largely with its bright emissive display capable of depicting sharp dynamic colour images or detailed text and graphics [11]. At the time of writing, the domestic television is a prime example of an application for a cathode ray tube that commands a very high volume of world-wide production. Many of the materials issues relating to cathode ray tubes have been solved to allow units to be mass-produced, inexpensively assembled, and operated for many thousands of hours. The overwhelming disadvantage of the cathode ray tube is its bulkiness. The three electron guns (in the case of a colour cathode ray tube) typically reside farther behind the faceplate than the screen is wide. Although, this ensures the electron beams can raster evenly and accurately across each phosphor-containing pixel to generate the image, it has provided a serious driving force to make more compact display modules [12]. With the appetite for relatively large broad-area domestic high-definition television and space-saving desktop monitors growing, a flat-panel display of similar image specification to the cathode ray tube is urgently required [13].

At the other end of the size scale are the plasma display panels, now finding application as information boards at major transport hubs such as Paddington Railway station in London (UK). These are essentially an array of ‘neon lamps’, generating ultraviolet radiation that excites a phosphor. Their adoption into the

home has been hindered by their high cost, due mainly to the relatively high power electronic circuits needed to control the plasma discharge at each pixel, which make them both expensive to produce and inefficient to operate. Striking bright and stable plasma also becomes problematic as the screen size drops and the pixels necessarily become smaller [14].

Despite these limitations plasma display panel have driven forward the market for broad area displays, and in doing so have solved the problems of fabricating and sealing thin, broad area vacuum tube-like glass vessels [15].

These hurdles need to be leapt at a fantastic rate, as both alternative and established technologies, backed by enormous world-wide investment, are improving daily [16]. There are, of course, numerous contending display technologies with advantages and disadvantages over field emission display, depending on the application for which they are intended [17-18]. They will only be mentioned here in passing, as this is not intended to be the subject of this review. Rather, they will illustrate how significant the progress in materials science and engineering has already been to make quite astonishing electronic display devices a reality. In many cases, these achievements can be applied to the design and manufacture of field emission display. In short, the field emission display has remained a field panel display challenger in the wings for many years, and some commentators have rightly questioned whether they will ever become a widespread solution to the modern display. The primary reason is that, to date, field emission displays have been dogged by fabrication and lifetime issues. This has been particularly apparent when the production of display modules has been scaled up for commercial sale. In addition, the first generation of field emission display have been based around ‘microtip’ technology (to be discussed later), and this has grave processing disadvantages when the format is enlarged to give a broad-area display commensurate with the demands of domestic viewing.

The main flat-panel contenders to the field emission display are liquid crystal displays (LCD's), electroluminescent (EL) displays, and plasma displays panels. To be a true competitor in the field of high information content displays, these technological components must be matrix-addressed to enable individual pixels to be independently controlled. Active matrix (AM) LCDs are by far the most mature of these technologies. They are an incredible feat of micro-engineering made reality by combining the disciplines of chemistry, physics, electronic engineering, process engineering and materials science [19-21]. They comprise of a very flat glass substrate on which optical coatings are disposed (such as the reflector, polariser or analyser), electrodes, passivation layers, alignment layers, the liquid crystalline material, colour filters, and the individual transistor devices (themselves a sandwich of doped semiconductors and electrodes) [22]. To achieve this level of complexity requires a series of vacuum processing steps on highly capital-intensive ultra-clean production lines [23]. Other disadvantages include the need for a back light to make the display emissive and a limited viewing angle. EL technologies [24], including those based on organic light emitting diodes (OLED's) and light emitting polymers (LEP's) [25-26] are promising emissive replacements to AMLCD's. However, for high-information content display modules, they will also require active matrix elements at each sub-pixel [27]. Of particular interest to the field emission display engineer is the plasma display panel [28]. This is a broad-area display built around a glass vacuum envelope containing pixels comprising of small pockets of gas that are electrically excited to create a coloured sub-pixel. The main disadvantage is the high voltage required to strike the plasma and the need to modulate this voltage to generate an image. PDP's are also suited to large format displays (typically greater than 1 m diagonal), as the process of striking plasma in small pixels is inefficient. However, like a field emission display, it does not require an active matrix of transistors, and many of its structural and processing issues have much in common with a field emission display of comparable size [29-30]. Plasma display panels have already

beaten field emission display's to the high-street, although their high cost still inhibits their penetration into the domestic television market. Plasma display panels demonstrate the need for a low-cost field panel display replacement to the CRT and an existence theorem for broad area field panel displays based around evacuated glass envelopes [31].

The practical CL phosphors are empirically selected as the brighter phosphors. They include cub-ZnS:Ag:Cl (blue), cub-ZnS:Cu:Al (green), and Y_2O_2S:Eu (red) in color CRT's, and YP_2S:Eu:Tb^{3+} (white) in black-and-white monochrome cathode ray tubes [32]. We may use those phosphor screens in future cathode ray tubes. The image quality of phosphor screens in cathode ray tubes is predominantly determined by the optical and electrical properties of the bulk phosphor particles in the screen. These properties correlate with irradiation conditions of the electron beam on the phosphor screen, and do not relate to the CL properties generated in the phosphor particles. Although there are many books and review articles devoted to CL phosphors [33-37], there are a limited number of reports on the subject. Furthermore, the phosphor powders are seriously contaminated with the residuals of phosphor production [38], and the surface of each phosphor particle is heavily contaminated with microclusters (insulators), such as SiO_2 (and pigments) to control the screening of phosphor powders on cathode ray tube faceplates. Commercial phosphor powders usually contain some amount of strongly clumped (or bound) particles that generate the defects (pinholes and clumped particles) in the phosphor screen [39].

1.2 Thin film phosphors

A variety of different materials including sulphides, oxides, oxysulphides and aluminates have been used as host matrices for alkali-earth metals or rare-earth elements to synthesize phosphors which are widely used in the lighting industry. Traditionally, a wide variety of phosphors used in the lighting industry were

produced from doping sulphides (e.g. ZnS) with alkali-earth metals (Cu, Ag, etc). Today, trivalent (in some cases divalent) rare-earth elements (Eu^{3+}, Tb^{3+} or Ce^{3+}) are used as activators/dopants of choice in oxide, oxysulphide or aluminate matrices to produce phosphors for a variety of applications. One example of such phosphors is the green emitting terbium (Tb^{3+}) doped gadolinium oxysulphide ($Gd_2O_2S:Tb^{3+}$), which can be used in applications such as flat-panel x-ray imaging in medical diagnosis [40-43] and flat panel communication displays such as colour television and computer screens and other optoelectronic devices. Current fundamental research on $Gd_2O_2S:Tb^{3+}$ is aimed at improving its optical properties for such applications. Although studies of optical properties of $Gd_2O_2S:Tb^{3+}$ phosphors have been reported, the focus has mainly been on the powder form of the phosphor. While it is well known that powders are much brighter than luminescent thin films, thin films have advantages such as superior adhesion to substrates and reduced out gassing over powders. It is therefore equally important to investigate the optical properties of the films as well. The lower luminance of the thin films which is attributed to, among other things, light piping at the phosphor-substrate interface [44], small interaction volume with the incident beam and substrate absorption [45] can be improved by growing films with rougher surfaces, using less absorbing substrates and also by optimizing processing parameters during deposition of the films on the substrates.

The application of powder phosphors on screens raised some serious concerns which include debonding, outgassing and carbon contamination. All these can be eliminated by using thin film phosphors technology [46]. This has resulted in significant interest in the development of thin film phosphors for field emission and plasma-panel displays. Field-emission flat-panel displays require thinner phosphor layers that operate at lower voltages compared to the cathode ray tubes without sacrificing brightness or contrast [47]. Thin films, as opposed to the traditional discrete powder screens, offer the benefit of reduced light scattering, a

reduction of material waste and the potential for fabricating smaller pixel sizes to enhance resolution [47].

1.3 Statement of the problem

A lot of research has been devoted to cathodoluminescence degradation of micro-sized sulphide phosphors since they are used in many display applications including cathode ray tube and field emission display. A mechanism that shows the relationship between their CL degradation and surface chemical reactions has been established. Since these phosphors are not very efficient at low voltages required for field emission displays, micro-sized and nanoparticle oxide phosphors are being investigated to replace them [48]. Several oxysulphide phosphors, for example $Gd_2O_2S:Tb^{3+}$, $Y_2O_2S:Eu^{3+}$, have been investigated for their luminescent properties of thin films. A proper way to evaluate these phosphors for application in low-voltage field emission displays would be to study their luminescent properties including CL and surface degradation during prolonged electron beam exposure. It is important to determine the mechanism that shows the correlation between their CL degradation and changes on the surface chemical composition during electron beam exposure.

It is well known that the reduction in particle size of crystalline systems in the nanometer regime gives rise to some important modifications of their properties with respect to their bulk counterparts. Two main reasons for the change of electronic properties of the nanosized particles can be identified as: (1) the ‘quantum confinement’ effect due to the confinement of delocalized electrons in a small sized particles, which results in an increased electronic band gap and (2) the increase of the surface/volume ratio in nanostructures, which enhances ‘surface’ and ‘interface’ effects over the volume effects. In case of rare-earth ions, the electronic f-f transitions involve localized electrons in the atomic orbital of the ions. Therefore, no size dependent quantum confinement effect is found in the

electronic transitions of the rare-earth doped nanosized particles. However, the 'surface effect' plays a vital role in the photoluminescence properties of these ions. Although there has been an explosive growth in the synthesis of nanosized materials, it is still a challenge for material chemists to design a process for the fabrication of highly luminescent nanosized materials with high degree of crystallinity. Somewhat more recently, the focus of interest has shifted to nanosized luminescent materials with tunable morphologies such as nanorods, nanowires, nanocubes etc [49].

1.4 Research objectives

1. Characterization and degradation of the commercial $Gd_2O_2S:Tb^{3+}$ phosphor powder.
2. Deposition of the $Gd_2O_2S:Tb^{3+}$ phosphor thin films onto Si (100) substrates with the use of a KrF excimer laser in pulsed laser deposition.
3. Characterisation of the thin films with Scanning Electron Microscopy, X-Ray Diffraction, Energy Dispersive X-Ray analysis and Atomic Force Microscopy.
4. Monitor changes in the surface composition and CL, due to electron bombardment of $Gd_2O_2S:Tb^{3+}$ thin films in an O_2 gas ambient, with Auger Electron Spectroscopy and X-ray photo electron spectroscopy.
5. The formulation of a degradation mechanism of $Gd_2O_2S:Tb^{3+}$ thin film and powders under electron bombardment.

1.5 Thesis layout

Chapter 2 provides background information on electronic displays (cathode ray tubes and field emission display), fundamentals of phosphors and luminescence processes such as cathodoluminescence and photoluminescence. Detailed information on energy transfer in phosphors and of cathodoluminescence degradation of sulphide phosphors is also provided.

A summary of surface analysis techniques used in this study is provided in *chapter 3*. This includes a brief description on how each of these techniques work.

Chapters 4 and *5* deal with cathodoluminescence degradation of $Gd_2O_2S:Tb^{3+}$ powder and pulsed laser deposited $Gd_2O_2S:Tb^{3+}$ thin film. Possible mechanisms that relate changes on the surface chemical composition to the decrease of CL intensity are discussed.

A summary of the thesis, conclusion and suggestions for possible future studies are discussed in *chapter 6*.

References

1. H. Degenhardt, Electromed., 3 (1980) 76

2. W. Knuepfer, M. Mengel, U.S. 5126573 (1992) 1

3. G. Blasse, B.C. Grabmaier, Luminescence Material, Springer-Verlag, New York, (1994)

4. S. Shionoya, W.M. Yen, Phosphor Handbook, CRC Press, (1998)

5. K.F. Braun, Ann. Phys. Chem., 60 (1987) 552

6. H. Nalwa and L.S. Rohwer, Eds. Handbook of Luminescence, Display, (1999)

7. Materials and Devices, Vols. 1-3, American Scientific Pub., Stevenson Ranch, CA, (2003)

8. L. Ozawa, Application of Cathodoluminescence to Display Devices, Kodansha, Japan, (1993) 313

9. L. Ozawa and M. Itoh, Chern. Reo., 103 (2003) 2836

10. L. Ozawa, Cathodoluminescence, Theory and Application, Kodansha. Japan, (1990) 237

11. F.A. Kroger, Some Aspects of the Luminescence of Solids, Elsevier, New York, (1948)

12. H.W. Leverentz, An Introduction to Luminescence of Solids, John Wiley & Sons, New York, (1950)

13. D. Curie and G.F.J. Garlick, Luminescence in Crystals, Methuen & Co. Ltd., London, (1960)

14. R.C. Dorf, The Plasma Display Handbook, (1997) 939

15. J.P. Boeuf, J. of Phys. D., 36 (2003) R53

16. M. Balkanski and F Cans, in Luminescence of Organic and Inorganic Materials, (1999)

17. H.P. Kallman and G.M. Spruch, Eds., John Wiley & Sons, New York, (1962), 318

18. S. Shionoya, in Luminescence of Inorganic Solids, P Goldberg, Ed., Academic Press, New York, (1966), chap. 4

19. G.F.J. Garlick, in Luminescence of Inorganic Solids, P Goldberg, Ed., Academic Press, New York, (1966), chap. 12

20. I. Broser, in Physics and Chemistry of II-VI Compounds, M. Aven and S, Prener, Eds., North-Holland, Amsterdam, (1967) 526

21. C.S. Scott and C.E. Reed, Eds., Surface Physics of Phosphors and Semiconductors, Academic Press, New York, (1968)

22. G. Blasse and B.C Grabmaier, Luminescent Materials, Springer-Verlag, Berlin, (1994)

23. S. Shionoya and W.M. Yen, Phosphor Handbook, CRC Press LLC, Boca Raton, 566 (1999) 36

24. P.N. Yocom, J. Soc. Display, 4 (1996) 149

25. M. Yamamoto, J. Soc. lri, Display, 4 (1996) 165

26. L.S. Rohwer, A.M. Srivastava, Electrochem. Soc. Inter., 12 (2), "Luminescence and Display Materials," 2003

27. L. Ozawa, M. Makimura, and M. Itoh, Mater. Chern. Phys., 93 (2005) 481

28. L. Ozawa and M. Itoh, Semiconductor FPD World, 114 (2004) 142

29. N.S. Xu, Y. Tzeng, and R.V. Latham: J. Appl. Phys., 26 (1993) 1776

30. P. J. Marsh, J. Silver, A. Vecht and A. Newport, J. Lumin., 97 (2002) 229

31. S. H. Shin, J. H. Kang, D. Y. Jeon and D. S. Zang, J. Solid State Chem., 178 (2005) 2205

32. D. B. M. Klaassen and D. M. de Leeuw, J. Lumin., 37 (1987) 21

33. M. Pham-Thi and A. Morel, J. Electrochem. Soc., 138 (1999) 1100

34. V.A. Bolchouchine, E.T. Goldburt, B.N. Levonovitch, V.N. Litchmanova, and N.P. Sochtine, J. Lumin., 87 (2000) 1277

35. J.S. Kim, H.L. Park, C.M. Chon, H.S. Moon, and T.W. Kim, Solid State Commun., 129 (2004) 163

36. J. Banga, M. Abboudib, J. Lumin., 106 (2004) 177

37. J.Y. Chen, Y. Shi, J.l. Shi, J. Inorg. Mater., 19 (2004) 1260

38. K.H. Bulter, H.H. Homer, Illum., Eng., 55 (1960) 396

39. F.P. OuYang, B. Tang, Rare Metal Mat. Eng., 32 (2003) 522

40. E-J. Popovici, L. Muresan, A. Hristea-Simoc, E Indrea, M Vasilescu, M. Nazariv, D.Y. Jeon, Opt. Mat., 27 (2004) 559

41. A.A. da Silva, M.A. Cebim, M.R. Davalos, J. Lumin., 128 (2008) 1165

42. S-K Kang, J-K Park, J-Y Choi, B-Y Cha, S-H. Cho, S-H Nam, Nuclear Instruments and Methods in Physics Reseach A, 546 (2005) 242

43. Y. Tian, W-H Cao, X-X Luo, Y. Fu, J. of Alloy Comp., 433 (2007) 313

44. S.L. Jones, D. Kumar, K-G Cho, R Singh, P.H. Holloway, Display, 19 (4) (1999) 151

45. S.Y. Seo, S. Lee, H.D. Park, N. Shin, K-S Sohn, J. Appl. Phys., 9 (2002) 5248

46. R.K. Singh, Z. Chen, D. Kumar, K. Cho, M. Ollinger, Appl. Surf. Sci., 197 (2002) 321

47. J. McKittrick, C.F. Bacalski, G.A. Hirata, K.M. Hubbard, S.G. Pattillo, K.V. Salazar, M. Trkula, J. Am. Ceram. Soc., 83 (2000) 1241

48. T. Haykawa, J. Lumin. 72 (1997) 925

49. O.M. Ntwaeaborwa , Ph.D Thesis, University of the Free State, Bloemfontein, (2006)

CHAPTER 2

Theory on luminescence process based phosphor material

2.1 Introduction

A phosphor is any chemical substance that emits light under UV excitation. They are usually in the form of powders but in some cases, thin films. The impurities that are intentionally introduced in to the material are referred to as activators and the material as the host or matrix. The host material should be transparent enough to enable the transfer of visible light to the surface of the phosphor. Different activators produce deep acceptor levels at distinct depths, which is the main cause for different emission colours of the phosphor. The phosphor material used in this study was commercially available gadolinium oxysulphide doped with Tb^{3+} as a rare earth metal ($Gd_2O_2S:Tb^{3+}$).

Phosphor utilization depends on the luminescent properties (e.g luminescence efficiency and colour) and the powder characteristics (e.g particle size and morphology) that are regulated during the synthesis stage. Furthermore, Popovici et al. [1] reported on the general characterization of the $Gd_2O_2S:Tb^{3+}$ phosphor. The majority of the specially conditioned phosphor samples possesses free-flowing properties, is white smoke or light-beige in colour and exhibits green luminescence under ultraviolet excitation. However, it was mentioned that the powder colour is influenced by the presence of residual metallic sulphides that, by

their dark colour, could drastically deteriorate the PL performances. In this chapter we provide background information on fundamentals of phosphors and luminescence processes such as cathodoluminescence and photoluminescence. Degradation of oxysulphide phosphors is also provided.

2.2 Emission of light in a phosphor by a CL process

When an energetic electron is incident on a phosphor, a number of physical processes occur. These include emission of secondary electrons, Auger electrons and back-scattered electrons. Hundreds of free electrons and free holes are produced along the path of the incident electron (primary electron). As illustrated in figure 2.1, recombination of an e-h pair results in the emission of a photon. This energy is then adsorbed by the activator.

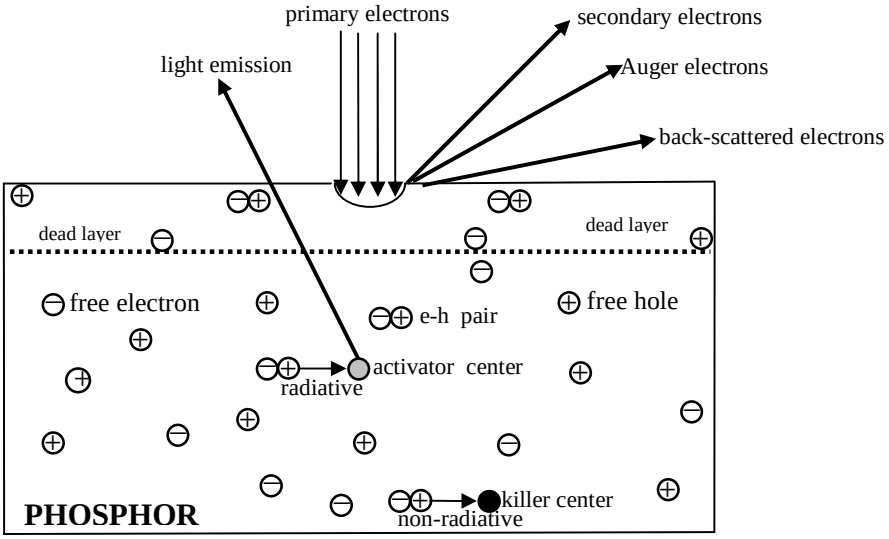

Figure 2.1: CL process in a phosphor grain [2]

The e-h pairs can diffuse through the phosphor and transfer e-h energy to activator ions and subsequently emit light [2-3]. This process is referred to as radiative recombination. Unwanted process in which the e-h pairs recombine non-radiatively by transferring their energy to killer centres (incidental impurities and inherent lattice defects) is also possible. The e-h pair can also diffuse to the surface of the phosphor and recombine non-radiatively [2]. A thin "dead" (non-luminescent) layer may be formed on the surface.

2.3 Cathodoluminescence degradation

Cathodoluminescence intensity of Cathode ray tube/field emission display phosphor is known to degrade drastically due to prolonged exposure to a beam of electrons. Degradation of the CL intensity of phosphors has been a subject of interest since the 1960s. It is defined as a reduction (quenching) of luminescence efficiency of phosphors during electron beam or photon exposure [3]. There are two kinds of effects that contribute to the CL degradation. These are (1) the presence of a killer (incidental impurities or lattice defects) and (2) thermal quenching (an increase in temperature) [3].

2.4 Killers

Killers are defects caused by incidental impurities (adsorbed atoms or molecules) as well as defects that are inherent to the lattice. The impurities adsorbed at the surface may quench cathodoluminescence by producing a non-luminescent surface layer [3] when they react with ambient vacuum species. There are two ways in which killers can quench luminescence of phosphors. First, bypassing killers are capable of capturing free carriers in competition with luminescent centres during diffusion of the free carriers produced by excitation, allowing them to recombine non-radiatively. Second, ionization of impurity atoms may quench luminescence

when competing with intra-ionic radiative transitions during resonant energy transfer processes [4].

2.5 Thermal quenching

Thermal quenching refers to reduction in luminescence of a radiative recpmbination centre due to an increase in temperature. It occurs at high temperatures when thermal vibrations of atoms surrounding the luminescent centre transfer energy away from the centre resulting in a non-radiative recombination, and a subsequent depletion of the excess energy as phonons in the lattice [5]. Thermal quenching process can be described in terms of the configurational coordinate model of a luminescent centre shown in figure 2.2.

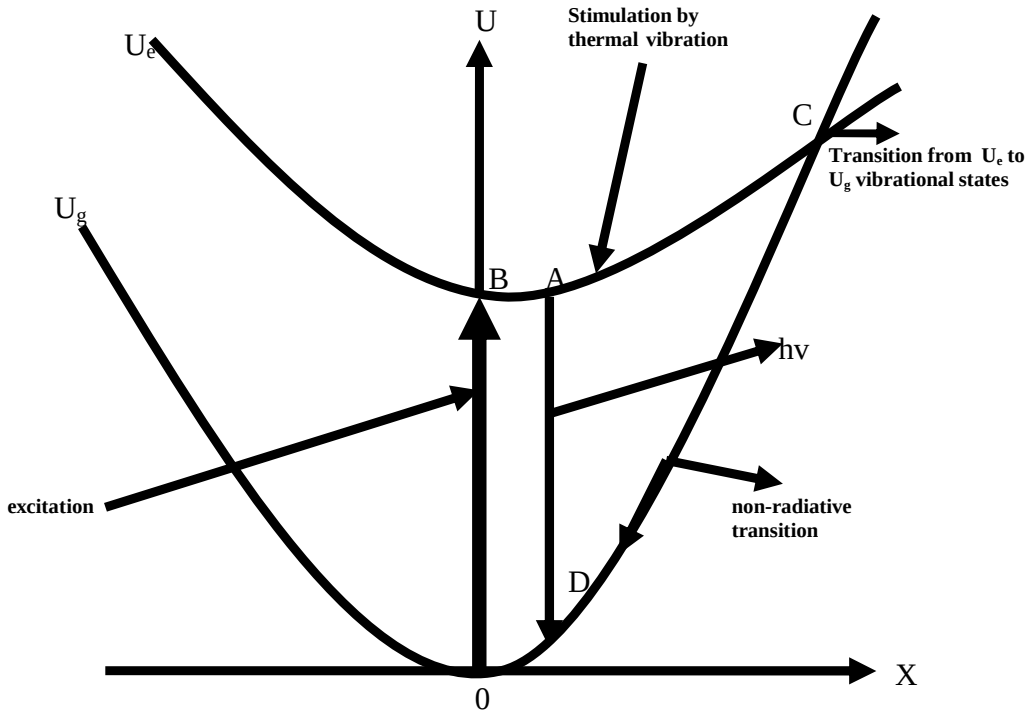

Figure 2.2: Configurational coordinate model of a luminescent centre [6]

The U_g and U_e in figure 2.2 represent the energies of luminescent centres in the ground state and in the excited state, respectively. If the centre is optically excited, the system undergoes a vertical transition from the stable ground state (point O on the U_g) to the excited state (point B on the U_e). This transition causes the system to adapt to the new equilibrium situation by changing its atomic configuration from B to the new equilibrium (A) along the curve U_e, with excess energy dissipated as heat. In a short while, the system undergoes a vertical jump, a radiative transition, from A - D, emitting the energy difference between the two states as radiation. This transition is then followed by the slower rearrangement of the atomic configuration from A - 0 along U_g, with excess energy dissipated as heat. If the system temperature is too high, the luminescent centre can be stimulated from A - C along U_e. The centre may transit, at the crossing point C, from the vibration state of the excited state to a different vibration state of the ground state O, with the vibration energy dissipated into the host lattice. Thus, the non-radiative relaxation from A competes at high temperatures with a radiative transition from A - D, causing thermal quenching of emission [7].

2.6 Electron stimulated surface chemical reaction (ESSCR)

A mathematical model of an ESSCR developed by Holloway et. al. [8] shows the correlation between degradation of CL intensity and the depletion of sulphur (S) from the surface of ZnS:Cu,Al,Au and ZnS:Ag,Cl powder phosphors. According to this model, the concentration of S on the surface, C_S, can be represented by a standard chemical rate equation:

$$\frac{dC_S}{dt} = -kC_S C_{as}^n, \qquad (2.1)$$

where k is a chemical rate constant, C_{as}^{n} is the concentration of the adsorbed atomic species that will react with ZnS, n is the order of the surface reaction; and the first order surface reactions are assumed [9]. Assuming that the reaction takes place on the surface, C_{as} can be expressed as:

$$C_{as} = Z\phi_{ma} C_m J \tau_{as}, \qquad (2.2)$$

where Z is the number of reactive atomic species produced from the parent molecule, ϕ_{ma} is the dissociation cross section of the molecule to atoms, C_m is the surface concentration of the molecular species, J is the current density causing the dissociation, and τ_{as} is the lifetime of a reactive atomic species [9]. C_m controls the rate of production of C_{as} and can be expressed as:

$$C_m = \sigma(\tau_o \, e^{Q/kT})(\frac{P_m}{\sqrt{2\pi mkT}}), \qquad (2.3)$$

where σ is the molecular sticking coefficient and the first term in brackets is the molecular mean stay time on the surface, while the second term in brackets is the molecular flux onto the surface. τ_o is the mean time between attempts by the adsorbed molecule to escape from the surface, Q is the energy required to desorb from the surface, k is Boltzman's constant, T is absolute temperature, and P_m is the partial pressure of the molecular gas in the vacuum. Substituting equations (2.2) and (2.3) into (2.1) gives:

$$\frac{dC_s}{dt} = -k\sigma C_s Z\phi_{ma} J \tau_{as} (\tau_o \, e^{Q/kT})(\frac{P_m}{\sqrt{2\pi mkT}}). \qquad (2.4)$$

Equation (2.4) may be written as

$$\frac{dC_s}{C_s} = -K'JP_m dt, \tag{2.5}$$

where K′ is defined by

$$K' = k\sigma Z\phi_{ma}\tau_{as}(\tau_o e^{Q/kT})(\sqrt{2\pi mkT}). \tag{2.6}$$

Integrating equation (2.6) with respect to time yields

$$C_s = C_s^0 e^{-K'P_m Jt}, \tag{2.7}$$

where the boundary conditions of $C_s = C_s^0$ at time equal to zero were applied and the product Jt is the electron density. Jt is equal to coulomb per unit area or the electron dose, also known as the coulombic dose [6]. This model predicts that the concentration of S will decrease exponentially with coulombic dose, and the rate of loss will be larger at higher gas pressures. Since the C_S and the CL intensity are correlated, equation (2.7) can be written in terms of the CL intensity, I_{CL}, as

$$I_{CL} = I_{CL}^0 e^{-K'P_m Jt} \tag{2.8}$$

The study of degradation of sulphide phosphors such as ZnS:Cu,Al,Au, ZnS:Ag,Cl and Y_2O_2S:Eu showed a direct correlation between the decrease of CL intensity and changes in the surface chemistry during prolonged exposure to a beam of electrons. These changes suggest that electron beam stimulated surface chemical reactions are occurring.

2.7 Energy transfer in phosphors

The process of energy transfer in phosphors involves interaction between two luminescent centres referred to as the sensitizer (energy donor) and the activator (energy acceptor). The interaction can be an exchange interaction (e.g. spectral or wave function overlap) or an electric or a magnetic multipolar interaction [10]. Energy transfer can occur between a pair of identical luminescent centres (e.g. two identical rare-earth ions) or between two non-identical centres. Energy transfer between two identical centres, especially two identical rare-earth ions, has been an issue of research for the past two decades. In this study, energy transfer was evaluated between non-identical centres.

The process of energy transfer between two non-identical centres, a sensitizer/energy donar (D) and an energy acceptor (A) separated by a distance R in a phosphor, is illustrated in figure 2.3. (Excited sensitizer atom can transfer its excitation to a neighbouring acceptor atom, via an intermediate virtual photon)

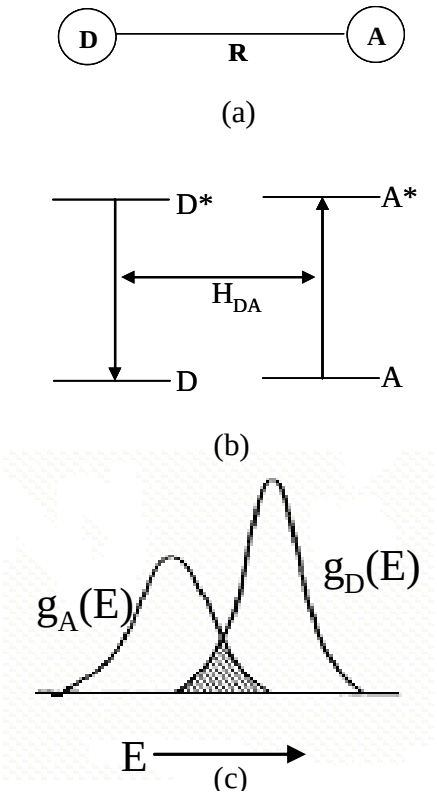

Figure 2.3: (a) Two centers D and A separated by a distance R, (b) energy transfer between D and A, and (c) the overlap between D emission and A absorption spectra [10]

Energy transfer can only occur if the energy differences between the ground states and the excited states of D and A are equal and if a suitable interaction (e.g. spectral or wavefunction overlap) exists between the centres [10]. The rate of energy transfer (P_{DA}) between D and A is given by [10]:

$$P_{DA} = \frac{2\pi}{\hbar} \left| < D, A^* \left| H_{DA} \right| D^*, A > \right|^2 \cdot \int g_D(E).g_A(E) dE, \qquad (2.10)$$

where the matrix element represents the interaction between the initial state $\left| D^*, A > \right.$ and the final state $\left. < D, A^* \right|$. H_{AD} is the interaction Hamiltonian and D^* and A^* are the excited states of D and A. The integral represents the spectral overlap between D emission and A absorption where $g_x(E)$ is the normalized optical line function of center x (x = D or A). D^* can decay to the ground state non-radiatively by transferring energy to A with a rate P_{DA} (transfer rate) or radiatively with a rate P_D (radiative rate). The critical distance (R_c) for energy transfer is defined as the distance for which P_{DA} equals P_D. For $R > R_c$, radiative emission from D prevails, and energy transfer from D to A dominates for $R < R_c$ [10].

2.8 Luminescence mechanism

Luminescent materials, also called phosphors, are mostly solid inorganic materials consisting of a host lattice, usually intentionally doped with impurities (see Fig. 2.3) [11]. The impurity concentrations generally are low in view of the fact that at higher concentrations the efficiency of the luminescence process usually decreases (concentration quenching, see below). In addition, most of the phosphors have a white body color. Especially for fluorescent lamps, this is an essential feature to prevent absorption of visible light by the phosphors used [11]. The absorption of energy, which is used to excite the luminescence, takes place by either the host lattice or by intentionally doped impurities. In most cases, the emission takes place

on the impurity ions, which, when they also generate the desired emission, are called activator ions [11]. When the activator ions show too weak an absorption, a second kind of impurity can be added in sensitizers, which absorb the energy and subsequently transfer the energy to the activators. This process involves transport of energy through the luminescent materials. Quite frequently, the emission color can be adjusted by choosing the proper impurity ion, without changing the host lattice in which the impurity ions are incorporated. On the other hand, quite a few activator ions show emission spectra with emission at spectral positions which are hardly influenced by their chemical environment. This is especially true for many of the rare-earth ions [11].

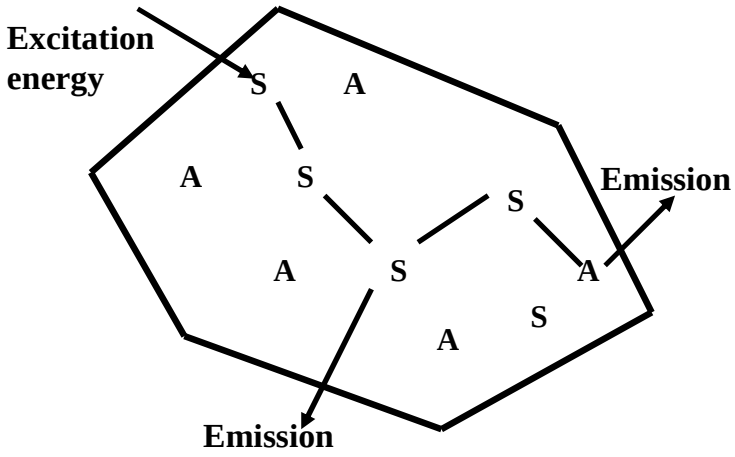

Figure 2.4: Luminescence material containing activator ions A (ions showing the desired emission) and sensitizing ions S (on which, e.g UV excitation can take place) [11]

2.9 Cross relaxation process

A phenomenon not discussed until now is cross-relaxation. In such a process, which can also be looked upon as energy transfer, the excited ion transfers only part of its energy to another ion. For two Tb^{3+} ions, the process is depicted in Fig. 2.5 [12]. In this case, the energy difference between the $^5D_3$ and $^5D_4$ excited states matches approximately the energy difference between the $^7F_6$ ground state and higher ^7F_J states. As in the energy transfer processes discussed above, at large Tb-Tb distances, the process of cross-relaxation has a low rate. In many host lattices, therefore, at low Tb^{3+} concentration, emission from both the $^5D_3$ and $^5D_4$ excited states is observed (unless the gap between these two states is bridged by phonon emission, for which relatively high-energy phonons are required, which is, for example, the case with $Gd_2O_2S:Tb^{3+}$) [12]. The resulting emission spectrum has emission from the near UV into the red part of the optical spectrum. At higher Tb^{3+} concentrations (in the order of five percent), cross-relaxation quenches the emission from the $^5D_3$ level in favor of emission originating from the $^5D_4$ level, implying that it is not possible to obtain blue Tb^{3+} emission in luminescent materials with higher Tb^{3+} concentrations. Cross-relaxation also occurs for other ions. It quenches blue Eu^{3+} emission even at relatively low Eu^{3+} concentrations (<1 %) in favor of the well-known red emission. In case of ions like Sm^{3+} and Dy^{3+}, cross-relaxation leads to quenching of the visible emission. This seriously limits the applicability of these ions [12].

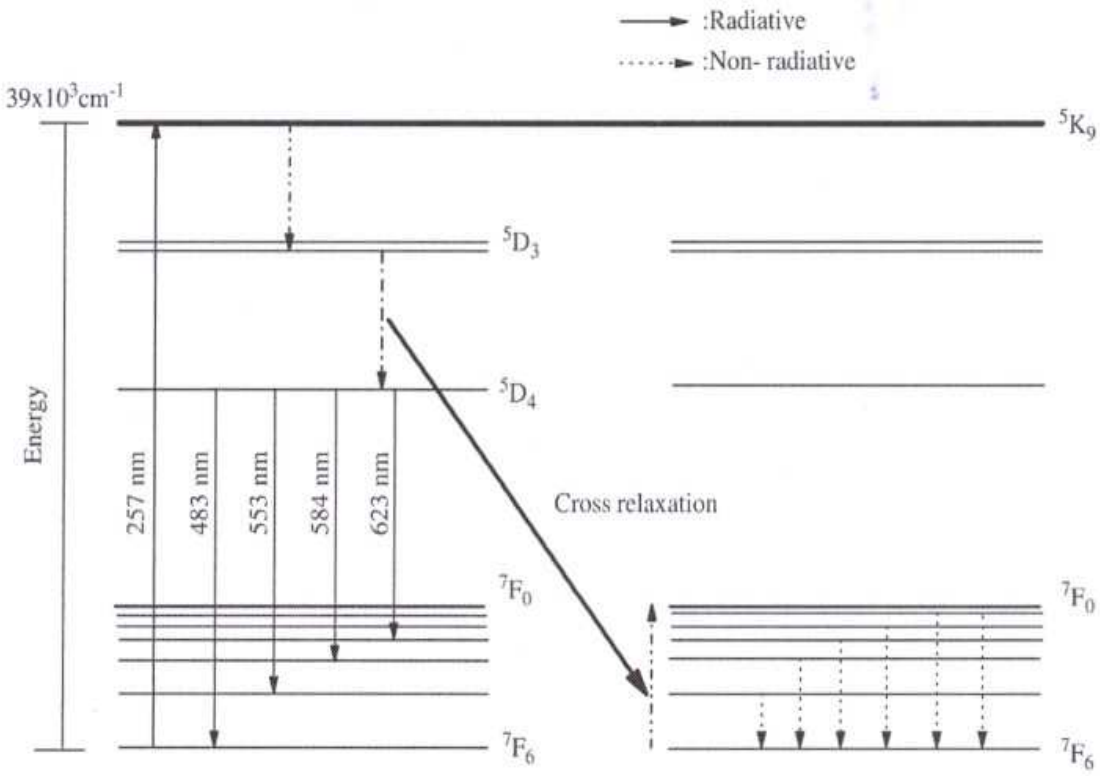

Figure 2.5: Cross-relaxation between two Tb^{3+} ions [12]

2.10 Factors determining the emission colour

Many luminescent ions show emission at different wavelengths in different host lattices. This phenomenon, once understood, opens up the possibility to change, within certain limits, the emission color. In this way, the emission spectra (and excitation spectra) can be tuned toward the specifications required. In cases where at least one of the electronic states is involved in the chemical bonding, the coupling to the lattice has to be taken into account. This situation is encountered for many transition metal ions, for the S_2 ions, and for rare-earth ions showing d→f emission [13]. In figure 2.6, this situation is illustrated for d→f optical

transition on Eu^{2+}. Other rare-earth ions showing d→f emission are Ce^{3+}, Pr^{3+}, Nd^{3+} and Er^{3+}, albeit for the last three ions only in the UV. The energy difference between the d- and f-electrons is modified by the covalence of the Eu^{2+}-ligand bond and the crystal field strength. An increase of the covalence of the Eu^{2+}-ligand bond results in a lower energy difference of the 4f-5d energy separation (due to the nephelauxetic effect). The nephelauxetic effect is a term used in the physical chemistry of transition metals. It refers to a decrease in the Racah interelectronic repulsion parameter, given the symbol B, that occurs when a transition metal free ion forms a complex with ligands. The name comes from the Greek for cloud-expanding. This elementary treatment considers the shift of the center of gravity (also called barycenter) of the d-electron level (also called centroid shift), i.e. any splitting is not yet taken into account [13].

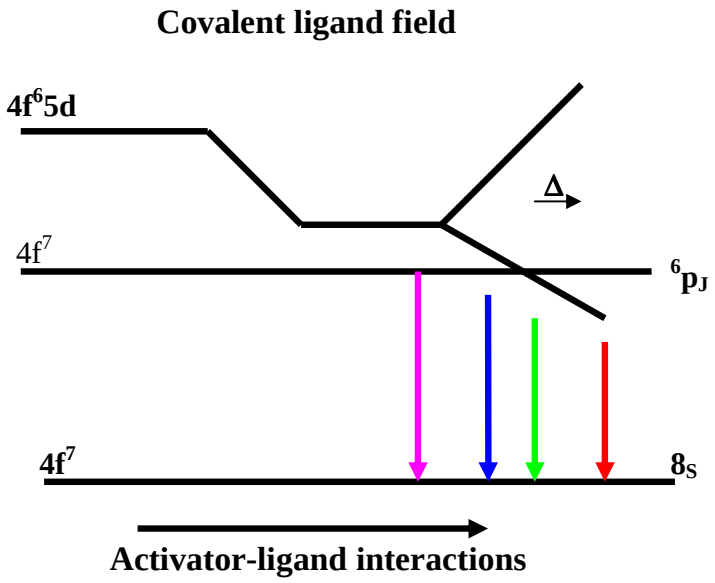

Figure 2.6: Energy separation of the $4f^7$ and $4f^65d^1$ bands as a function of covalence and ligand field strength. The arrows indicate different emission colors [13]

The crystal field interaction splits the d-level, depending on symmetry and crystal field strength. In this way, e.g., for Eu^{2+}, emission can be obtained extending from the UV part of the optical spectrum [13]. Both are easily accessible by choosing appropriate host lattices, and for this reason broad-band emitters can in general be tuned within a large spectral range and can be adapted to the application needs. The spectral position of the emission lines due to transitions between f-electronic states does not vary very much on changing the host lattice. However, the relative emission intensity of the several possible optical transitions does vary considerably. As a general remark, one can state that in cases where the rare-earth ion occupies a site with inversion symmetry, the selection rule states: $\Delta J = 0, 1$. In cases where $\Delta J = 0$, any transition to another state with $J = 0$ is forbidden as well. In such a case, $\Delta|J|$ is necessarily +1 [13]. These are all magnetic dipole transitions. In lattices without inversion symmetry there is also electric dipole emission. For these transitions, the selection rule is: $\Delta|J| \leq 6$. Here again, for initial or final states with $J = 0$, other selection rules are operative. In such a case, for electric dipole transitions, $\Delta | J | = 2, 4$, or 6. We observe that the presence of an inversion center opens up the possibility to tune the emission spectrum to a small extent. For Eu^{3+} with excited state $^5D_0$, the emission can be tuned from orange (590 nm, with inversion symmetry, $^5D_0 \rightarrow {}^7F_1$ transition) to red (610 nm, without inversion symmetry, $^5D_0 \rightarrow {}^7F_2$ transition). More generally, these effects can be described by the Judd-Ofelt theory [14-15]. As a function of three parameters, all possible spectra can be calculated. However, a direct coupling to the chemical environment is lacking. Nevertheless, such calculations are useful. Apart from being able to calculate the relative intensities, these calculations can also be used to calculate subsequent optical transitions, i.e. quantum cutters. For Pr^{3+}, in principle a quantum efficiency of 198 % can be obtained in the visible. The same kind of calculation has shown that for Tm^{3+}, no quantum cutter, a yield of two visible photons can be obtained [15].

Finally, in the case of donor-acceptor pair luminescence, both the donors and the acceptors and the magnitude of the band gap strongly influence the spectral position of the emission color to be obtained. ZnS:Ag and ZnS:Cu,Au (blue- and green-emitting phosphors, respectively, nicely illustrate this) [15].

2.11 Fluorescence

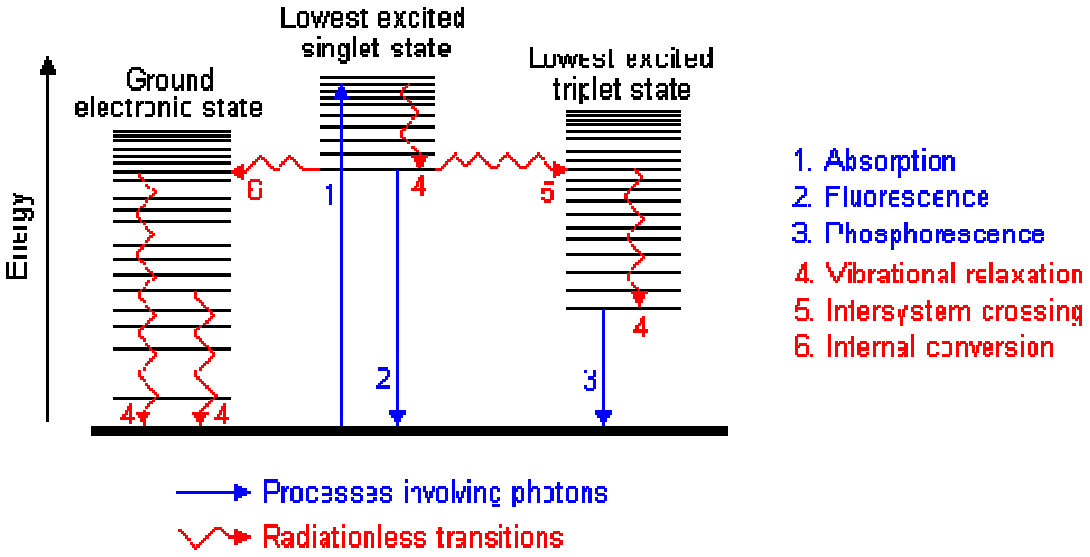

Figure 2.7: Possible physical process following absorption of a photon by a molecule [16]

Absorption of UV radiation by a molecule excites it from a vibrational level in the electronic ground state to one of the many vibrational levels in the electronic excited state in figure 2.7. This excited state is usually the first excited singlet state. A molecule in a high vibrational level of the excited state will quickly fall to the lowest vibrational level of this state by losing energy to other molecules through collision. The molecule will also partition the excess energy to other possible modes of vibration and rotation. Fluorescence occurs when the molecule returns to the electronic ground state, from the excited singlet state, by emission of

a photon. If a molecule which absorbs UV radiation does not fluoresce it means that it must have lost its phonon energy in some other way. These processes are called radiationless emission in the form of a phonon [16].

The spin of an excited electron can be reversed, leaving the molecule in an excited triplet state; this is called intersystem crossing. The triplet state is of a lower electronic energy than the excited singlet state. The probability of this happening is increased if the vibrational levels of these two states overlap. For example, the lowest singlet vibrational level can overlap one of the higher vibrational levels of the triplet state. A molecule in a high vibrational level of the excited triplet state can lose energy in collision with solvent molecules, leaving it at the lowest vibrational level of the triplet state. It can then undergo a second intersystem crossing to a high vibrational level of the electronic ground state. Finally, the molecule returns to the lowest vibrational level of the electronic ground state by vibrational relaxation [16].

References

1. M. Nazarov, B. Tsukerblat, C. Chisu Byeon, I. Arellano, E.J. Popovici, D.Y. Noh Opt. Mater., 27 (2004) 559

2. C. Stoffers, S.Yang, S.M. Jacobsen and C.J. Summers, Saturation of phosphor under low voltage excitation, Proceedings for the First International Conference on the Science and Technology of Display Phosphors, San Diego, Nov. (1995)

3. T. Hase, T. Kano, E. Nakazawa and H. Yamamoto, Advances in Electronics and Electrophys., 79 (1990) 271

4. M. Godlewski and M. Skowronski, Phys. Rev. B., 32 (1985) 4007

5. W. Park, B.K. Wagner, G. Russell, K. Yasuda and C.J.J. Summers, J. Mater. Res., 15 (11) (2000) 2288

6. K.T. Hillie, PhD Thesis, University of the Free State, South Africa (2001)

7. R. Raue, A.T. Vink and T. Welker, Phillips Tech. Rev., 44 (12) (1989) 335

8. P.H. Holloway, T.A. Trottier, J. Sebastian, S. Jone, X-M. Zhang, J-S Bang, B. Abrams, W.J. Thomes and T-J. Kim, J. Appl. Phys., 88 (2000) 1

9. A. Pfahnl, in Advances in electron tube techniques, Pergamon, New York, (1961) 204

10. G. Blasse and B.C. Grabmaier, Luminescence Material, Springer-Verlag, Berlin, (1994)

11. D.L. Dexter, J. Chem. Phys., 21 (1953) 836

12. R.H. Bartram, A. Lempicki, J. Lumin., 69 (1996) 225

13. A. Meijerink, J. Nuyten, G. Blasse, J. Lumin., 44 (1989) 19

14. G.S. Ofelt, J. Chem. Phys., 37 (1962) 511

15. B.R. Judd, Phys. Rev., 127 (1962) 750

16. K.J.B.M. Nieuwesteeg, Res., 44 (1989) 383

CHAPTER 3

Research and experimental techniques

3.1 Introduction

A wide variety of surface analysis techniques were used to study degradation, morphology and crystallinity of oxide-based powder and thin film phosphors. These include Auger electron spectroscopy, x-ray photoelectron spectroscopy, x-ray diffraction, Fourier transform infrared spectroscopy and scanning electron microscopy. In addition, the pulsed laser deposition technique was used to grow thin luminescent films. The Auger electron spectroscopy and the X-ray photoelectron spectroscopy were used to monitor the elemental composition on the surfaces of powder and thin film phosphors during electron or x-ray bombardment, respectively. Scanning electron microscopy was used to obtain information about the morphology of powder phosphors. X-ray diffraction was used to identify crystalline phases of powder samples and the Fourier transform infrared spectroscopy was used to identify and/or verify compounds synthesized by a sol-gel process. This chapter provides an introductory overview of some of the techniques used in this study.

The thin films investigated in this research were prepared by pulsed laser deposition.

Theory on the PLD technique, SEM, EDX, XRD, PL, CL, AES and XPS can be found in this chapter as well as the experimental procedure.

3.2 Auger Electron Spectroscopy

Auger electron spectroscopy is a common analytical technique used specifically in the study of surfaces and, more generally, in the area of materials science [1]. Underlying the spectroscopic technique is the Auger effect, as it has come to be called. This technique is based on the analysis of energetic electrons emitted from an excited atom after a series of internal relaxation events. The Auger effect was discovered independently by both Lise Meitner and Pierre Auger in the 1920s. Though the discovery was made by Meitner and initially reported in the journal Zeitschrift für Physik in 1922, Auger is credited with the discovery in most of the scientific community [1]. Until the early 1950s Auger transitions were considered nuisance effects by spectroscopists, not containing much relevant material information, but studied so as to explain anomalies in x-ray spectroscopy data. Since 1953 however, AES has become a practical and straightforward characterization technique for probing chemical and compositional surface environments and has found applications in metallurgy, gas-phase chemistry, and throughout the microelectronics industry [2-5]. An emitted electron will have a kinetic energy of:

$$E_k = E_{\text{Core State}} - E_B - E_C' \tag{3.1}$$

where E_{Core} State, E_B, $E_{C'}$ are the core level, first outer shell, and second outer shell electron energies respectively, measured from the vacuum level.

The types of state-to-state transitions available to electrons during an Auger event are dependent on several factors, ranging from initial excitation energy to relative interaction rates, yet are often dominated by a few characteristic transitions. Due to the interaction between an electron's spin and orbital angular momentum (spin-orbit coupling) and the concomitant energy level splitting for various shells in an atom, there are a variety of transition pathways for filling a core hole. Energy

levels are labeled using a number of different schemes such as the j-j coupling method for heavy elements (Z ≥75), the Russell-Saunders L-S method for lighter elements (Z< 20), and a combination of both for intermediate elements [3-7]. The j-j coupling method, which is historically linked to X-ray notation, is almost always used to denote Auger transitions. Thus for a KL1L2,3 transition, K represents the core level hole, L1 the relaxing electron's initial state, and L2,3 the emitted electron's initial energy state. Figure 3.1(b) illustrates this transition with the corresponding spectroscopic notation. The energy level of the core hole will often determine which transition types will be favoured. For single energy levels, i.e. K, transitions can occur from the L levels, giving rise to strong KLL type peaks in an Auger spectrum. Higher level transitions can also occur, but are less probable. For multi-level shells, transitions are available from higher energy orbitals (different n,l quantum numbers) or energy levels within the same shell (same n, different l number) [2]. The results are transitions of the type LMM and KLL along with faster Coster–Kronig transitions such as LLM [2-3]. It should be noted that while Coster–Kronig transitions are faster, they are also less energetic and thus harder to locate on an Auger spectrum. As the atomic number Z increases, so too does the number of potential Auger transitions. Fortunately, the strongest electron-electron interactions are between levels which are close together, giving rise to characteristic peaks in an Auger spectrum. KLL and LMM peaks are some of the most commonly identified transitions during surface analysis [3]. Finally, valence band electrons can also fill core holes or be emitted during KVV-type transitions.

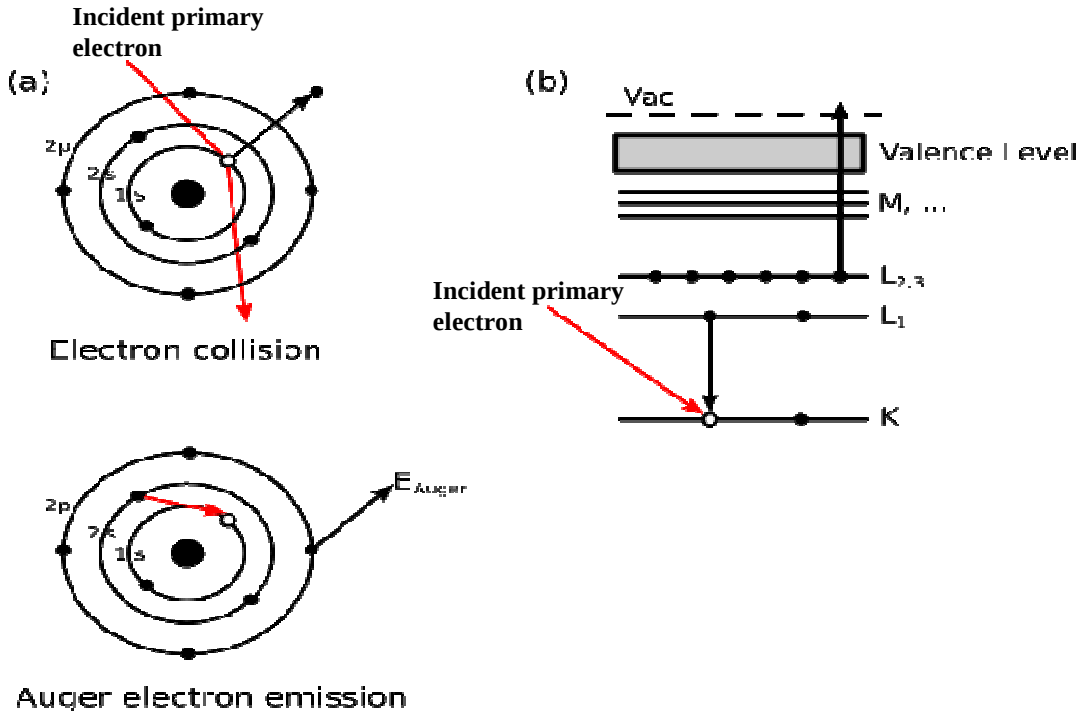

Figure 3.1: Two views of the Auger process. (a) Illustrates sequentially the steps involved in Auger de-excitation and (b) illustrates the same process using spectroscopic notation, $KL_1L_{2,3}$ [1]

The essential components of an AES spectrometer are an ultra high vacuum (UHV) chamber, electron gun, electron energy analyzer and electron detector [8]. Figure 3.2 shows the PHI model 549 Auger spectrometer used in this study.

Figure 3.2: The PHI model 549 Auger spectrometer

3.3 X-Ray Photoelectron Spectroscopy

X-ray photoelectron spectroscopy, also known as electron spectroscopy for chemical analysis (ESCA), is a widely used surface technique to obtain chemical information at surfaces of various materials. The XPS process involves the ejection of an electron (photoelectron) in vacuum from the K level of an atom by an energetic incident x-ray photon [3]. Photoelectrons are collected and analyzed to produce a spectrum of emission intensity versus electron binding energy. In general, the binding energies of the photoelectrons are characteristic of the element from which they are emitted [9]. The schematic of the XPS process is shown in figure 3.3.

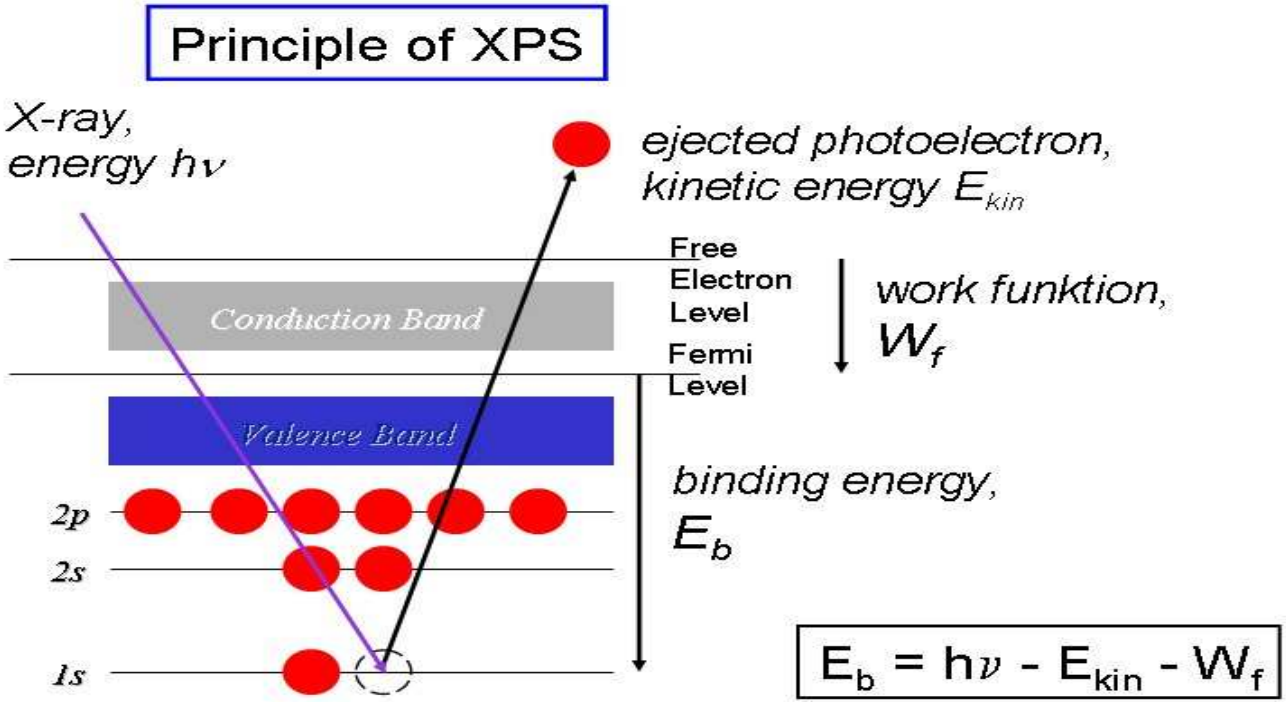

Figure 3.3: Schematic diagram of the XPS process in copper [10]

The kinetic energy (E_{Kin}) of the ejected photoelectron is dependent on the energy of the incident photon (hv) according to the following equation [10]:

$$E_{kin} = hv - \Phi - E_b \qquad (3.2)$$

Where hv is the x-ray photon energy, E_b is the binding energy of the photoelectron in the parent atom and Φ is the work function of the target material. The low kinetic energy (0 - 1500 eV) of emitted photoelectrons limit the depth from which it can emerge and this means that the X-ray photospectroscopy is a very surface-sensitive technique [9]. The basic components of a X-ray photospectroscopy are an x-ray source, electron energy analyzer for the photoelectrons, and an electron detector. The XPS spectrometer used in this study was the PHI 5000 Versaprobe, shown in figure 3.4, from the University of the Free State, Department of Physics (Bloemfontein).

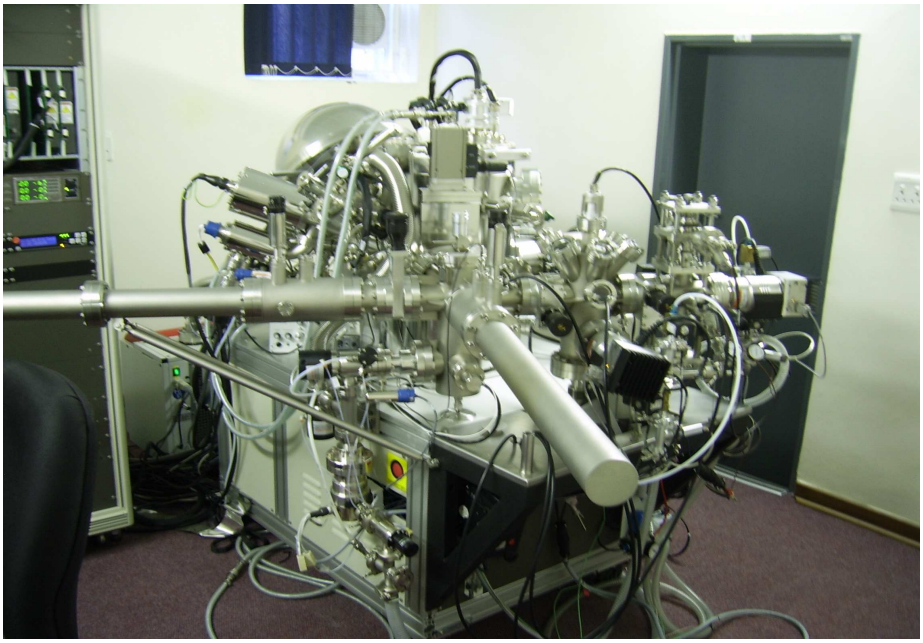

Figure 3.4: PHI 5400 Versaprobe scanning x-ray photoelectron spectrometer

3.4 Scanning Electron Microscopy

Scanning electron microscopy is a technique in which a beam of finely focused electrons is used to examine materials on a nanometer to micrometer scale. The examination can yield information about topography, morphology, composition and crystallography of materials [9]. When a beam of primary electrons impinges the surface of a sample, it generates low energy secondary electrons. The intensity of these secondary electrons is governed by the surface topography of the sample. An image of the sample surface is therefore constructed by measuring secondary electron intensity as a function of the position of the scanning primary electron beam [9]. In this study, the SEM images of powder and thin film samples were obtained using Leo-Field Emission Scanning Electron Microscope Gemini LEO 1525 model to determine the surface morphology. (see figure 3.5) from the University of the Free State (Centre of Confocal and Electron microscopy).

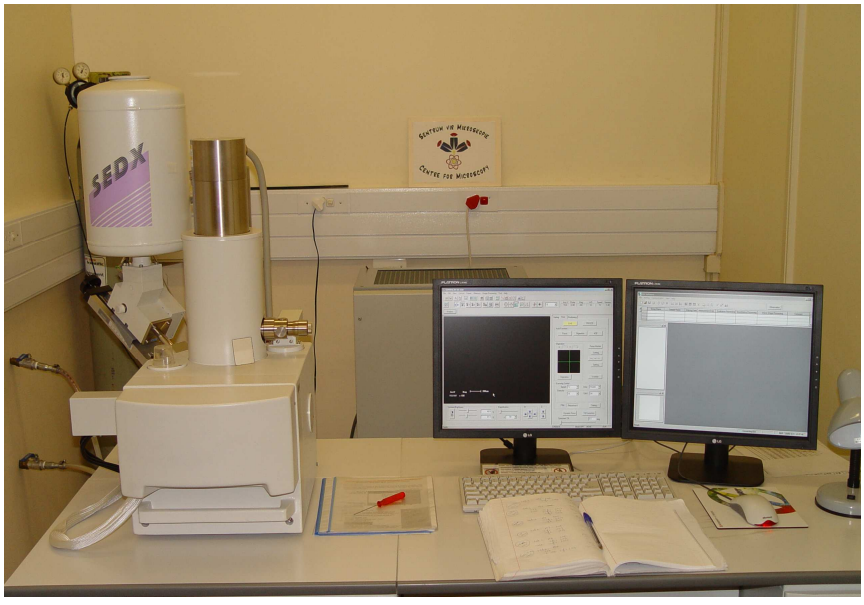

Figure 3.5: Leo-Field Scanning Electron Microscope

3.5 X-Ray Diffraction

X-ray Diffraction is a powerful non-destructive technique used to investigate structural properties of crystalline materials. It can be used in applications such as phase identification, determination of grain size, composition of solid solution, lattice constants, and degree of crystallinity in a mixture of amorphous and crystalline substances [9]. A diffraction pattern is produced when a material is irradiated with a collimated beam of x-rays. The X-ray diffractometer used in this study was Philips SAM003A model X-ray diffractometer, shown in figure 3.6, from the Geology department of the University of the Free State.

Figure 3.6: Philips SAM003A model x-ray diffractometer

3.6 Atomic Force Microscopy

AFM is the acronym for Atomic Force Microscopy or Atomic Force Microscope and is often called the "Eye of Nanotechnology". AFM, also referred to as SPM or Scanning Probe Microscopy, is a very high-resolution type of scanning probe microscopy, with demonstrated resolution on the order of fractions of a nanometer, more than 1000 times better than the optical diffraction limit. It allows researchers to observe and manipulate molecular and atomic level features [11]. The atomic force microscope is one of about two dozen types of scanned-proximity probe microscopes, used to study surface topography and morphology. All of these microscopes work by measuring a local property - such as height, optical absorption, or magnetism - with a probe or "tip" placed very close to the sample. The small probe -sample separation (on the order of the instrument's resolution) makes it possible to take measurements over a small area [12]. AFM works by bringing a cantilever tip in contact with the surface to be imaged, as shown in figure 3.7. An ionic repulsive force from the surface applied to the tip bends the cantilever upwards. The amount of bending, measured by a laser spot reflected on to a split photo detector can be used to calculate the force. By keeping the force constant while scanning the tip across the surface, the vertical movement of the tip follows the surface profile and is recorded as the surface topography by the AFM.

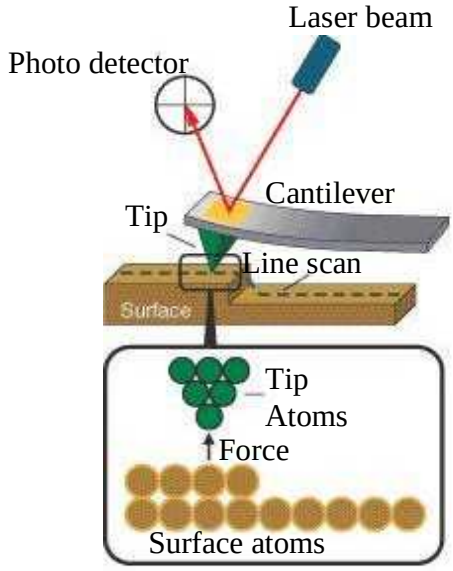

Figure 3.7: Schematic diagram of the AFM operated in repulsive contact mode [13]

3.7 Pulsed Laser Deposition (PLD)

The history of pulsed laser deposition (PLD) started, when Smith and Turner [13] demonstrated films deposited from materials ablated using a ruby laser. Various semiconductor, oxide and chalcogenide films with varying quality have been produced. However, strong attention to the pulsed laser deposition has been attracted only when it has been demonstrated, that this technique is suitable for deposition of complex compounds like $YBa_2Cu_3O_7$ (YBCO), which was considered a promising high temperature superconductor [14]. The principle of PLD is quite simple. Due to the deposited energy when a pulsed laser beam is focused onto a material it is evaporated, it is expanded from the target surface and is deposited on a substrate placed on the opposite side. Ablation is carried out in vacuum or reduced ambient atmosphere, since the ablated material cannot reach the substrate under atmospheric pressure. In spite of the simplicity of the general idea and its realization processes occurring during ablation and deposition are quite complex. Up to now some of them are not fully understood and most are

difficult to describe analytically. Thus, most of the research in this area is empirical. The deposition process can be separated into several stages: ablation, plasma plume expansion, deposition onto a substrate, nucleation and formation of the film structure. The ablation process depends strongly on the properties of the target material and surface quality as well as on characteristic of laser radiation. The laser radiation is absorbed by electronic subsystem and then the energy is transferred to the lattice. In case of oxides (insulators) free electrons first need to be produced. It occurs as a result of one or several mechanisms: linear absorption, multiphoton absorption, impact avalanche ionization. Depending on the time scale, either the dissociation of material can take place, when a certain free electron density is exceeded (laser-induced breakdown), or energy is transferred from electrons to lattice, so that thermal melting and evaporation occur. The former scheme take place, when pulse duration is less than the time constant of energy transfer from electrons to the lattice ($\tau < \tau_{e\text{-}ph}$). $\tau_{e\text{-}ph}$ is typically in the picosecond range, thus is true for femtosecond and picosecond pulses. The latter case occurs for longer pulses ($\tau > \tau_{e\text{-}ph}$), including the nanosecond radiation used in this work. Thus, gaseous or, more often, partly ionized material (plasma) is formed and expands from the target. The evaporation is very fast, plasma is not thermalized and expansion has an ultrasonic character. This plasma can also absorb some part of the laser radiation and thus further influence the course of the ablation process. The plume is usually very strong, which might result in difficulties when directed for large area coatings. Individual species in the plasma plume has energies up to 100 eV. This feature of PLD is often utilized to produce crystalline films even at relatively low substrate temperatures. Ambient gas plays a crucial role in the plume expansion process. It can be used to reduce the velocities of plasma species and partly thermalize the plume. Reactive atmosphere is often used to prevent the deficiency of some volatile component, e.g. oxygen. In the case of nanosecond pulses, not completely evaporated, liquid droplets can be desorbed from the target. Loosely attached solid particles can also be dislodged

due to stress produced by ablation. These droplets or macro particles deposited on the substrate (termed particulates) are one of the major issues of the PLD technique, since they degrade the quality of the fabricated films. A number of processes take place, when plume species reach the substrate surface. Depending on their energy, they are adsorbed at the surface or are implanted into the volume of material. Subsequently diffusion and recrystallization processes take place which are usually stimulated by heating of the substrate. When particle energies are too high, they can result in destruction of the already formed film and even desorption of film material. Depending on process parameters and the interaction between substrate and arriving plume species, film formation can occur in different regimes. Typically three such regimes are distinguished: (1) layer-by-layer growth, when previous layer is completed before the growth of the next one starts; (2) island growth, first three-dimensional islands are formed, and only afterwards they grow together to form a continuous film; (3) mixed mode, first some monolayers are formed and then island growth start to prevail. Generally, due to the high kinetic energy, particles on the surface have enough mobility. Therefore growth of crystalline films is relatively easy to achieve for the PLD process. The evaporated particles form a plume that expands towards the substrate, adhering onto it, see figure 3.8.

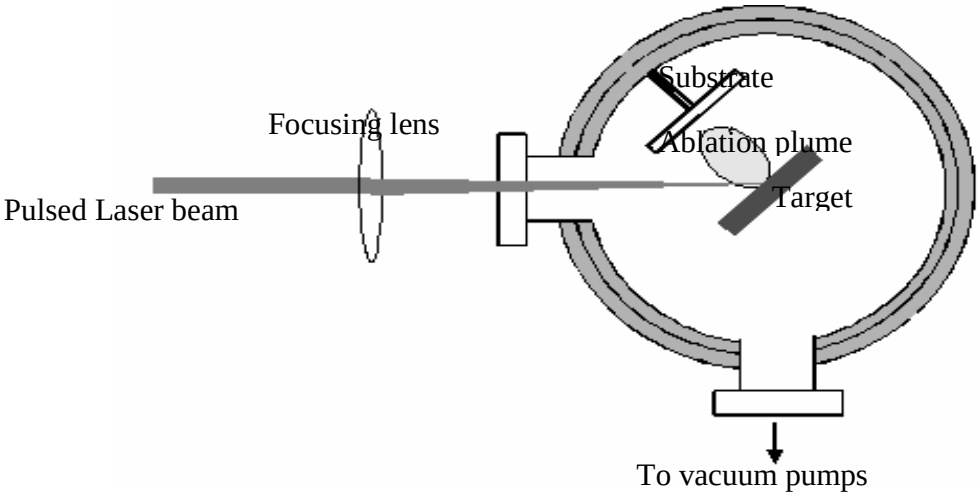

Figure 3.8: Schematic diagram of the PLD technique [15]

Figure 3.9: 248 nm KrF Lambda Physic excimer laser with PLD setup

References

1. J.T. Grant, Surface Analysis by Auger and X-ray Photoelectron Spectroscopy. Chichester: IM Publications (2003)

2. A. Thomas, Carlson Photoelectron and Auger Spectroscopy. New York: Plenum Press (1975)

3. D. Briggs, P.M. Seah, Practical Surface Analysis by Auger and X-ray Photoelectron Spectroscopy. Chichester: John Wiley & Sons (1983)

4. M. Thompson, M.D. Baker, A. Christie, and J.F. Tyson, Auger Electron Spectroscopy. Chichester: John Wiley & Sons (1985)

5. L.E. Davis, Modern Surface Analysis: Metallurgical Applications of Auger Electron Spectroscopy (AES) and X-ray Photoelectron Spectroscopy (XPS). Warrendale: The Metallurgical Society of AIME (1980)

6. C. Kittel, Introduction to Solid State Physics (7th ed.). New York: John Wiley & Sons (1996)

7. N. Ashcroft, N. Mermin, Solid State Physics. Ithaca: Thomson Learning (1976)

8. A. Settle, Handbook of Instrumental Techniques for Analytical Chemistry, Prentice Hall, New Jersey, (1997)

9. Hong Kong Baptist University: www.hkpu.edu.hk/~csar/fesem.html [Accessed 9 October 2007]

10. G.C. Smith, Surface Analysis by Electron Spectroscopy, Plenum Press, New York, (1994)

11. Atomic Force Microscopy, [online]. Available from www.molec.com/ what_is_afm.html [Accessed 22 February 2006]

12. The tip-sample interaction in atomic force microscopy and its implications for biological applications ", Ph.D. thesis by David Baselt, California Institute of Technology (1994)

13. H. M. Smith and A. F. Turner, Vac. Appl. Opt., 4 (1965) 147

14. D. Dijkamp, T. Venkatesan, X. D. Wu, S. A. Shaheen, N. Jisrawi, Y. H. Min-Lee, W. L. McLean, and M. Croft, Appl. Phys. Lett., 51 (1987) 619

15. Pulsed Laser Deposition, [online]. Available from http://www.esrf.fr/UsersAndScience/Experiments/CRG/BM25/inhouseresearch/supportlaboratory/PLD [16 August 1996]

CHAPTER 4

Characterization and degradation of commercial $Gd_2O_2S:Tb^{3+}$ phosphor powder

4.1 Introduction

Terbium doped gadolinium oxysulfide ($Gd_2O_2S:Tb^{3+}$), one of the rare earth oxysulfide group of phosphors, is known to be an efficient phosphor and has been put to practical use for cathodoluminescent and X-ray application for its high conversion efficiency (12–25%) of the exciting radiation [1-3]. $Gd_2O_2S:Tb^{3+}$ is a well-known green-emitting photoluminescence and cathodoluminescence phosphor used in high resolution and projection television screens [4-7].

We report on the characterization of commercial terbium doped gadolinium oxysulfide ($Gd_2O_2S:Tb^{3+}$) phosphor and the degradation of the $Gd_2O_2S:Tb^{3+}$ green phosphor for its application in CRT screens. As a result, degradation of the cathodoluminescence (CL) intensity during irradiation of the powder with 2 keV electrons in an oxygen pressure of 1×10^{-6} Torr was studied. The Linear Least Square (LLS) method was used to determine the relative contribution of Gd and S to the measured low energy Auger Peak to Peak Height (APPH).

4.2 Experimental

The commercially available phosphor powders, obtained from phosphor Technology, were characterized by PL spectroscopy, X-ray diffraction measurements, Scanning electron microscopy, Energy-dispersive X-ray spectroscopy and Transmission electron microscopy analysis. The powder was degraded under prolonged electron bombardment. AES and CL spectroscopy were used to monitor changes on the surface and the corresponding decrease of the CL intensity during electron bombardment of the green phosphor $Gd_2O_2S:Tb^{3+}$. The AES measurements were taken in an UHV chamber using a PHI model 549 Auger spectrometer. The chamber was first evacuated to 2.8 $x10^{-9}$ Torr before backfilled with oxygen to $1x10^{-6}$ Torr. The CL data for the peak intensity at λ = 550 nm, were collected for 20 hr with a PC2000-UV Spectrometer type using OOI Base32 computer software. Both Auger and CL measurements were taken simultaneously with the same electron beam of energy 2 keV and a beam current density of 26 $mA.cm^{-2}$. Due to peak overlapping in the AES data a linear least squares (LLS) method was applied to resolve the peaks. Elemental standards from Goodfellow and Phosphor Technology were used in conjunction with the measured data to subtract the S and Gd peaks. The standards were sputtered clean with 2 keV Ar^+ ions. The Gd standard was also oxidized at 1 x 10^{-7} Torr. Spectra were drawn before and after oxidation of the Gd standard. The oxidized Gd was used as the standard for Gd_2O_3 in the LLS fits. Residual gas mass analyses (RGA) were performed to determine the volatile gas species during electron bombardment, by using an Anavac-2 mass analyzer.

4.3 Results and discussion

4.3.1 Characterization of $Gd_2O_2S:Tb^{3+}$ phosphor powder

The crystal structure of Gd_2O_2S is shown in figure 4.1, where Gd is 7 coordinated by 3 sulfur and 4 oxygen atoms. The crystal structure of gadolinium oxysulfide has trigonal symmetry and the space group $P3_{ml}$ with one formula unit per unit cell. The lattice constants are a = 3.8558 Å and c = 6.6700 Å. Each Gd atom is coordinated by four oxygen atoms and three sulfur atoms in a non-inversion symmetric arrangement. It was reported that sulfur atoms form layers perpendicular to the crystallographic c-axis. So, the Gd_2O_2S structure can be described by the sulfur layers with double layers of gadolinium and oxygen in between [8].

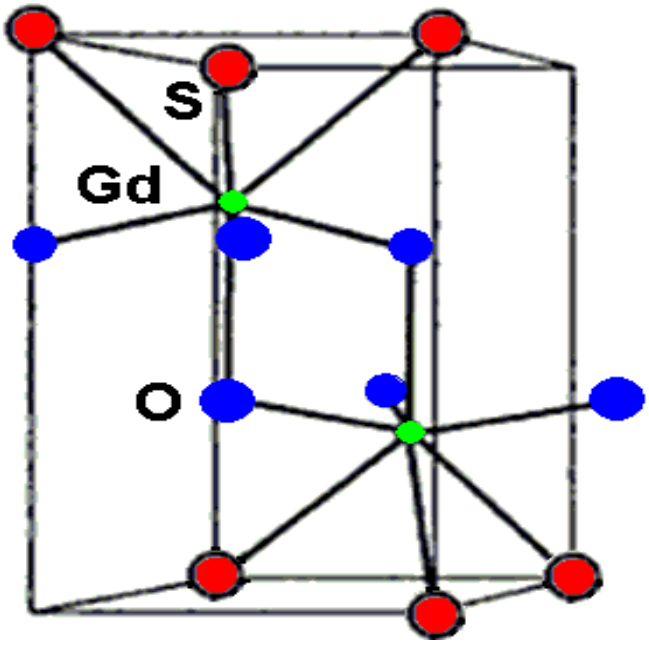

Figure 4.1: The crystal structure of Gd_2O_2S (where Gd is 7 coordinated by 3 sulfur and 4 oxygen atoms)

The crystalline structure of the $Gd_2O_2S:Tb^{3+}$ phosphor was determined by XRD as shown in figure 4.2. The insert is the XRD spectra of the $Gd_2O_2S:Tb^{3+}$ prepared by the Solid State Reaction (SSR) [9] technique which shows a similar spectrum. The

results are in good agreement with Popovici et al [5]. It is well known that, the small size of the crystallites, the lattice strains and lattice imperfections as well as the experimental diffraction geometry could cause the XRD line broadening [5].

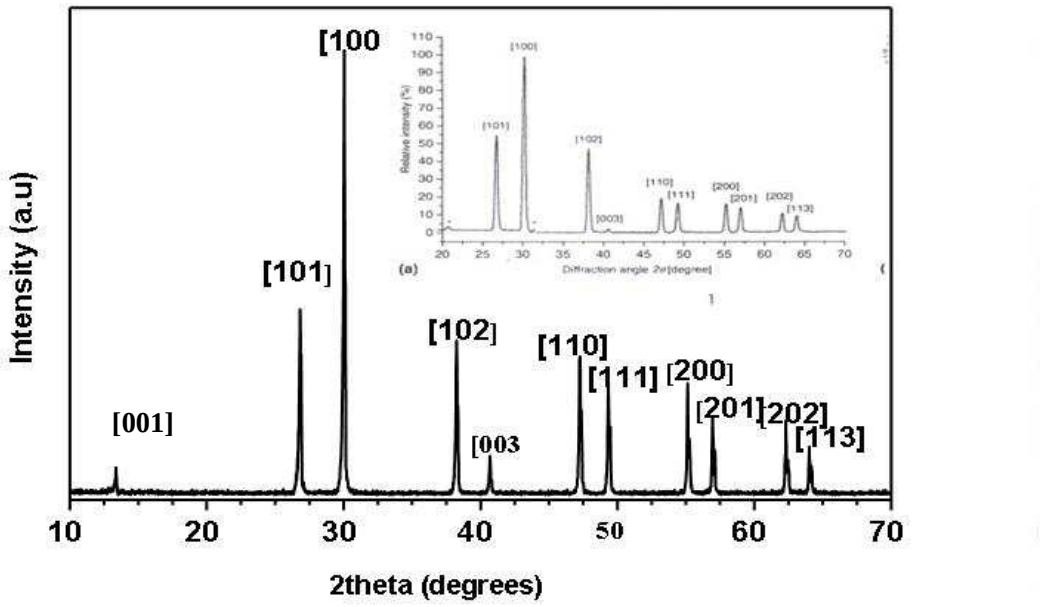

Figure 4.2: XRD pattern for the $Gd_2O_2S:Tb^{3+}$ phosphor powder. Inset is the XRD pattern for $Gd_2O_2S:Tb^{3+}$ phosphor powder prepared by solid state reaction route

SEM images of the commercially available $Gd_2O_2S:Tb^{3+}$ phosphor powder was taken to determine the surface morphology. Figures 4.3(a) shows the SEM image of the powder with magnification of 10000. The particles are polyhedron in shape, showing relatively good for the close packing requirement for the CRT or X-ray intensifying screens and it differs in size and shapes. The sizes differ from 1 µm to 6 µm. Figure 4.3 (b) shows that some of the particles have agglomerated at magnification of 2000. EDS data in figure 4.4 confirms the presence of all the elements (Gd, O and S) together with the adventitious carbon. Tb^{3+} ions were not detected probably due to their relatively low concentration in the $Gd_2O_2S:Tb^{3+}$ matrix.

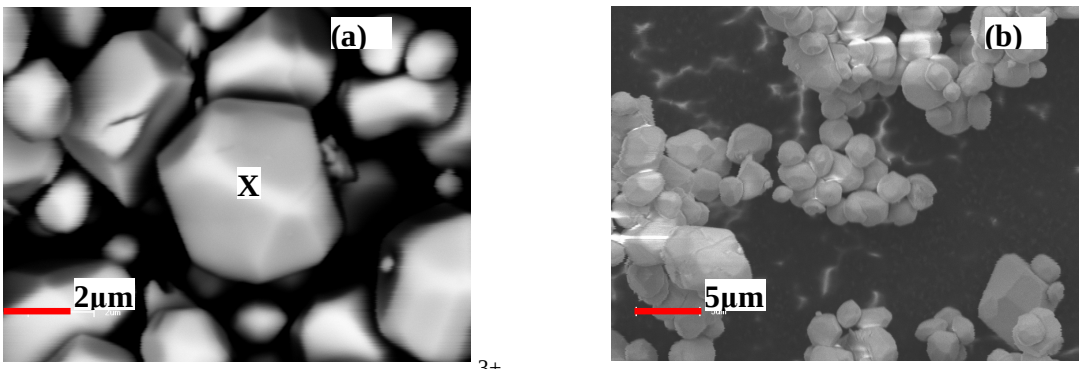

Figure 4.3: SEM images of the $Gd_2O_2S:Tb^{3+}$ phosphor powder at different magnifications (a) 10 000 and (b) 2000 magnifications

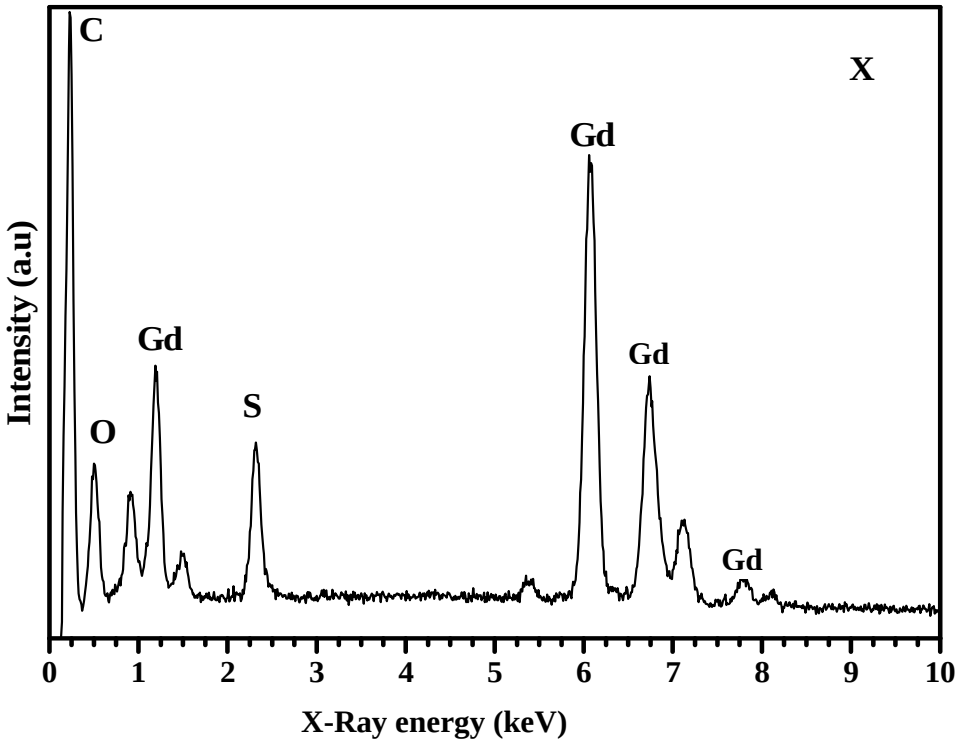

Figure 4.4: EDS Spectra of $Gd_2O_2S:Tb^{3+}$ powder phosphor on the marked area X

Figure 4.5 TEM micrographs of the $Gd_2O_2S:Tb3^+$ phosphor powders at different positions. It can be seen from figure. 4.5 that the phosphor particles are irregular and have agglomerations, and the observed particle sizes are about 20 and 100 nm.

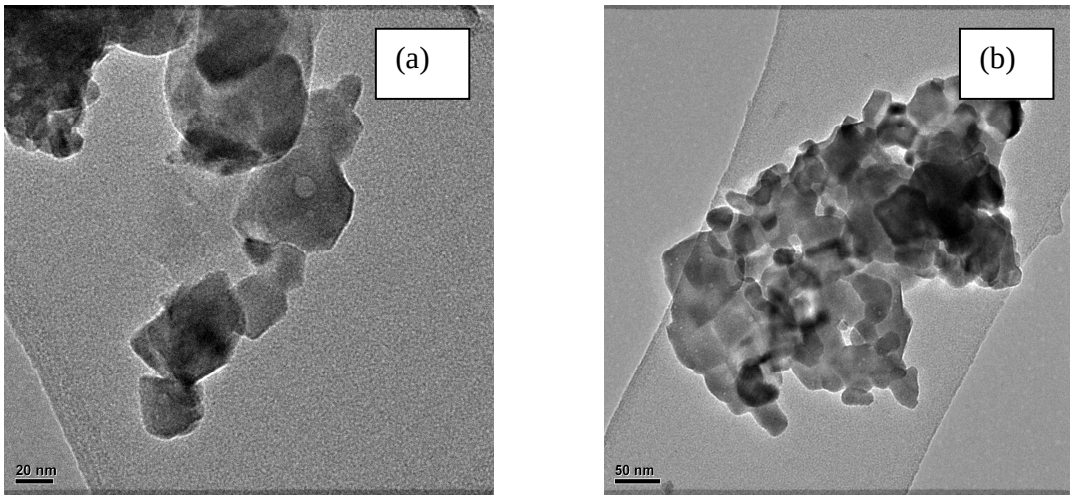

Figure 4.5: TEM images of the $Gd_2O_2S:Tb^{3+}$ phosphor powder at different positions

Figure 4.6 PL spectra of $Gd_2O_2S:Tb^{3+}$ powder phosphors with excitation energy of 254 nm. The luminescence peaks in the figure arise from the transitions of $^5D_4$ excited state levels to ^7F_J (J = 0, 1, 2, 3, 4, …) ground state levels, and belong to the characteristic emission of Tb^{3+}. The emission line at 490 nm corresponds to the $^5D_3 \rightarrow {}^7F_6$ transitions, and the emission lines between the 585 and 620 nm corresponds to the $^5D_4 \rightarrow {}^7F_4$ and $^5D_4 \rightarrow {}^7F_3$ transitions respectively. The peak at 545 nm arising from the $^5D_4 \rightarrow {}^7F_5$ transition is the strongest. When excited at 254 nm, bright green light can be observed. Under 254 nm UV excitation, the $Gd_2O_2S:Tb^{3+}$ phosphors exhibit the characteristic emission of Tb^{3+}. The energy transfer of the $^5D_3 \rightarrow {}^5D_4$ has not been observed in the PL spectra, and the reason may be that the bottom of the CTS (charge transfer states) in Gd_2O_2S is close to the $^5D_3$ level, and the energy transfer occurs between them, thus leading to the greatly reducing of the energy transfer of $^5D_3 \rightarrow {}^5D_4$.

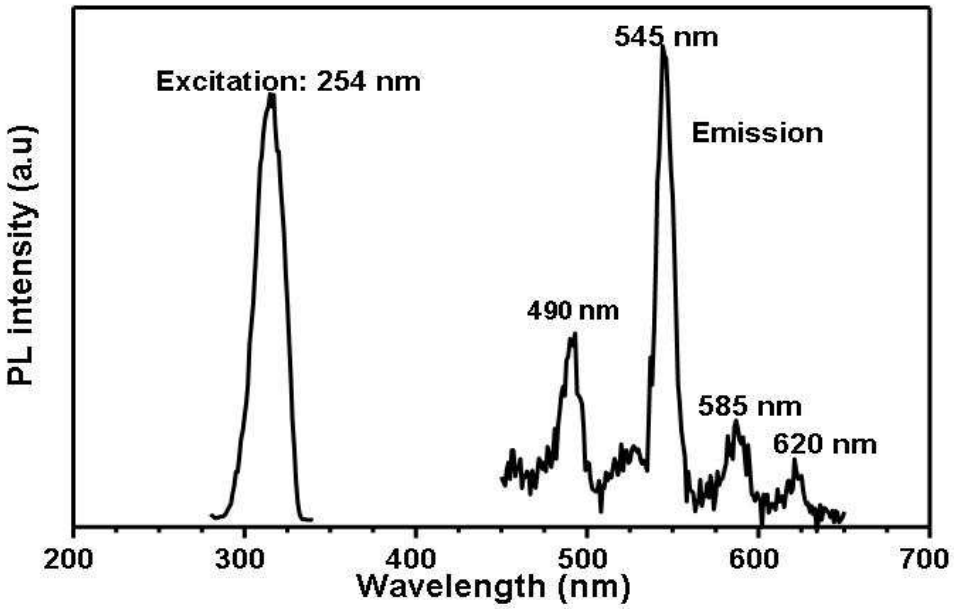

Figure 4.6: PL spectra for $Gd_2O_2S:Tb^{3+}$ phosphor powder, emission (λ_{exc} = 254 nm) and excitation (λ_{em} = 545 nm)

4.3.2 Degradation of $Gd_2O_2S:Tb^{3+}$ phosphor powder

In order to distinguish between the Gd, GdO and S peaks Gd metal was oxidized. The AES spectra before and after oxidation of the Gd are shown in figure 4.7. The main features of these spectra are the growth of the oxygen peak and the change in shape of the Gd low energy peaks in the 100 to 150 eV regions. The shoulder of the 142 eV Gd peak increased and the small peak at 128 eV became more pronounced and shifted to 127 eV during the oxidation process. Gd_2O_3 formed in the process.

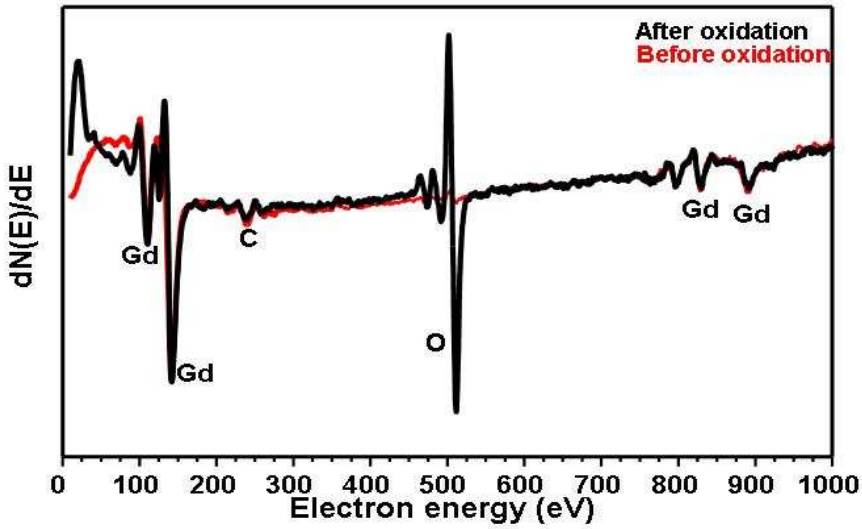

Figure 4.7: AES spectra of the Gd before and after oxidation at 1 x 10^{-7} Torr

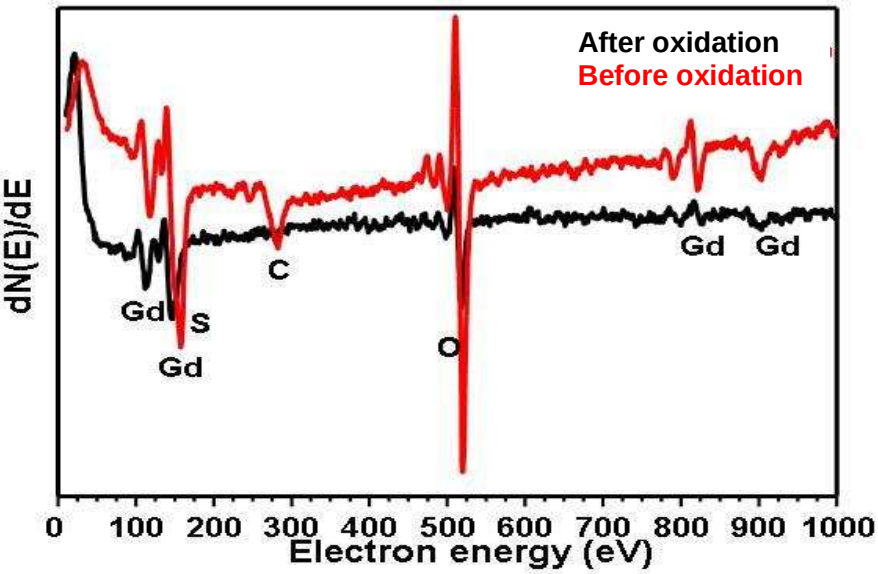

Figure 4.8: AES spectra of the $Gd_2O_2S:Tb^{3+}$ before and after degradation at 1 x 10^{-6} Torr

The AES spectra as measured before electron degradation and after electron degradation at 1 x 10^{-6} Torr oxygen are shown in figure 4.8. The O peak increased and the C decreased during electron bombardment. Residual gas analyses showed an increase in the CO and CO_2 concentration during electron bombardment indicating that the C was removed as volatile species according to the ESSCR (electron stimulated surface chemical reaction) model. The low energy peaks at around 150 eV also showed significant changes during electron bombardment. The peak is a combination of Gd and S. The change in the peak shape is due to the removal of S from the surface. The APPH's (Auger peak to peak heights) could not be determined directly from the AES spectra. The elemental standards, as shown in figure 4.9, were therefore used in combination with LLS to subtract the relative S and Gd contribution towards the peak. Both the low energy Gd peaks measured on the elemental standard before and after oxidation are shown together with the S peak as measured from a ZnS standard.

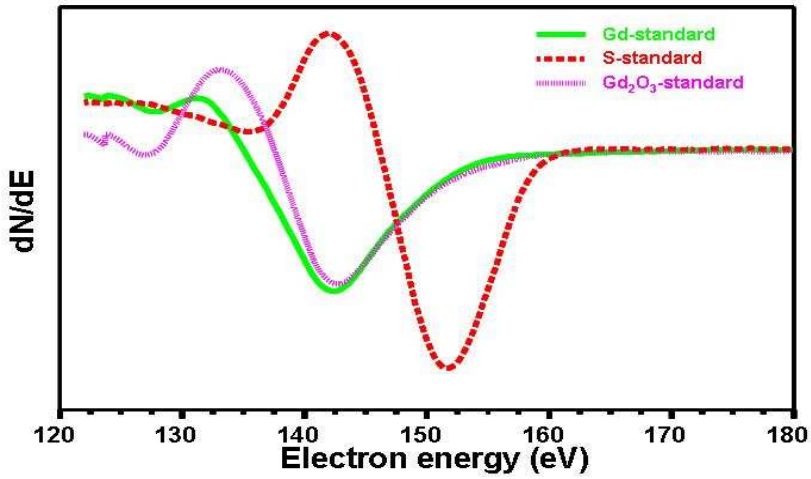

Figure 4.9: Low energy AES spectra of the S and the Gd standards. (Gd both the pure and the oxidized Gd)

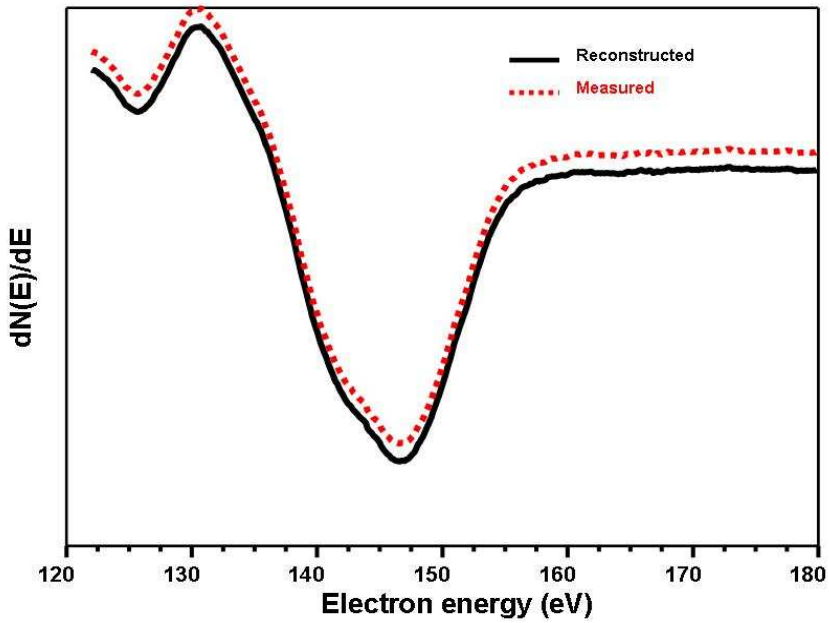

Figure 4.10: A reconstructed and measured AES spectra of the Gd_2O_2S:Tb during degradation

Let a_1, a_2 and a_3 be three $N \times 1$ vectors containing the standard spectra of the $S(\times 2)$ in ZnS, the pure Gd and the Gd in the oxidized state respectively. The $N \times 3$ matrix, A = [a_1, a_2, a_3] is constructed. Let each measured spectrum B, be an Nx1 vector containing the Auger spectrum of the combination of the three standards. The 3x1 vector X = [x_1, x_2, x_3], with x_1, x_2 and x_3 being the fractions of a_1, a_2 and a_3 in B, is the least squares solution to the over-determined system

$$AX = B \qquad (1)$$

given by [10-11].

$$X = (A^T A)^{-1} A^T B \qquad (2)$$

An example of a reconstruction of one of these spectra, by using these standards and the relative ratios as determined with LLS, are shown in figure 4.10. It is clear that the combination as determined from the LLS calculations is a perfect fit to the spectrum. The relative APPH of O, C and the calculated S, Gd in pure Gd and in the oxidized state are given in figure 4.11 as function of electron bombardment time at 1 x 10^{-6} Torr oxygen. It is clear that C was removed from the surface and the O increased during electron bombardment. The Gd also changed from a Gd_2O_2S state to a Gd_2O_3 state. It is clear that surface reactions did occur during electron bombardment in an oxygen atmosphere. As in the case of several other phosphors [12] the change in surface concentration may be explained by the ESSCR mechanism in which the Gd_2O_2S was converted to Gd_2O_3. Simultaneous with the change in surface concentration the CL decrease as shown in figure 4.12. The decrease of the CL intensity as function of electron dose is shown in figure 4.12.

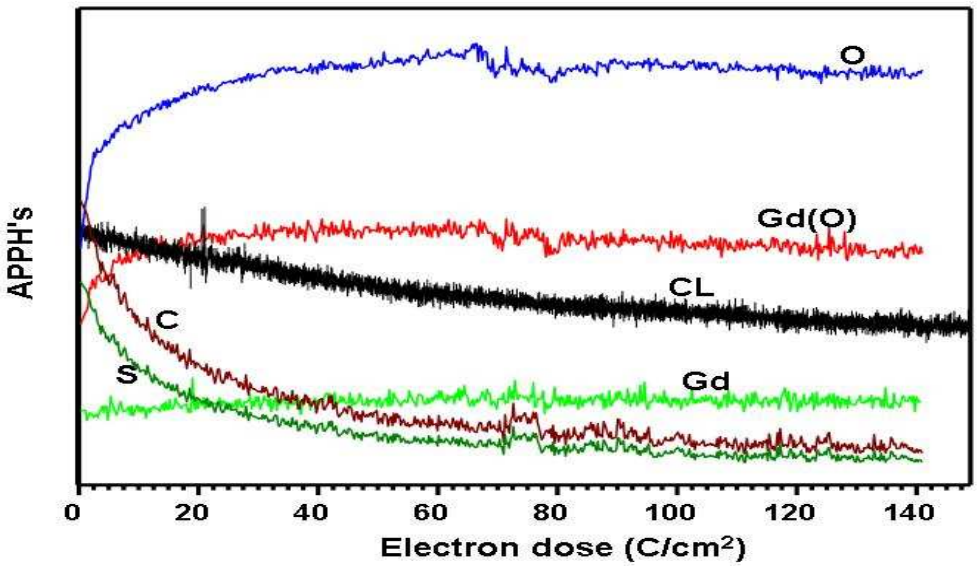

Figure 4.11: APPH's and CL as function of electron bombardment time at 1 x 10^{-6} Torr oxygen

The CL spectra before degradation and after degradation as function of wavelength are shown in figure 4.12. The CL decreased due to the formation of a new non-luminescent surface oxide layer. The CL peak positions are in agreement with the normalized PL spectra of Popovici et. al. [5] of synthesized $Gd_2O_2S:Tb^{3+}$. The main emission peak due to the $^5D_4 \rightarrow {}^7F_5$ transition is at a wavelength of 550 nm. Less intense emission peaks at 490 nm, 585 nm and 620 nm due to the $^5D_4 \rightarrow {}^7F_J$ (J = 0, 1, 2, 3,…) transitions are also shown. The main emission peak at 545 nm was only about 45% of the initial intensity after degradation.

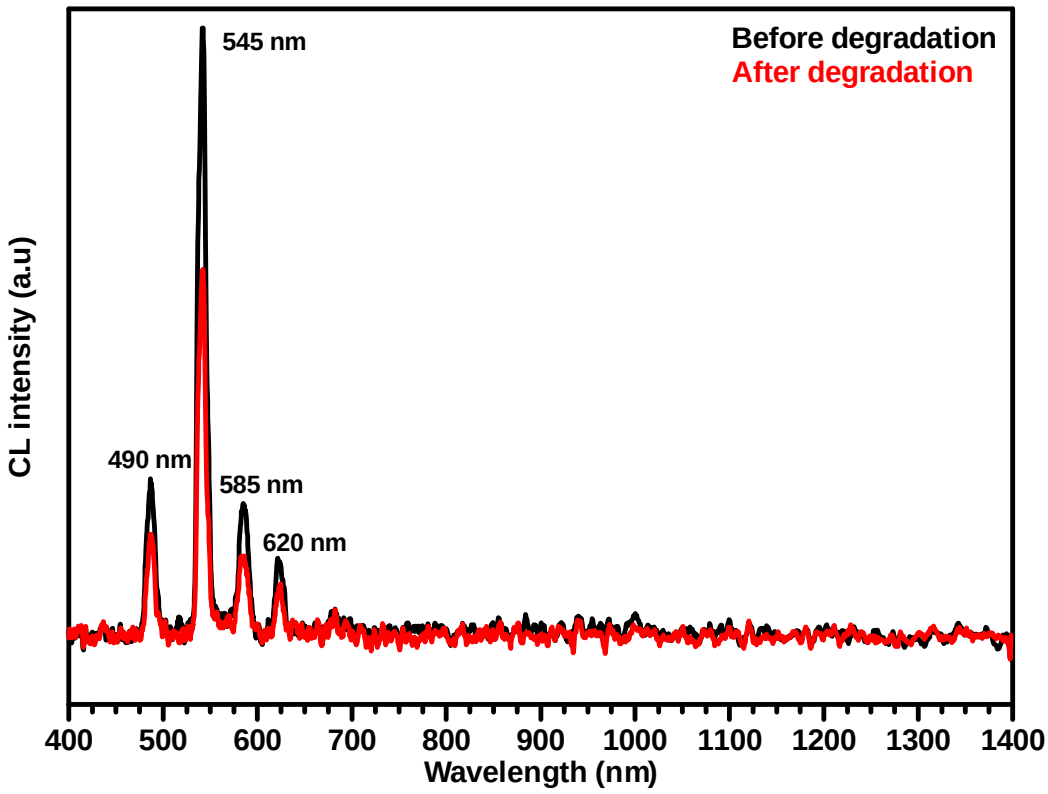

Figure 4.12: CL spectra before and after degradation of $Gd_2O_2S:Tb^{3+}$ at 1 x 10^{-6} Torr

Figure 4.13 shows fitted XPS spectra for sulphur 2p (a) before and (b) after degradation for 1x10^{-6} Torr obtained at 165.8 eV. A small peak increased at the lower binding energy side of the main S peak during electron bombardment, which is currently ascribed to Gd_2S_3 (158.2 eV) [13]. The peak at the higher binding energy (170 eV) corresponds to sulphur dioxide bondings (SO_2). A noticeable growth in these SO_2 peaks after degradation occurred, which suggest that surface reactions occurred.

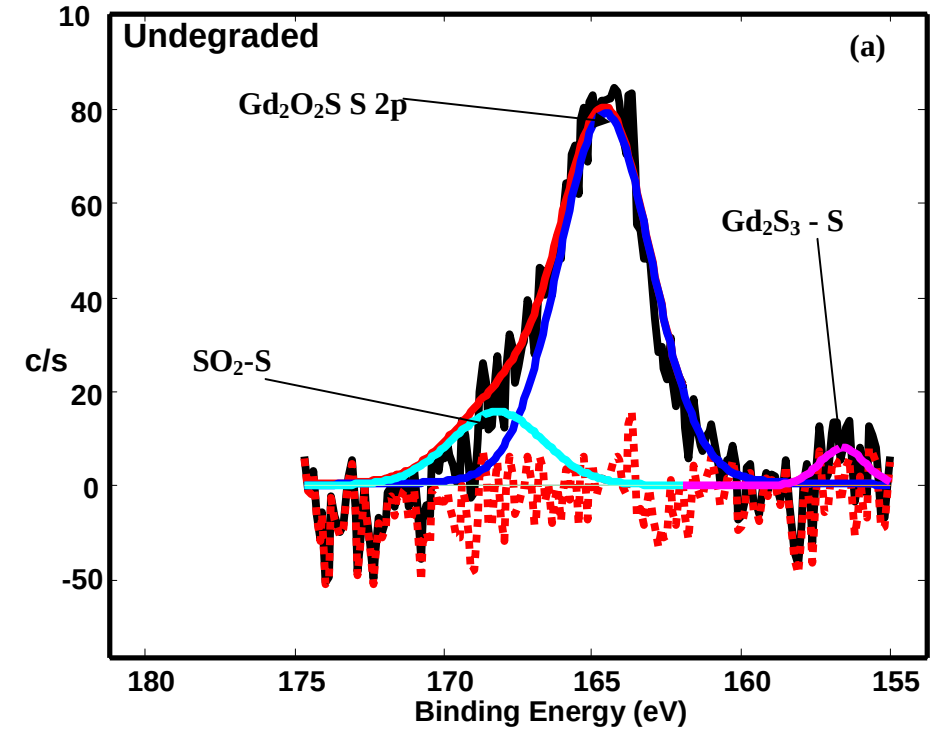

Figure 4.13: Fitted XPS for S 2p of $Gd_2O_2S:Tb^{3+}$ phosphor powder peaks (a) before and (b) after degradation for $1x10^{-6}$ Torr

Figure 4.14 shows fitted XPS for O1s peaks (a) before and (b) after degradation for $1x10^{-6}$ Torr obtained at O 1s at 531.6 eV. It can be noted that for the both degraded and undegraded powder spots only two binding energy peaks were identified. The degraded powder has an increase in Gd_2O_3 peak than the undegraded one. The increase in Gd_2O_3 is due to the oxide formation on the surface as a result of the ESSCR process as observed in the APPH results. It is therefore clear that a chemical reaction occurred during the degradation process. The binding energy assignment of the mixed oxides is based on a large extent to the core level screening that occurs in O^{2-} anion compared to the other oxygen species that are present on the surface and the relative magnitude of this peak compared to other O 1s peaks present [14]. The peak at the lower binding energy (528.4 eV) corresponds to sulphur dioxide bondings (SO_2). A noticeable growth in these SO_2 peaks after degradation occurred, which suggest that surface reactions occurred.

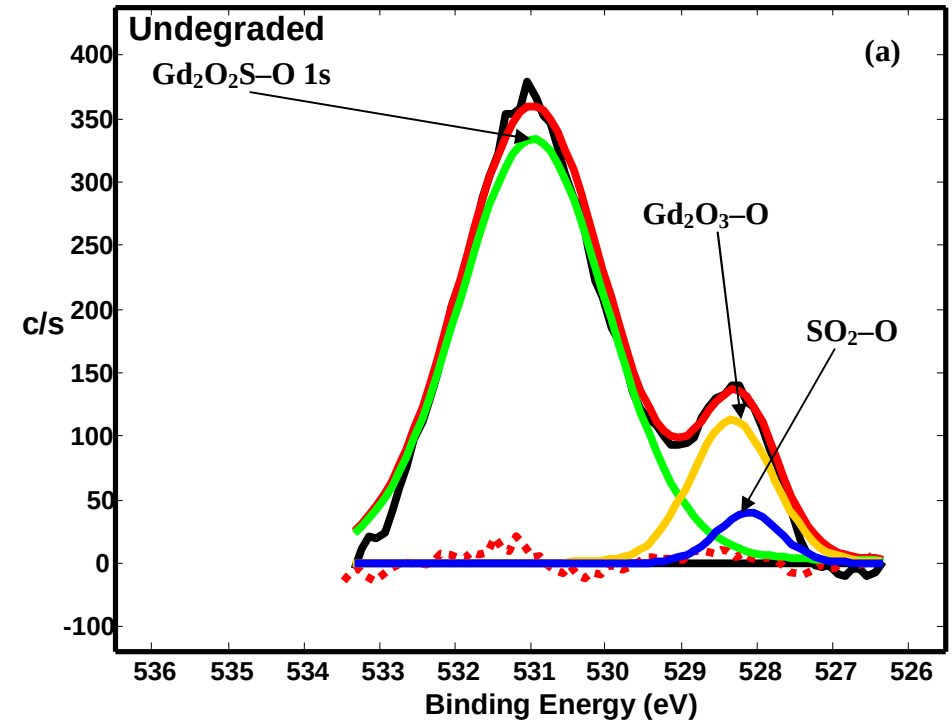

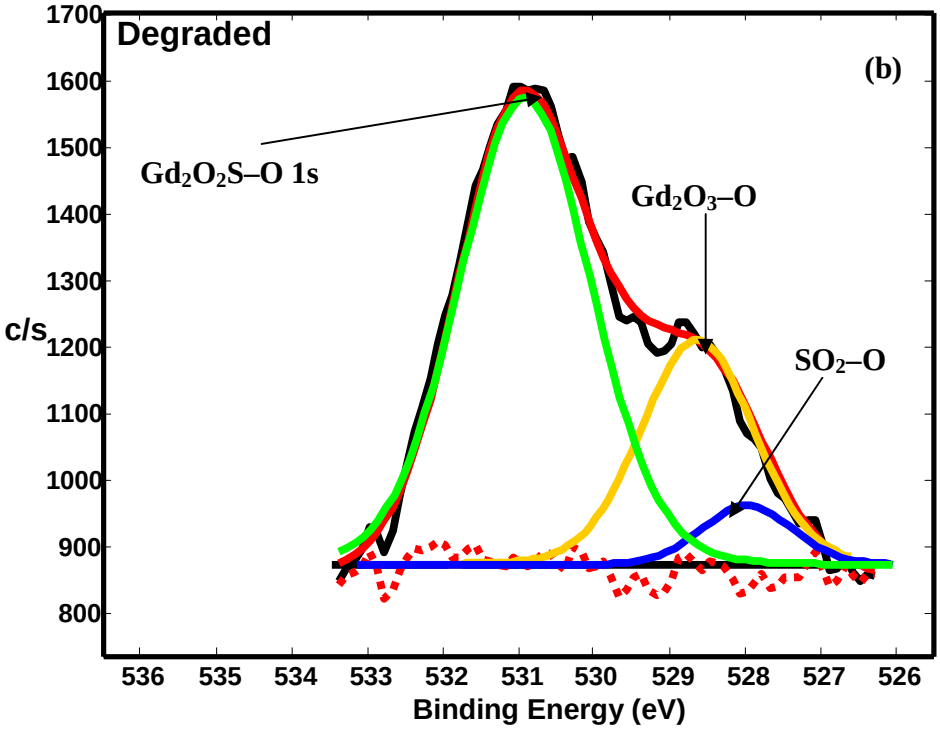

Figure 4.14: Fitted XPS for O 1s of $Gd_2O_2S:Tb^{3+}$ phosphor powder peaks (a) before and (b) after degradation for $1x10^{-6}$ Torr

Figures 4.15 show the fitted results from an XPS spectrum of the Gd 3d peaks (a) before and (b) after degradation. The peak shape changed due to an extra peaks of Gd_2O_3 (1189.0 eV) and Gd_2S_3 (1192.2 eV) that developed at higher binding energies. Gd_2O_2S-Gd 3d peaks were measured at 1185.20 eV. Both the degraded powder and undegraded spots recorded one peak of Gd_2O_2S-Gd 3d. Spectra extending beyond the binding energy of the Gd 3d peak could be obtained which is a satellite peak. The peaks for Gd_2O_3 and Gd_2S_3 after degradation have increased in terms of relative ratios as compared to the undegraded sample; this clearly shows that the surface reaction did occur after degradation. Figure 4.16 shows the Gd 4d peaks position for the Gd_2O_2S (Gd_2O_2S-4d peaks) (a) before and (b) after degradations. Six peaks can be identified for the Gd 4d core level spectrum after deconvolution of the experimentally measured curve. Gd $4d_{3/2}$ and Gd $4d_{5/2}$ peaks of the Gd_2O_2S are located at 146.7 eV and 141.6 eV respectively which is in agreement with Datta et. al.[15]. Apart from above, there are two peaks measured at 142.2 eV and 147.3 eV associated with Gd_2O_3 and the small peaks measured at 147.9 eV and 144.8 eV associated with Gd_2S_3. There is also an increase in relative ratio of the peaks, this suggests that a surface chemical reaction occurred and another possibility for the presence of the peaks (Gd_2O_3 and Gd_2S_3) could be chemical decomposition of the material [15].

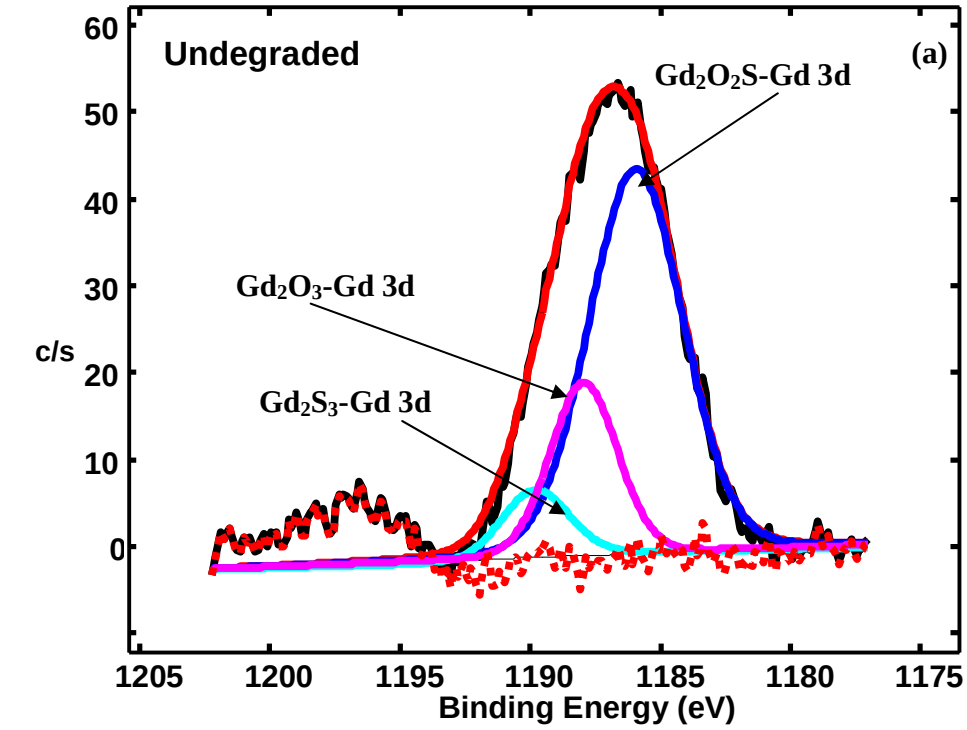

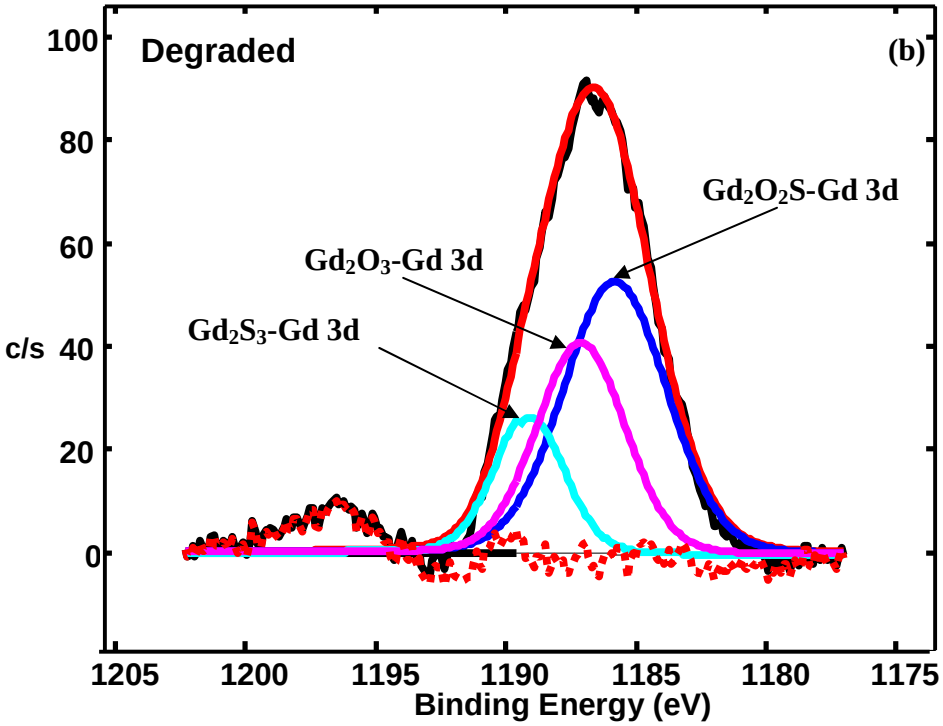

Figure 4.15: Fitted XPS for Gd 3d of $Gd_2O_2S:Tb^{3+}$ phosphor powder peaks (a) after and (b) before degradation for $1x10^{-6}$ Torr

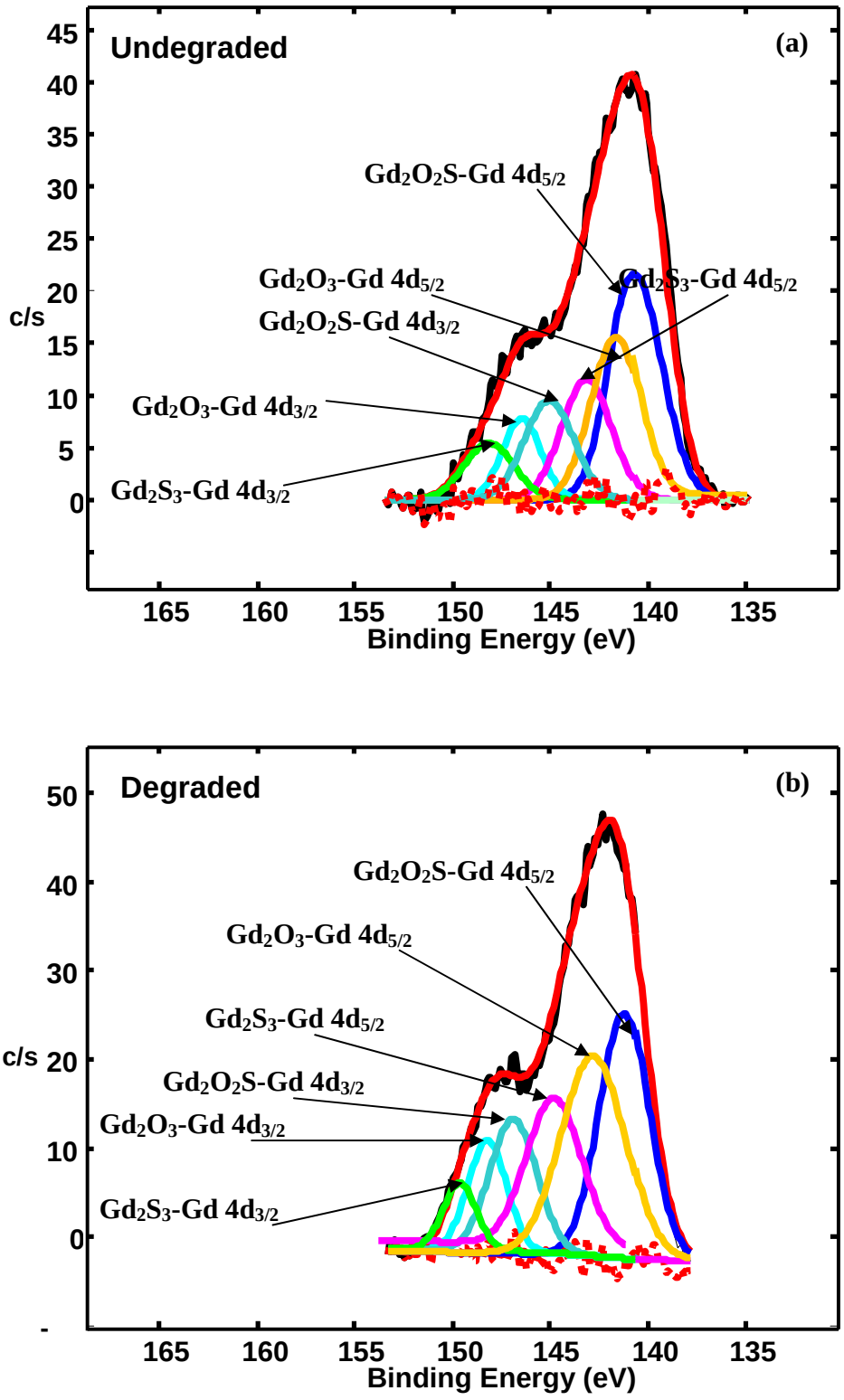

Figure 4.16: Fitted XPS for Gd 4d of $Gd_2O_2S:Tb^{3+}$ phosphor powder peaks (a) after and (b) before degradation for $1x10^{-6}$ Torr

4.4 Conclusion

Under 254 nm UV excitation, the $Gd_2O_2S:Tb^{3+}$ phosphors exhibit the characteristic emission of Tb^{3+}. The sample present bright green light that can be observed with the naked eye. The energy transfer of the $^5D_3 \rightarrow {}^5D_4$ has not been observed in the PL spectra, and the reason may be that the bottom of the CTS (charge transfer states or excited states) in Gd_2O_2S are close to the $^5D_3$ level, and the energy transfer occurs easily between them, thus leading to the reducing of the energy transfer of $^5D_3 \rightarrow {}^5D_4$. It was shown that the intensity of the CL emission from the $Gd_2O_2S:Tb^{3+}$ phosphor decreased simultaneously with the desorption of sulphur from the surface. The ESSCR mechanisms was used to explain the effects of sulphur desorption and the formation of a non-luminescent oxide layer. A dead layer of Gd_2O_3 and Gd_2S_3 are responsible for the degradation of the CL intensity with an increase in electron dose. The linear least square method was successfully used to separate the Gd and S peaks in the AES spectra. The XPS results confirmed the presence of Gd_2O_3 and Gd_2S_3 on the degraded powder spots.

References

1. M.R. Royce, US Patent 3 418 (1968) 246

2. M.R. Royce, A.L. Smith, Electrochem. Soc., Spring Meeting Extended Abstracts 34 (1968) 94

3. G.E. Giakoumakis, A.J. Pallis, Solid State Comm. 70 (1989) 419

4. G. Blasse, B.C. Grabmaier, Luminescence Material, Springer-Verlag, New York, 1994

5. E.J.P. Popovici, L. Muresan, A. Hristea-Simoc, E. Indrea, M. Vasilescu, M. Nazarov, D.Y. Jeon, Opt. Mat., 29 (2002) 632

6. Y. Jiang, Y. Wu, J. Am. Ceram. Soc., 83 (10) (2000) 2628

7. H. Yamamoto, T. Kano, J. Electrochem. Soc., 126 (2) (1979) 305

8. 13. W. Rossner, M. Ostertag, F. Jermann, A.G. Siemens, Electrochem. Soc. 98 (1999) 187

9. E.J.P. Popovici, L. Muresan, A. Hristea-Simoc, E. Indrea, M. Vasilescu, M. Nazarov, D.Y. Jeon, Opt. Mat., 27 (2004) 559

10. H.C. Swart, A.J Jonker, C.H. Claassens, R. Chen, L.A. Venter, P. Ramoshebe, E. Wurth, J.J. Terblans, W.D. Roos, App. Surf. Sci., 205, (2003) 231

11. W.D. Roos, G.N. van Wyk and J. du Plessis, Surf. Interface Anal., 22 (1994) 65

12. H.C. Swart, J.J. Terblans, E. Coetsee, O.M. Ntwaeaborwa, M.S. Dhlamini and P.H. Holloway, J. Vac. Sci. Tech., *A* 25 (4) (2007) 91

13. J. J. Dolo, H. C. Swart, E. Coetsee, J. J. Terblans, O. M. Ntwaeaborwa, B. F. Dejene, Hyperfine Interact (2010)197:129-134

14. A.K. Hashimoto, X-ray photoelectron spectra of several oxides, Corros. Sci., 17 (1977) 559

15. P. Datta, P. Majewski, F. Aldinger, Mat. Charac., 60 (2009) 138

CHAPTER 5

Characterization and Cathodoluminescence degradation of $Gd_2O_2S:Tb^{3+}$ thin film phosphor

5.1 Introduction

Current fundamental research on $Gd_2O_2S:Tb^{3+}$ is aimed at improving its optical properties. Although studies of optical properties of $Gd_2O_2S:Tb^{3+}$ phosphors have been reported, the focus has mainly been on the powder form of the phosphor [1-5].

In this chapter, $Gd_2O_2S:Tb^{3+}$ thin films were deposited by pulsed laser deposition at different oxygen pressures and substrate temperatures between 400 to 600 ^oC. Their structure and photoluminescence properties were investigated. The optical properties of the films were evaluated for possible applications in display technologies. The stability of the phosphor films under electron beam bombardment was also investigated.

5.2 Experimental

A commercial $Gd_2O_2S:Tb^{3+}$ powder phosphor from Phosphor Technology was pressed without binders to make a pellet that was used as a target for laser ablation. The chamber was first evacuated to a base pressure of 3 $x10^{-5}$ Torr before backfilling to an oxygen pressure of 700 to 900 mTorr during the growth of the films. Both films were post annealed at 600 and 900 ^oC as discussed in section

5.3.3 of this chapter. The crystalline structure of the films was analyzed using X-ray diffraction, and surface topography and particle morphology were analyzed with a scanning electron microscope and an atomic force microscope. The Cary Eclipse fluorescence spectrophotometer was used to collect the photoluminescence emission data at room temperature. The experimental part of the CL degradation of the thin film was similar to that used for the commercial powder as described in chapter 4 of this thesis.

5.3 Results and discussions

5.3.1 Characterization of room temperature ablated $Gd_2O_2S:Tb^{3+}$ thin films phosphors

Figure 5.1 shows the XRD spectrums of the thin films deposited in vacuum, 200 and 300 mTorr at room temperature. There is an emanation of the (100) peak on all of the films, which is not well pronounced in the film for vacuum conditions. This preferential growth is due to the influence of the Si (100) substrate that is favoured by the high mobility of the ablated species [6]. The substrate influence on the crystalline phase of $Gd_2O_2S:Tb^{3+}$ phosphor was also observed by Tian et. al. [7]. The increased intensity of the (100) peak in 300 mTorr in the presence of O_2 gas proves the influence of the background pressure on the modification of the ablated plume for improved surface orientation. The preferential orientation that is influenced by the Si (100) substrate is more dominant in this film.

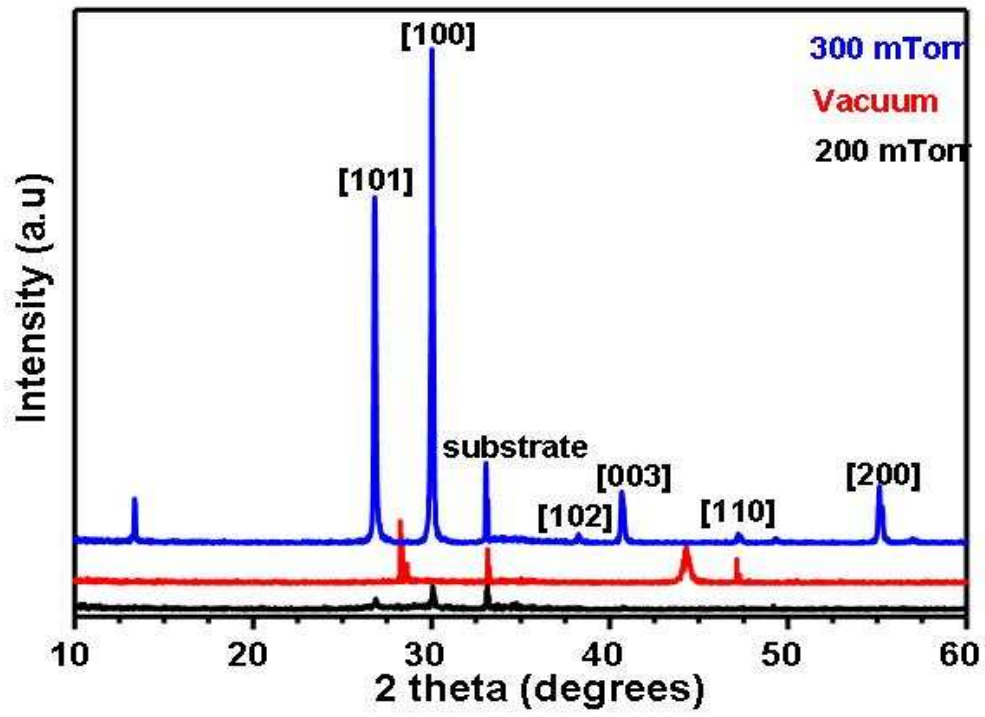

Figure 5.1: XRD patterns of the films deposited in vacuum, 200 and 300 mTorr O_2 at room temperature

Figures 5.2 shows the PL emission spectra of the films deposited in vacuum, 200 and 300 mTorr O_2 at room temperature. $Gd_2O_2S:Tb^{3+}$ emission spectrum between 400 - 650 nm exhibits, several bands characteristic of $^5D_4 \rightarrow {}^7F_J$ (J = 0, 1, 2, 3, 4) transitions of Tb^{3+} ions with an excitation wavelength of 255 nm. $^5D_4 \rightarrow {}^7F_5$ transition is the most intense and confers to the materials a global greenish emission. The intensity of the film in vacuum is very low. For vacuum deposition, nucleation in the plume is minimal [8]. Plume species reach the substrate predominantly as atoms and small clusters. The low surface mobility of the cooled substrate minimizes crystal grain growth and film forms. As ambient pressure increases, some fraction of the species forms crystalline structures in transit. The size and number density of such structures upon reaching the substrate determine

the degree of crystallinity of the deposited film. These structures act as seeds for growth, yielding a polycrystalline film [8].

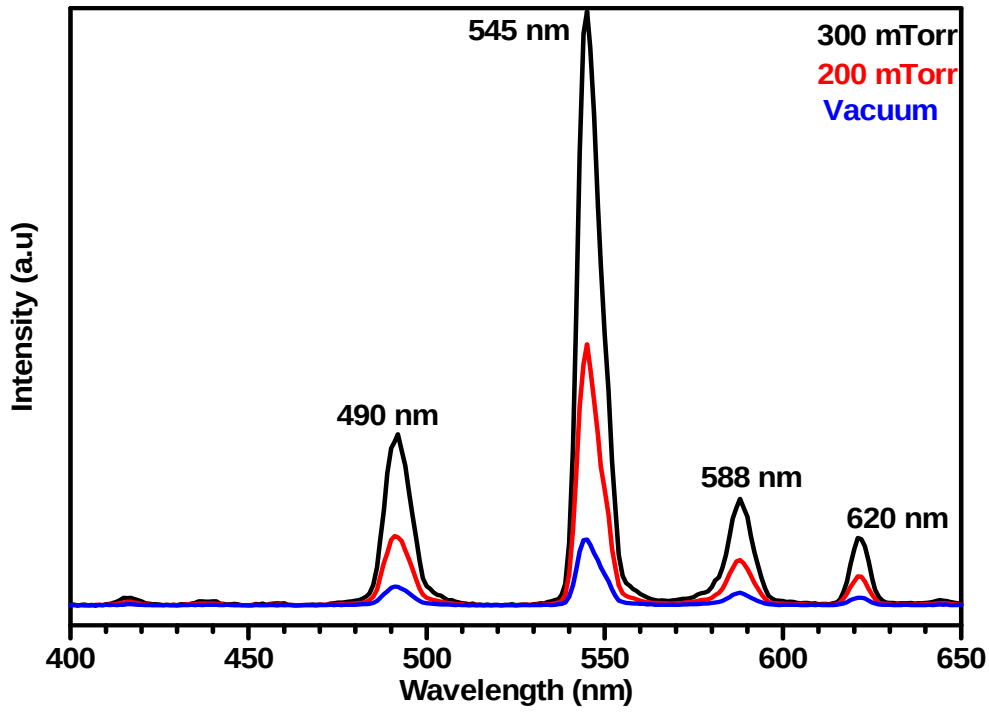

Figure 5.2: PL emission spectra of the films deposited in Vacuum, 200 and 300 mTorr O_2 at room temperature

Figure 5.3 (a) - (c) show the AFM images of the samples deposited using PLD at room temperature in (a) vacuum; (b) 200 mTorr; and (c) 300 mTorr. From figure 5.3 (a), the particles on the surface are not clearly distinguishable, which is in agreement with observations made by Swart et. al [9]. Smooth phosphor layers are normally obtained with PLD in vacuum [9].

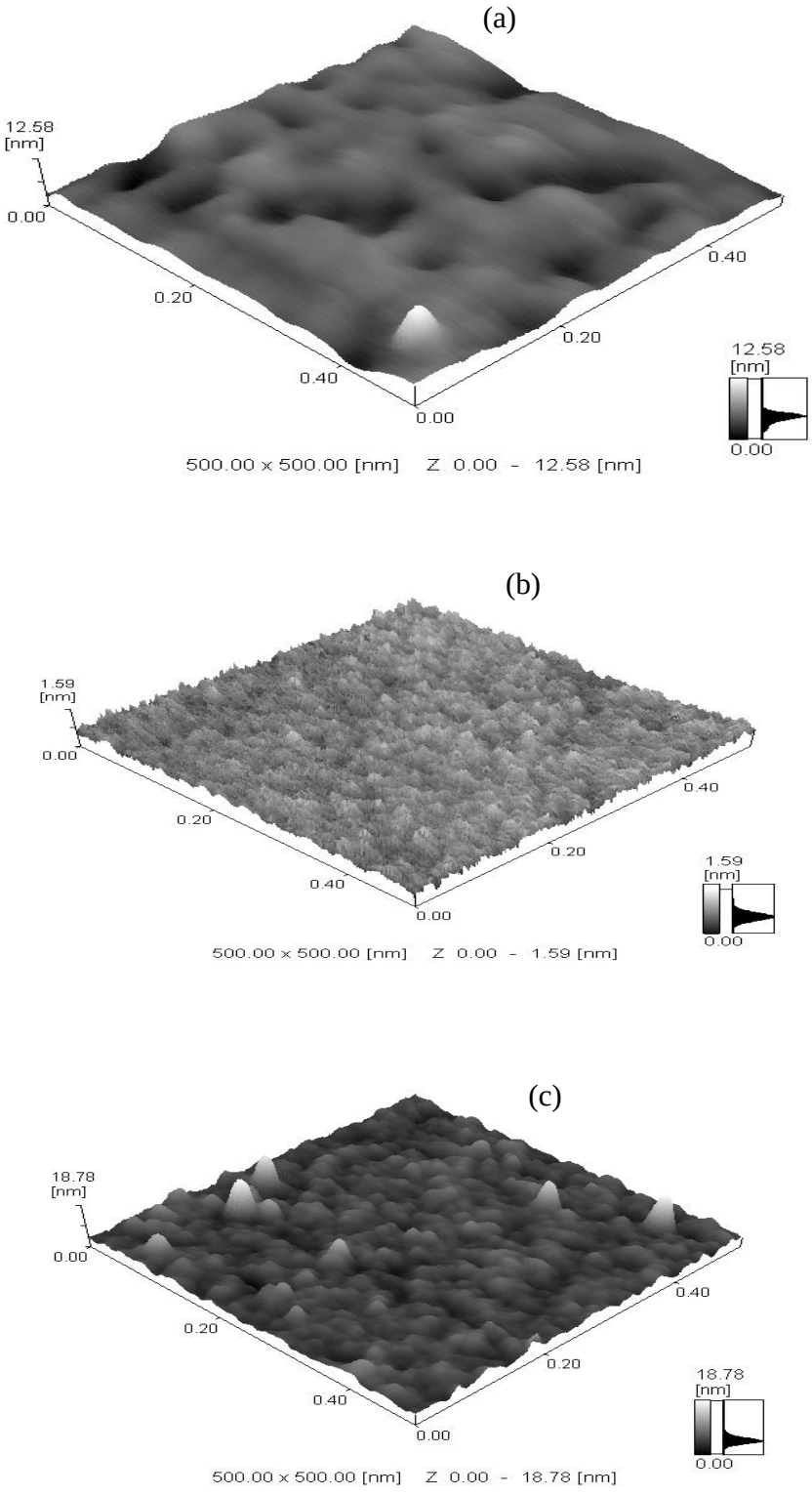

Figure 5.3: AFM images of (a) vacuum; (b) 200 mTorr; and (c) 300 mTorr

5.3.2 The effect of the Oxygen pressure on the structure, morphology and PL intensity of the PLD deposited $Gd_2O_2S:Tb^{3+}$ thin film phosphor

Figures 5.4 shows the XRD patterns of $Gd_2O_2S:Tb^{3+}$ thin films grown at 600 ^oC (a) 100 mTorr and (b) 300 mTorr O_2. While Figure 5.5 shows the same for films grown at a substrate temperature of 400 ^oC. It is clear that the films crystallized in the well known hexagonal structure of Gd_2O_2S. The degree of crystallinity increased with an increase in oxygen pressure. The intensity of the XRD peak from the (1 0 0) and (1 0 1) crystal planes were found to increase with the oxygen pressure in the range from 100 to 300 mTorr O_2. This may be attributed to the enhanced oxidation kinetics and improvement in crystalline nature of the films. No Tb_2O_3 diffraction peaks were detected, which means that the Tb^{3+} ion incorporated into the Gd_2O_2S host lattice is still homogeneously [10] distributed in the host matrix. As the oxygen pressure increases, the crystallinity of the films improved. It is also clear that the 400 ^oC thin film consist of nanoparticles as seen from the broad XRD peaks.

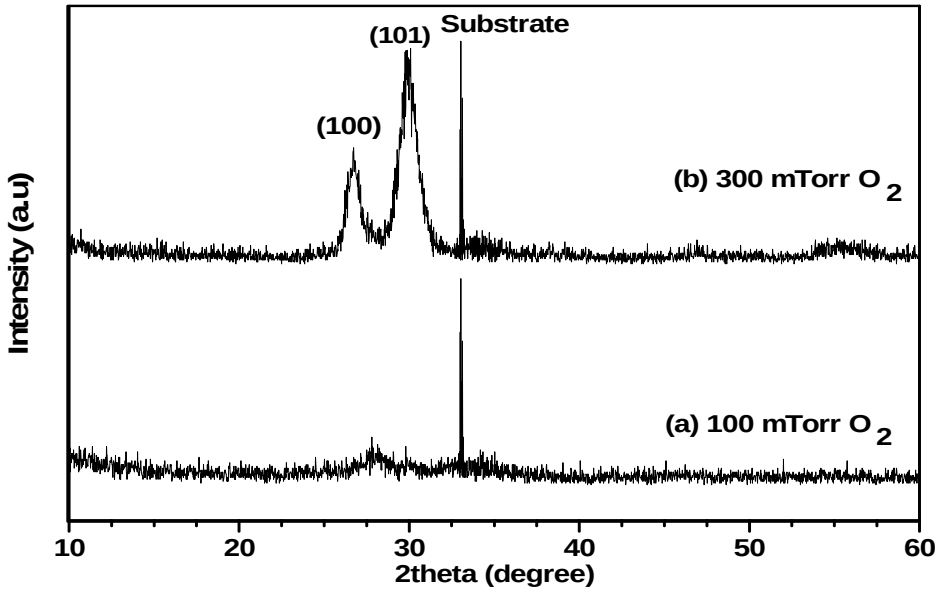

Figure 5.4: XRD patterns of the films deposited in (a) 100 mTorr and (b) 300 mTorr O_2 at a substrate temperature of 600 ^oC with aspect ratio 1.6303:1

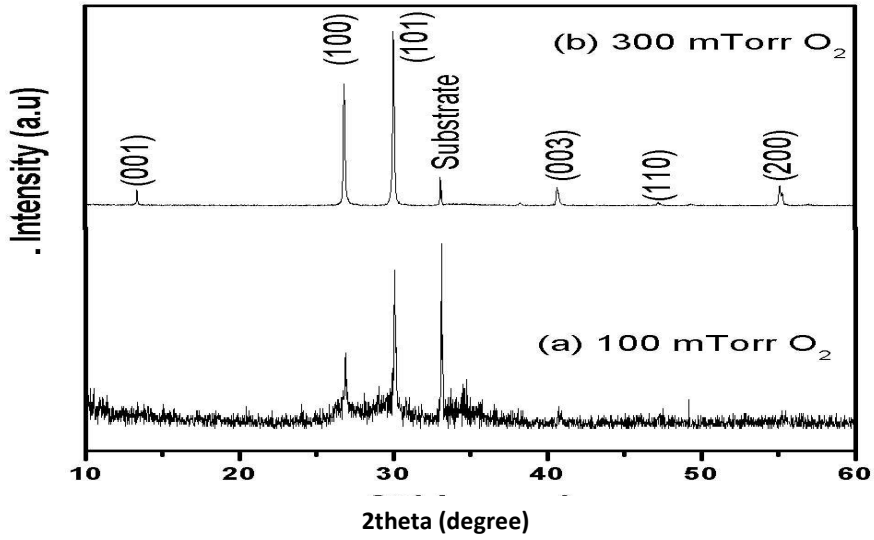

Figure 5.5: XRD patterns of the films deposited in (a) 100 mTorr and (b) 300 mTorr O_2 at a substrate temperature of 600 ^oC with aspect ratio 1.71564:1

Figure 5.6 (a) and (b) show the SEM images for the films deposited at 100 and 300 mTorr O_2 respectively. The substrate temperature was maintained at 400 ^oC. Figures 5.7 (c) and (d) show the SEM images of the films deposited at 100 and 300 mTorr O_2, respectively, when the substrate temperature was maintained at 600 ^oC. It can be seen that the films grown at higher oxygen pressure have relatively rougher surfaces (50-90 nm) than the films grown at lower oxygen pressures. The films grown at higher oxygen pressures and higher substrate temperature were found to exhibit high intense photoemission and the particles distributed uniformly all over the surfaces. While the film deposited at lower oxygen pressures exhibit low intense photoemission and the surface were found to be very smooth with a few particles on the surface.

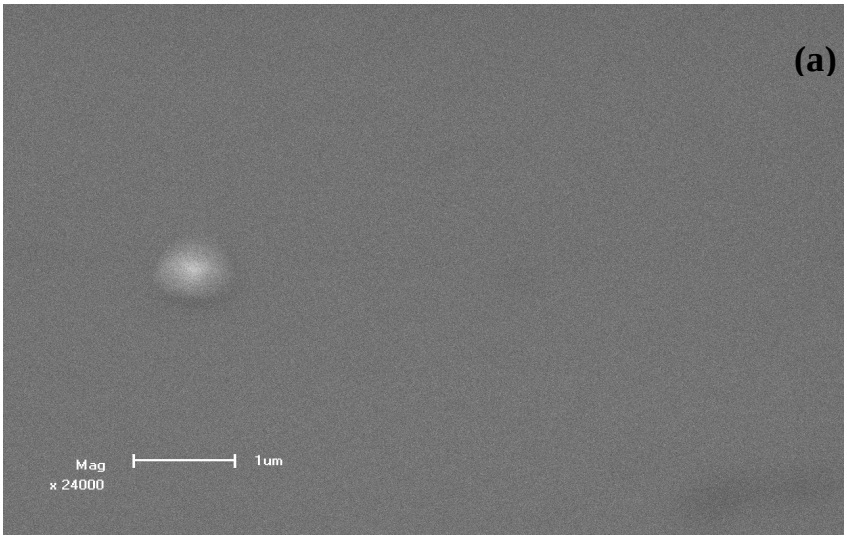

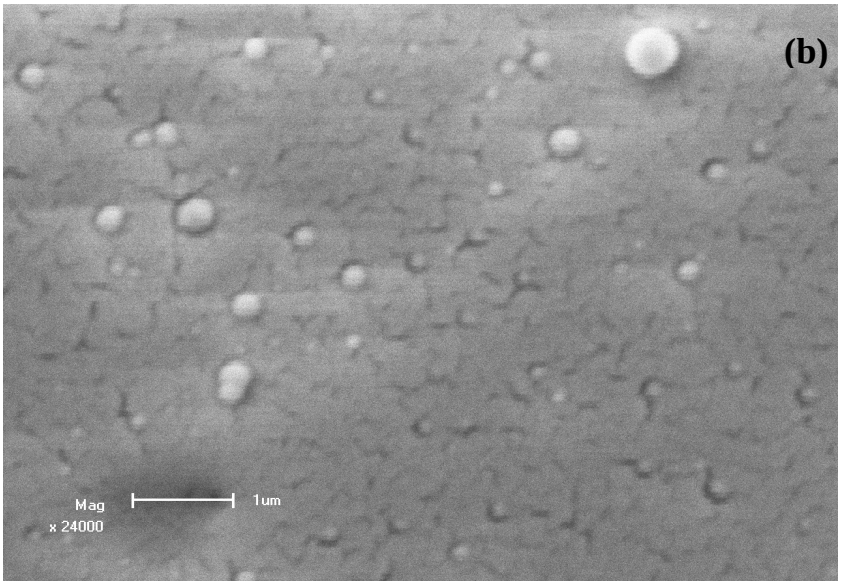

Figure 5.6: SEM images of the films deposited in (a) 100 mTorr O_2 and (b) 300 mTorr O_2 at a substrate temperature of 400 ^{o}C

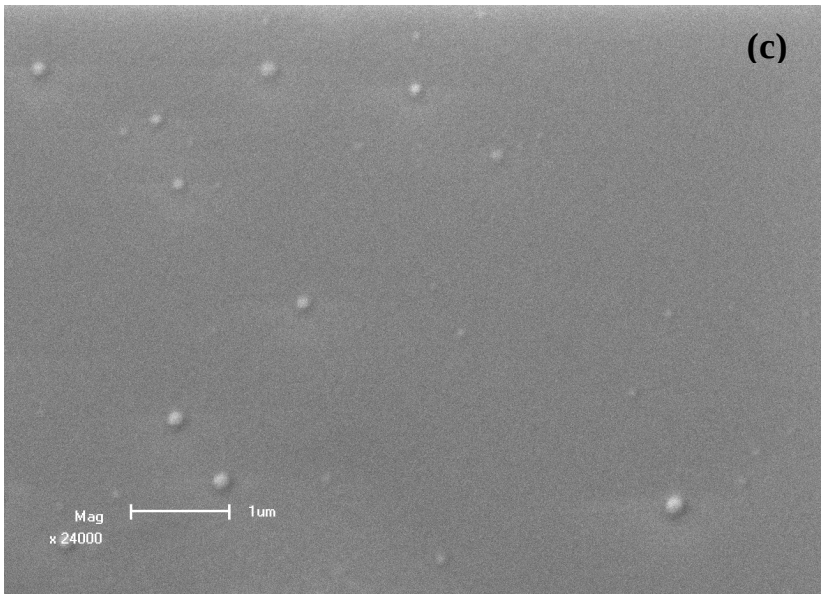

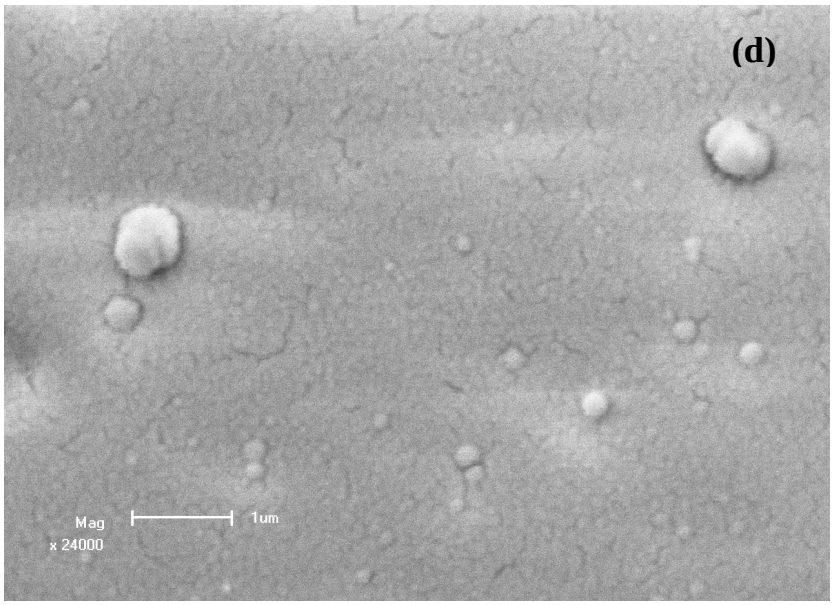

Figure 5.7: SEM images of the films deposited in (c) 100 mTorr O_2 and (d) 300 mTorr O_2 at a substrate temperature of 600 ^oC

Figure 5.8 AFM images of the samples deposited at 100 mTorr (a) 400 ^{o}C (b) and 600 ^{o}C. Figure 5.9 shows AFM images deposited at 300 mTorr (c) 400 ^{o}C and (d) 600 ^{o}C. It is clear that spherical nanoparticles were deposited during the deposition process. The particle sizes of the different samples varied from 19 to 36 nm depending on the deposition conditions. An average particle size of 36 nm was calculated for the film grown at 100 mTorr, 400 ^{o}C, figure 5.8 (a), and the particle size of 19 nm was calculated for the film grown at 300 mTorr, 600 ^{o}C. The particles were also less agglomerated at the higher oxygen pressures (figure 5.9 (c) versus figure 5.8 (b)). The mean free path of the particles in a low ambient pressure is longer compared to the mean free path at higher ambient pressures. More collisions between the ultrafine particles (vaporised particles close to the target) at a higher ambient pressure lead to nucleation and growth of smaller nanoparticles when arriving at the substrate. In vacuum there are virtually no collisions between the particles before reaching the substrate. Longer residence time of the particles in the plume, as is the case at higher ambient pressures, lead to more evenly distributed particles (figure 5.9 (c) and (d)). Light emission from the spherical shaped phosphor particles as excited by the electron beam is more intense due to the fact that much less photons encounter total internal reflection [11]. The increase in the substrate/deposition temperatures is reported to have caused an increase in the connectivity (agglomeration) between particles [12] due to sintering of small particles. This would eventually lead to grain growth at high enough temperatures. Dhlamini et al. [13] deposited SiO_2:PbS thin films at different temperatures (100 to 400 ^{o}C) on Si (100) substrates. The deposited material consisted of an agglomeration of spherical nanoparticles distributed all over the substrates. The diameters of the spheres increased with temperature, suggesting a correlation between deposition temperatures and particle size. Similar results have been reported by Riabinina et. al. [14]. In this case, however it was found that less agglomeration occurred at the higher temperature.

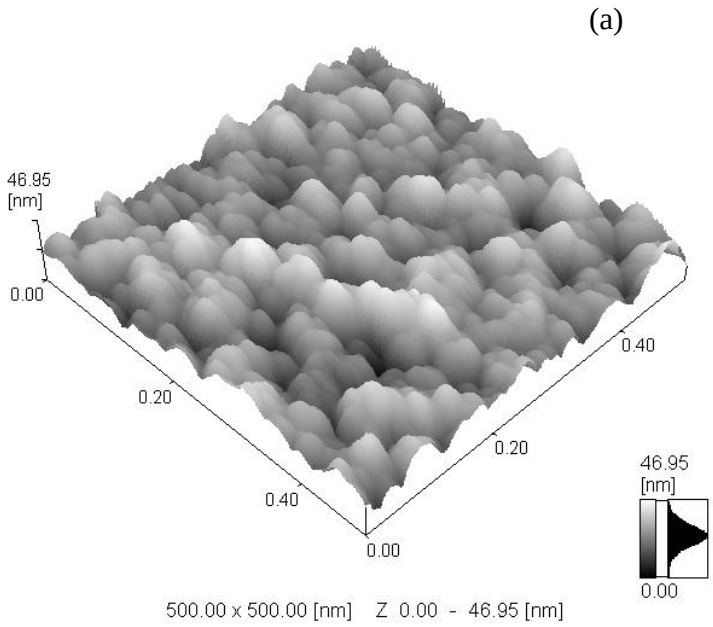

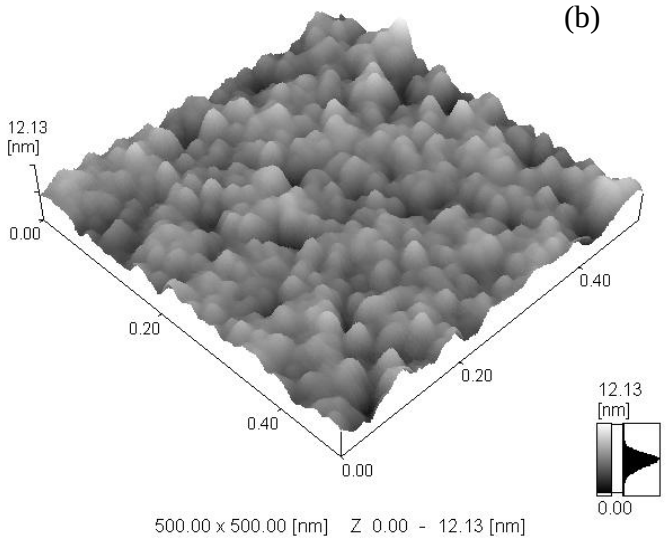

Figure 5.8: AFM images of 100 mTorr (c) 400 ^{o}C and (d) 600 ^{o}C

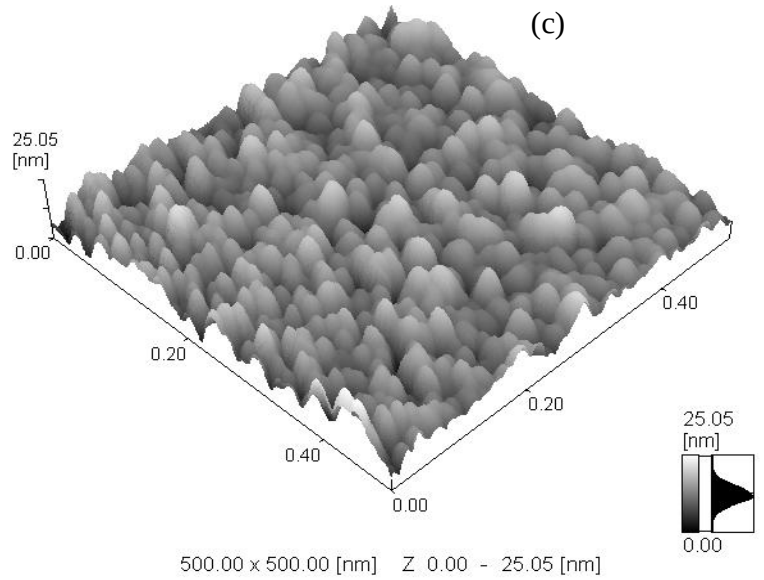

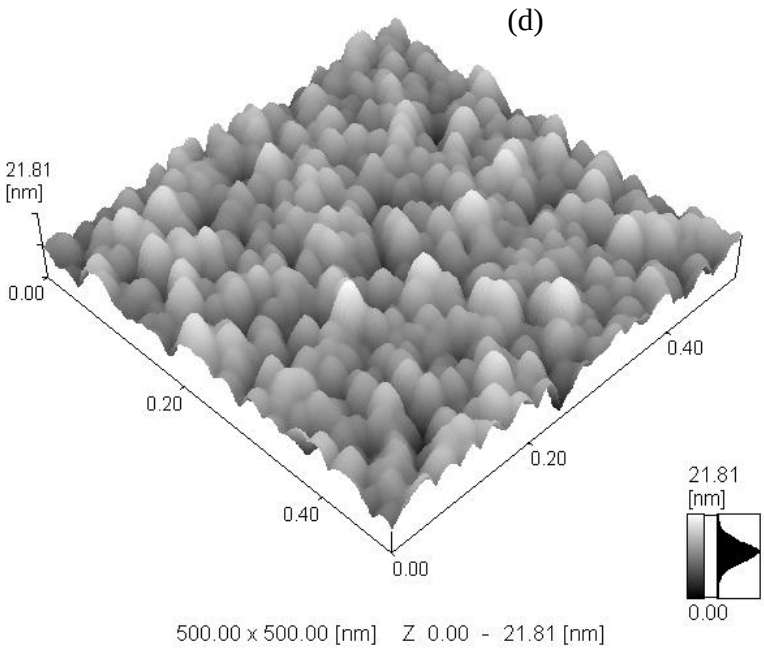

Figure 5.9: AFM images of 300 mTorr (c) 400 ^{o}C and (d) 600 ^{o}C

Figure 5.10 (a) shows the PL emission spectra of the films deposited at 100 mTorr O_2 while figure 5.11shows the film at 300 mTorr O_2 with the substrate temperature fixed at 400 and 600 ^oC during the deposition process. All the spectra consist of the main emission peak associated with the $^5D_4 \rightarrow {}^7F_5$ of Tb^{3+} at 545 nm and minor peaks at 588 nm ($^5D_4 \rightarrow {}^7F_4$) and 622 nm ($^5D_4 \rightarrow {}^7F_3$). The maximum intensity was observed for the films deposited at 600 ^oC and also for the higher oxygen pressures (smaller particles but more densely packed). The improvement in PL intensity at higher oxygen pressure is due to an increase in surface roughness. Rougher surfaces are known to reduce internal reflection at the film-substrate interface resulting in improvement of the PL intensity [15-18]. The higher intensity at higher substrate temperatures is also associated with an improvement in crystallinity [18].

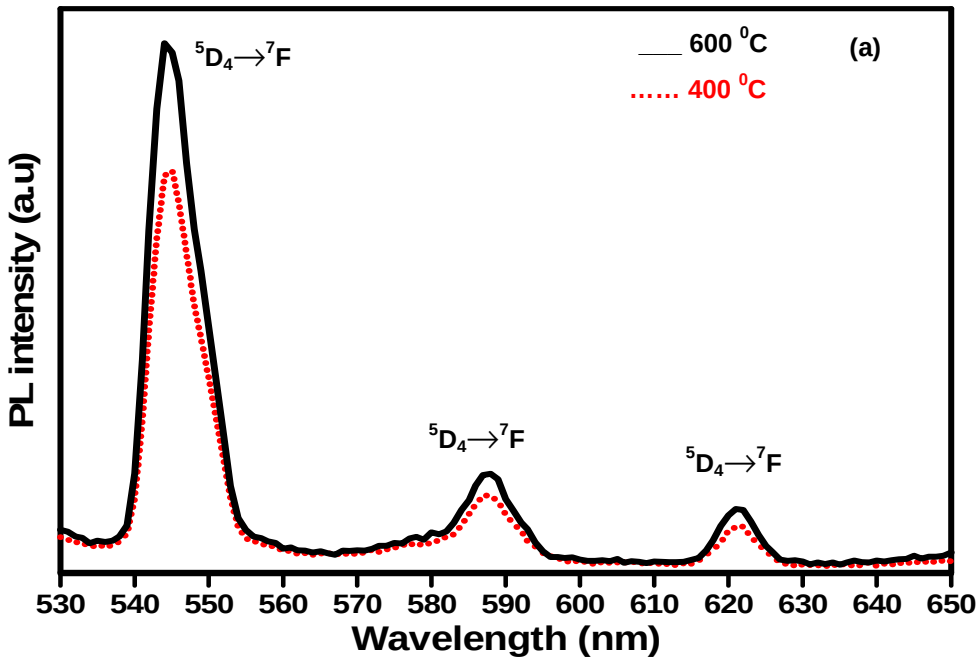

Figure 5.10: PL emission spectra of the films deposited in 100 mTorr O_2 at a substrate temperature of 400 ^oC and 600 ^oC

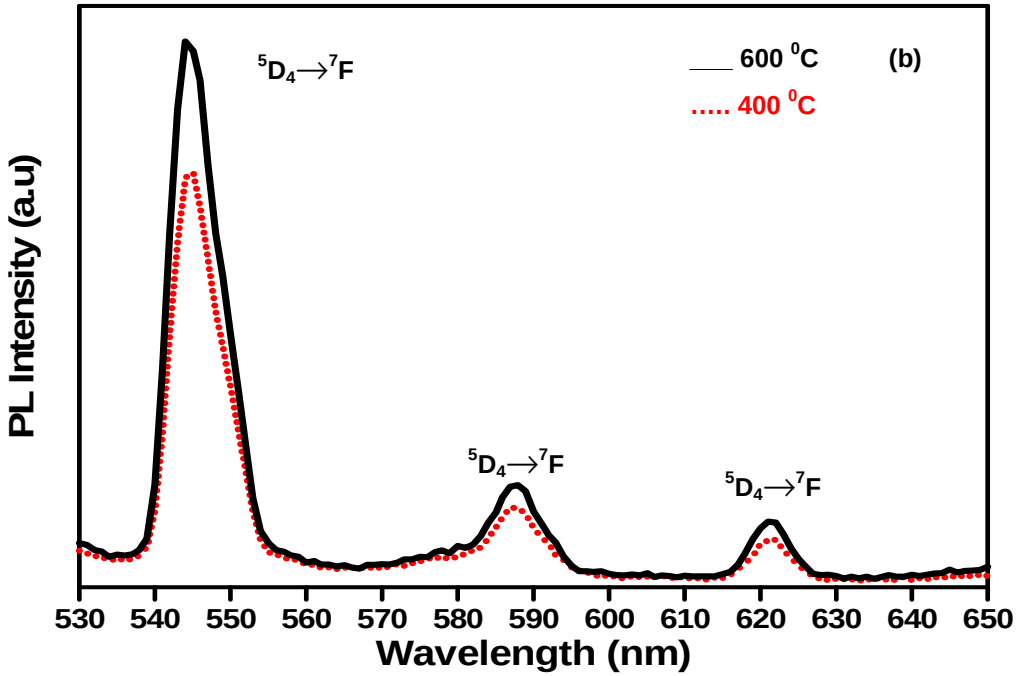

Figure 5.11: PL emission spectra of the films deposited in 300 mTorr O_2 at a substrate temperature of 400 ^{o}C and 600 ^{o}C

5.3.3 Characterization of annealed $Gd_2O_2S:Tb^{3+}$ thin films

XRD spectra from the $Gd_2O_2S:Tb^{3+}$ films deposited on Si (100) at an oxygen pressure of 900 mTorr and 700 mTorr annealed at 600 ^{o}C and 900 ^{o}C, respectively, are shown in figures 5.12 (a) and (b). The average particle size of the $Gd_2O_2S:Tb^{3+}$ films was 40 nm as calculated using the [100] peak. The diffraction data suggest that $Gd_2O_2S:Tb^{3+}$ film exhibit some amorphous and cubic structure phases. In addition these diffraction patterns illustrate that the (1 0 0) surface is the preferred oriented surface.

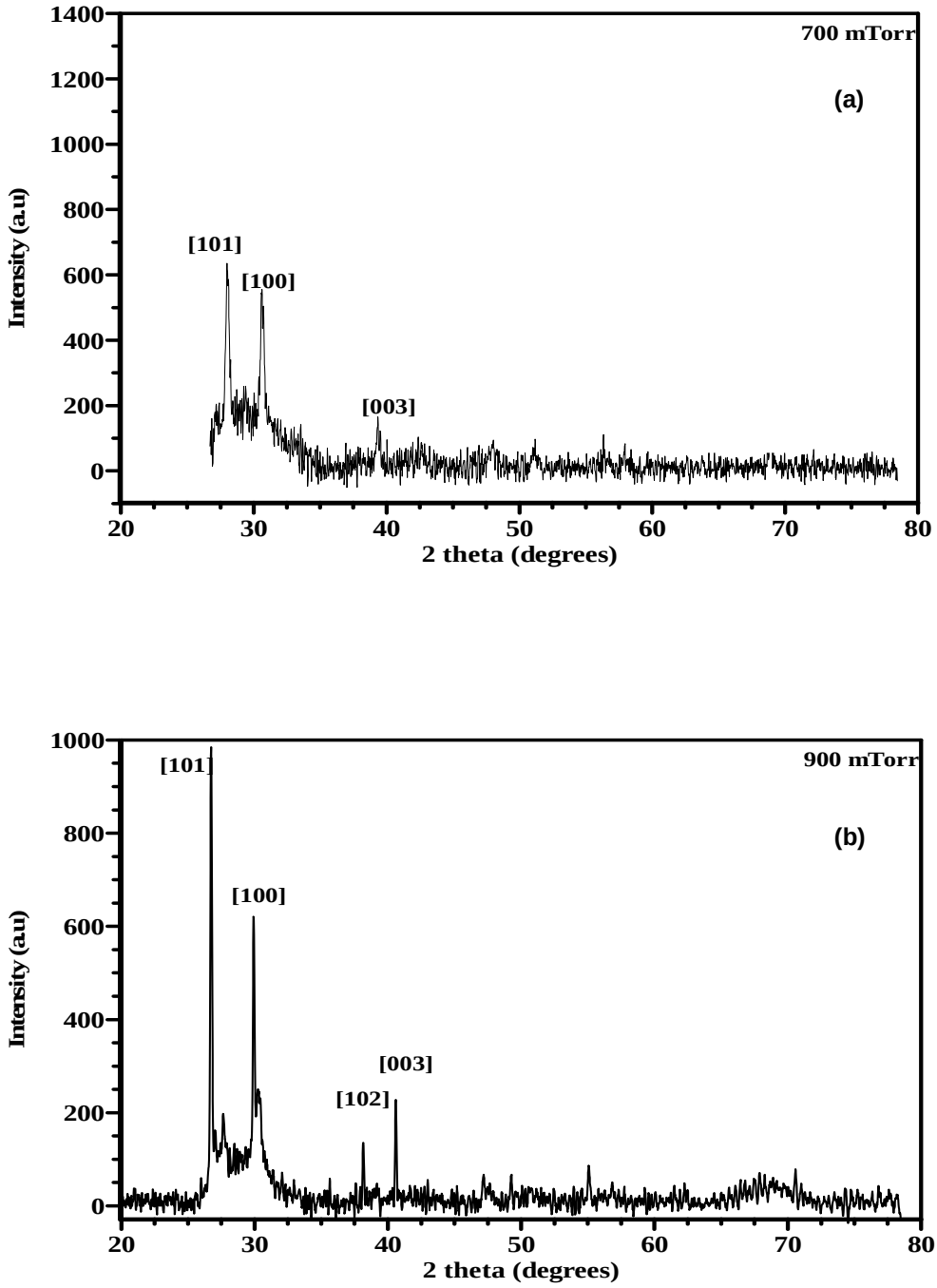

Figure 5.12: XRD patterns of the thin film at 700 mTorr and 900 mTorr (a) annealed at 600 ^{o}C with aspect ratio 1.66248:1 and (b) annealed at 900 ^{o}C with aspect ratio 1.85722:1

Figures 5.13 (a) - (b) and figures 5.14 (c) - (d) show the AFM images of the samples deposited at (a) 700 mTorr; 600 ^{o}C (b) 900 mTorr; 600 ^{o}C , (c) 700 mTorr; 900 ^{o}C and (d) 900 mTorr; 900 ^{o}C respectively. It is clear that spherical nanoparticles were deposited during the deposition process and the particle sizes increase as the annealing temperature increases. An average particle size of 45±1 nm was calculated for the film grown at higher temperatures and pressures of 700 mTorr, 900 ^{o}C and 900 mTorr, 900 ^{o}C. Recall, section 5.3.2, it discusses low pressure and temperature that the atoms do not have enough thermal energy to migrate on the substrate surface, leading to the formation of high density small nucleation sites. On the contrary, due to high surface mobility of atoms at high temperature the nucleation sites consists of high oriented crystals with large grain size, thus increasing surface roughness. It has been reported that the high O_2 pressure causes a high density of dislocations and misaligned grains at the interface [19]. The AFM images indicate that at the relatively lower temperature of 600 ^{o}C and lower O_2 pressure a better morphological structure was obtained in the initial growth stage of Gd_2O_2S film on Si (100) as seen in section 5.3.2.

(a)

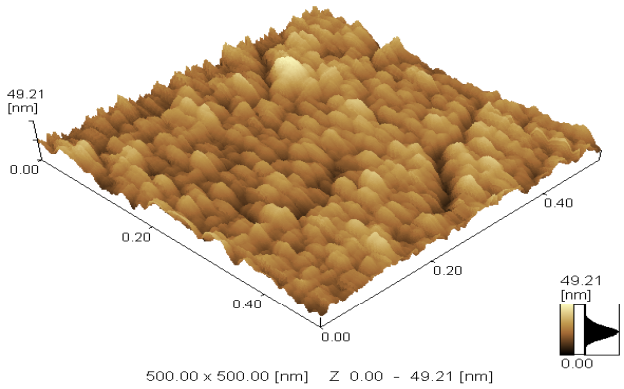

(b)

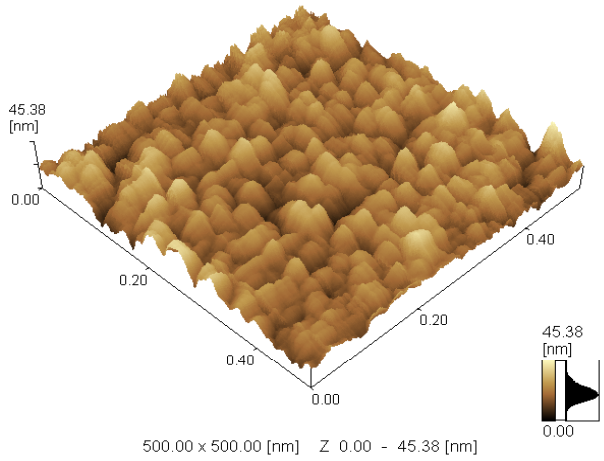

Figure 5.13: AFM images of (a) 700 mT; 600 ^{o}C (b) 900 mT; 600 ^{o}C

(c)

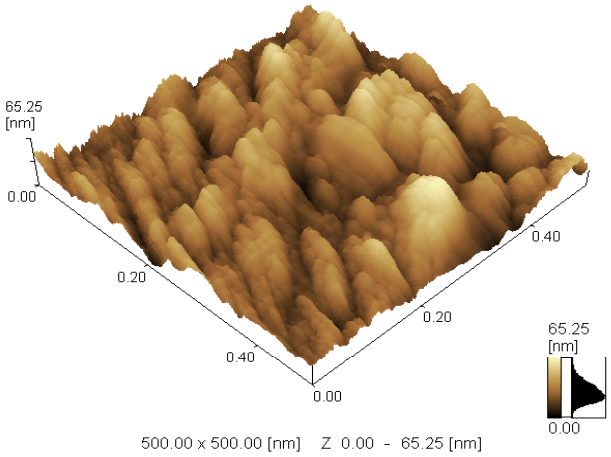

(d)

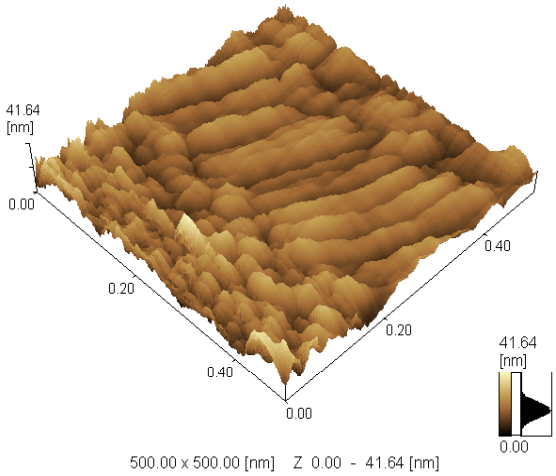

Figure 5.14: AFM images (c) 700 mTorr; 900 ^{o}C and (d) 900 mTorr; 900 ^{o}C

The SEM images of the films deposited in 700 and 900 mTorr O_2 at the substrate temperature of 900 ^oC are shown in figures 5.15 (a) and (b). It can be seen that the films grown in the higher oxygen pressures and the higher temperature of 900 ^oC have rougher surfaces compared to the lower temperature and pressures which shows smooth surface, as discussed in section 5.3.2 at the end of this chapter.

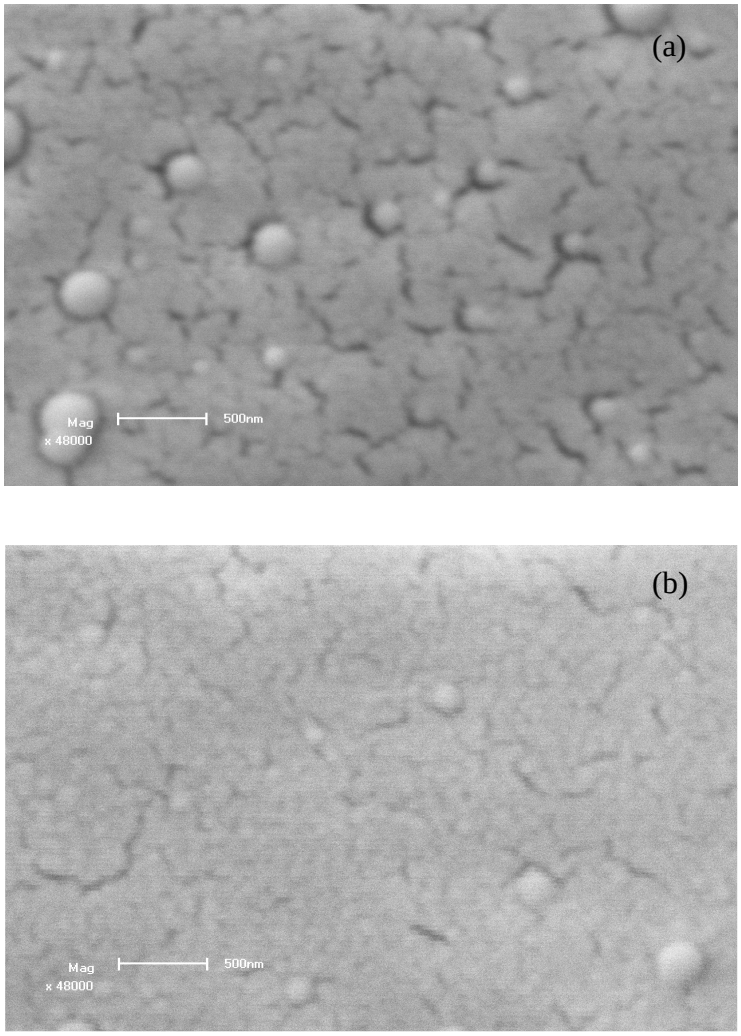

Figure 5.15: SEM images of the films deposited in (a) 900 mTorr O_2 and (b) 700 mTorr O_2 respectively annealed at 900 ^oC

Figures 5.16 and 5.17 show the PL emission and the corresponding excitation spectra of the films deposited at 700 and 900 mTorr O_2 with the annealing temperatures at 600 and 900 ^oC during the deposition process. The excitation spectra were obtained by monitoring the emission of Tb^{3+} due to the transition $^5D_4 \rightarrow {}^7F_5$ at 545 nm. It can be seen that the excitation spectrum consists of a broad intense band with a maximum at 255 nm and 275 nm whose intensity increases with the increase in annealing temperature and pressure. The increased excitation intensity may be due to the better crystallinity of the sample at higher annealing temperatures up to 900 ^oC. As discussed in section 5.3.2, all the spectra consist of the main emission line associated with the $^5D_4 \rightarrow {}^7F_5$ of Tb^{3+} at 545 nm indicating minor peaks at 585 nm ($^5D_4 \rightarrow {}^7F_4$) and 620 nm ($^5D_4 \rightarrow {}^7F_3$). The maximum intensity was observed from the films deposited at a higher pressure of 900 mTorr and high annealing temperature of 900 ^oC. The improvement in PL intensity at higher oxygen pressure is due to an increase in surface roughness, mainly because rougher surfaces are known to reduce internal reflection at the film-substrate interface resulting in an improvement in the PL intensity.

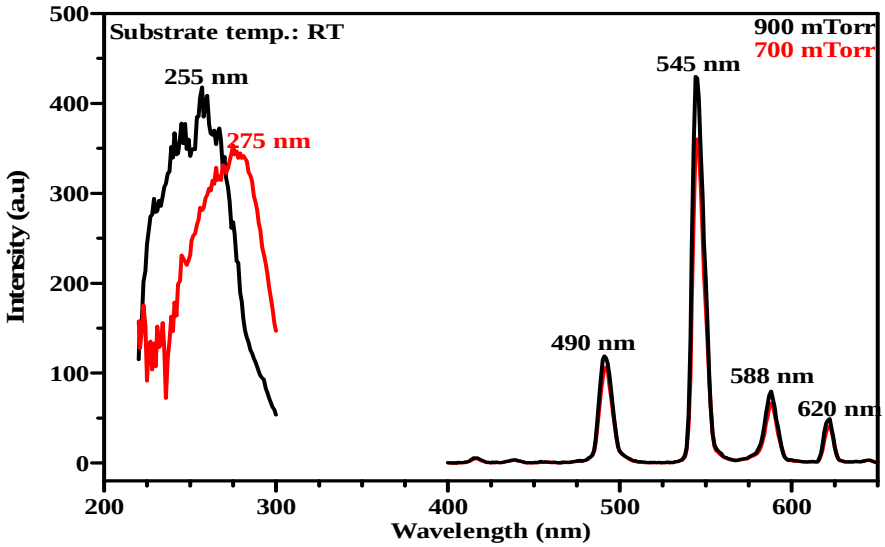

Figure 5.16: PL spectra of the films deposited in 700 mTorr and 900 mTorr O_2 annealed at 600 ^oC

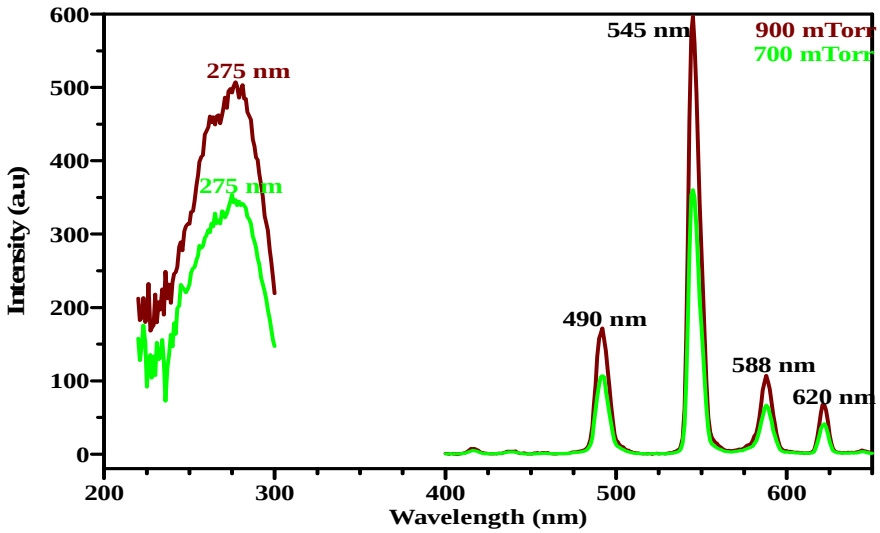

Figure 5.17: PL spectra of the films deposited in 700 mTorr and 900 mTorr O_2 annealed 900 ^oC

5.3.4 CL degradation and XPS analysis of $Gd_2O_2S:Tb^{3+}$ thin films at higher temperature and pressure

The AES spectra before and after degradation of the $Gd_2O_2S:Tb^{3+}$ are shown in figures 5.18 and 5.19. The main features of these spectra are the growth of the oxygen peak and the change in shape of the Gd low energy peaks in the 100 to 150 eV regions as discussed in chapter 4 of this thesis on the degradation of the powder phosphor. The shoulder of the 142 eV Gd peak increased and the small peak at 128 eV became more pronounced and shifted to 127 eV during the oxidation process. It is clear that a Gd_2O_3 formed in the process as confirmed by XPS in the next section. Due to overlapping of the Gd and S peaks, the Linear Least Square (LLS) technique was used, as discussed in chapter 4 in more detail, to separate the peaks [20].

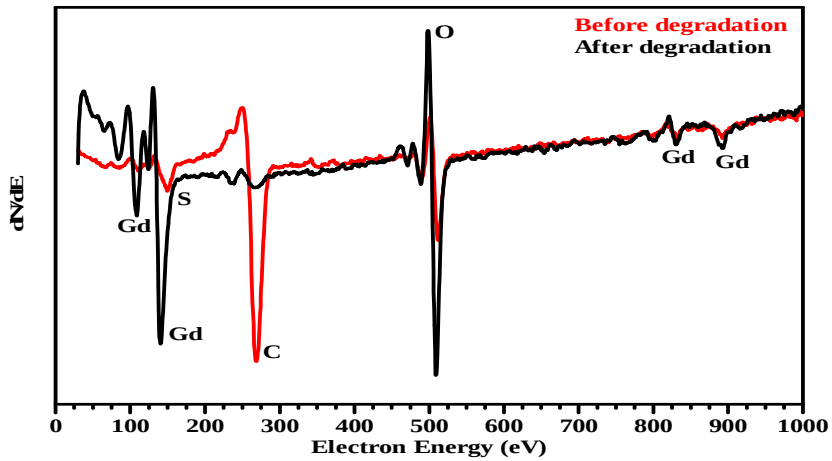

Figure 5.18: The AES spectra of the $Gd_2O_2S:Tb^{3+}$ thin film 600 ^oC, 300 mTorr before and after degradation at $1x10^{-6}$ Torr oxygen with aspect ratio 1.57632:1

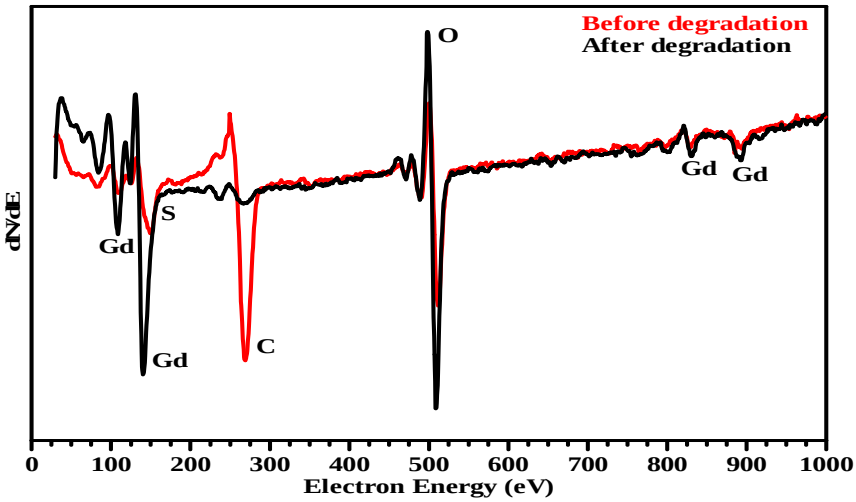

Figure 5.19: The AES spectra of the $Gd_2O_2S:Tb^{3+}$ thin film 600 ^oC, 300 mTorr before and after degradation at $1x10^{-8}$ Torr oxygen with aspect ratio 1.60321:1

Simultaneous with the change in surface concentration the CL decreased as shown in figures 5.20. The fact that the main emission peak at 545 nm in figure 5.21 did not shift from its original position during degradation suggests that exposure to the electron beam did not change the radiative relaxation process for Tb^{3+}. After degradation, the main emission peak is only 20% of the initial intensity, showing a significant reduction in the CL intensity [21].

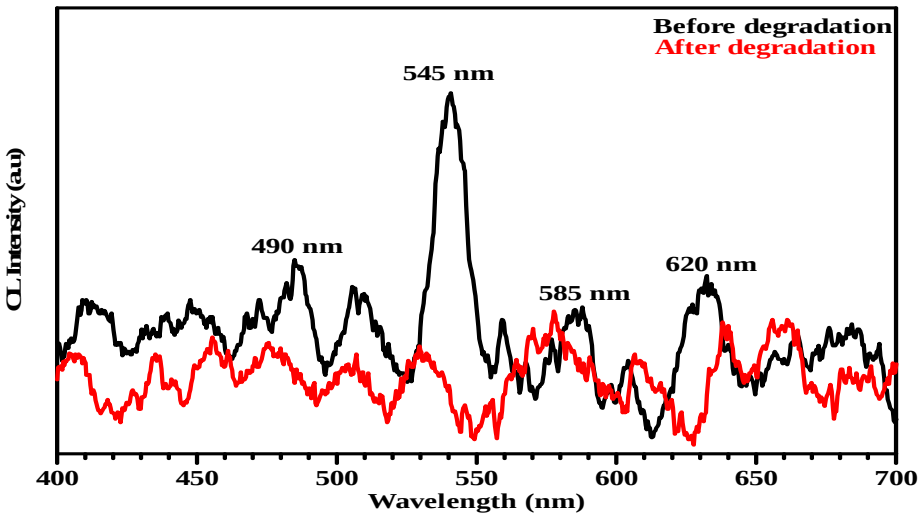

Figure 5.20: The CL spectra of the $Gd_2O_2S:Tb^{3+}$ thin film before and after degradation at $1x10^{-6}$ Torr oxygen pressure for 600 ^oC, 700 mTorr with aspect ratio 1.64341:1

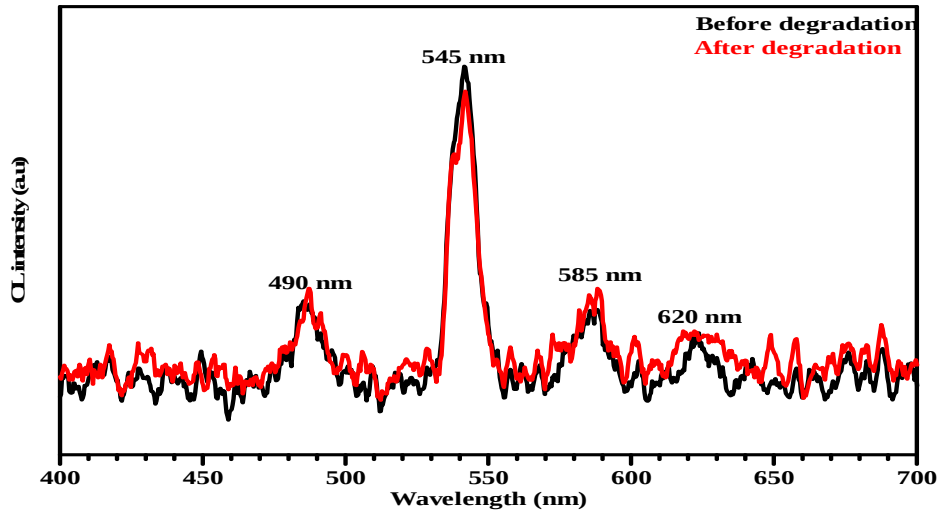

Figure 5.21: The CL spectra of the $Gd_2O_2S:Tb^{3+}$ thin film before and after degradation at $1x10^{-8}$ Torr oxygen pressure for 600 ^oC, 900 mTorr with aspect ratio 1.58126:1

Figure 5.22 shows the O1s XPS peak of $Gd_2O_2S:Tb^{3+}$ (600 ^oC; 900 mTorr) that was measured at 531.4 eV before and after degradation. The peak with a lower binding energy of 528.6 eV corresponds to Gd_2O_3 for both the degraded and undegraded samples [22]. The peak increased after degradation indicating the formation of Gd_2O_3 during prolonged electron bombardment.

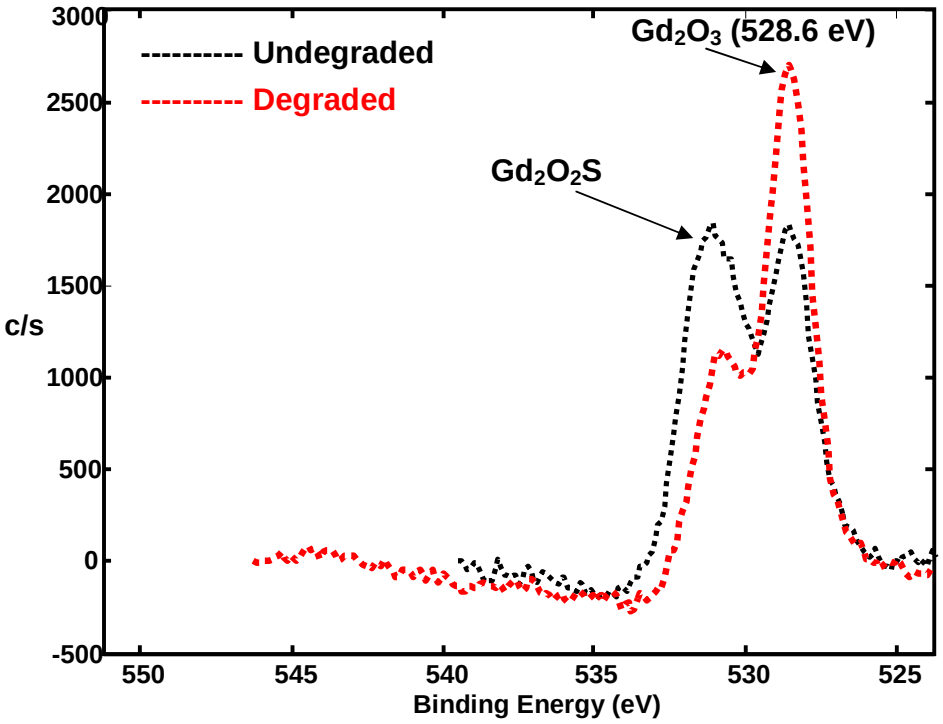

Figure 5.22: Measured XPS spectra of O 1s from the surface of the $Gd_2O_2S:Tb^{3+}$ thin film before and after degradation at $1x10^{-6}$ Torr oxygen

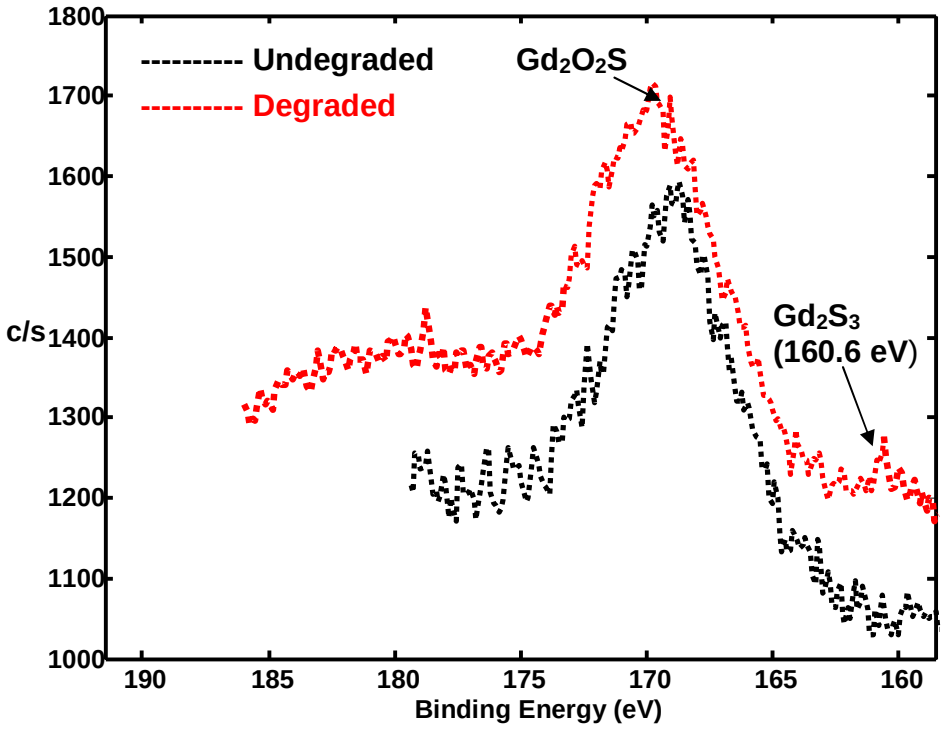

Figure 5.23 Measured spectra of S 2p from the surface of the $Gd_2O_2S:Tb^{3+}$ thin film before and after degradation at $1x10^{-6}$ Torr oxygen

The XPS measured spectra of S 2p from the surface of the $Gd_2O_2S:Tb^{3+}$ thin film before and after degradation are shown in Figure 5.23. A small new peak developed at the lower binding energy (160.6 eV) side of the main S peak during electron bombardment, which is currently ascribed to Gd_2S_3. Figure 5.24 shows the measured XPS spectra for Gd 4d obtained from the surface of the $Gd_2O_2S:Tb^{3+}$ thin film before and after degradation at $1x10^{-6}$ Torr oxygen. It can clearly be seen that the higher binding energy shoulder peak increased after degradation due to the formation of Gd_2O_3 and Gd_2S_3. It is therefore clear that chemical surface reactions are responsible for the CL intensity degradation.

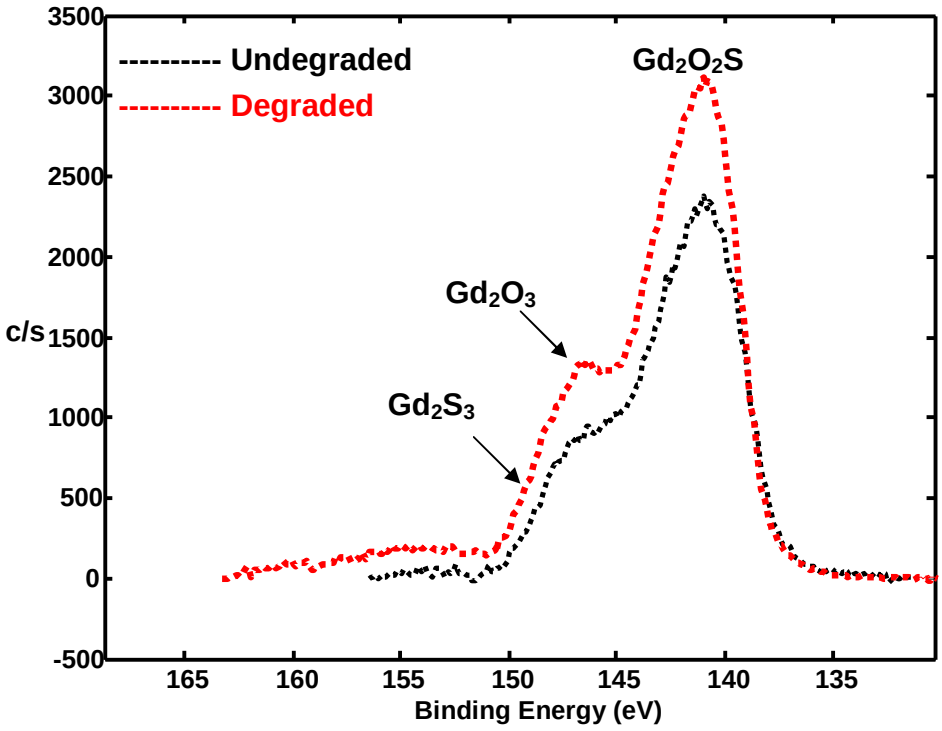

Figure 5.24 Measured XPS spectra of Gd 4d from the surface of the $Gd_2O_2S:Tb^{3+}$ thin film before and after degradation at $1x10^{-6}$ Torr oxygen

Figure 5.25, shows fitted XPS data for S 2p (a) before and (b) after degradation at $1x10^{-6}$ Torr. The main S peak is a combination of the $2p_{3/2}$ and $2p_{5/2}$ peak which could not be resolved completely. The peak at the higher binding energy (175 eV) corresponds to sulphur dioxide bondings (SO_2). A noticeable growth in these SO_2 peaks after degradation occurred, which suggest that surface reactions occurred. Some indication of Gd_2S_3 at the lower energy side of the S peak in the noise level can however not completely excluded, but these peaks could not be confirmed with the fits in the Gd peaks. Figures 5.26 show the fitted results from an XPS spectrum of the Gd 3d peaks (a) before and (b) after degradation. The Gd peak position for the Gd_2O_2S-3d chemical state was measured before and after degradation at 1186.2 eV. A noticeable increase in the Gd_2O_3 peak after degradation is obvious. This also indicates that surface reaction did occur during prolonged electron bombardment in an oxygen atmosphere.

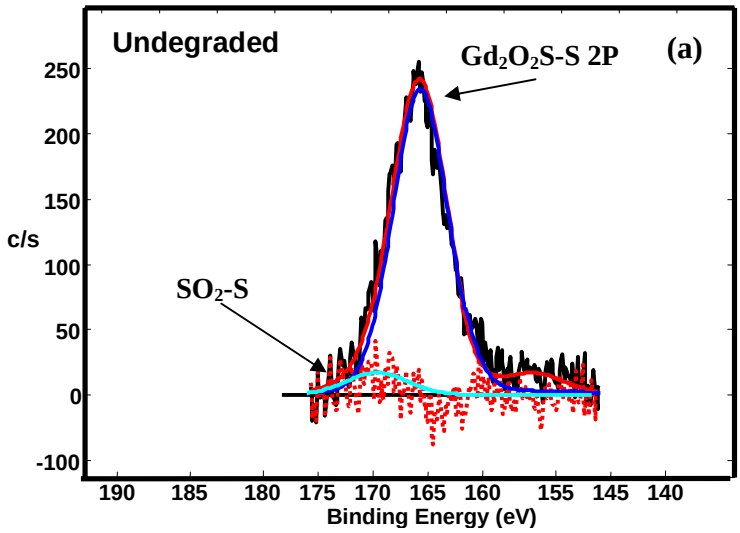

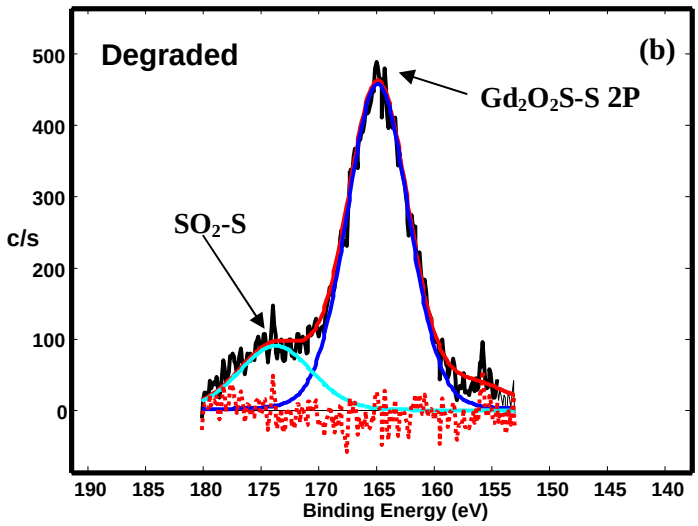

Figure 5.25 Fitted XPS for S 2p of $Gd_2O_2S:Tb^{3+}$ phosphor thin film peaks (a) before and (b) after degradation for $1x10^{-6}$ Torr

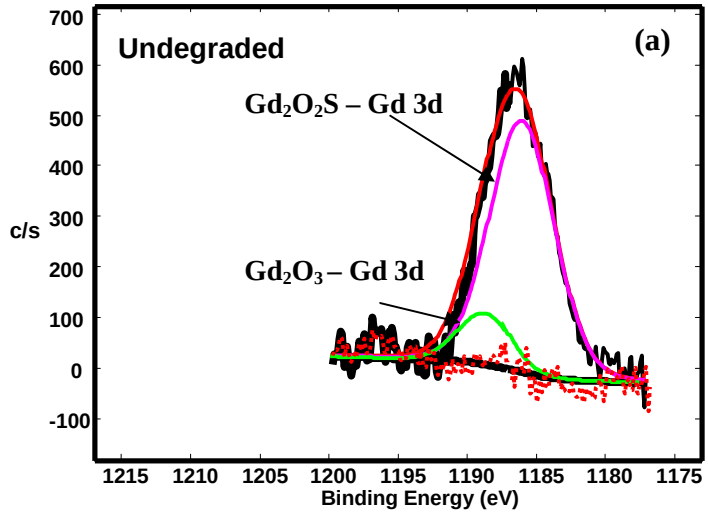

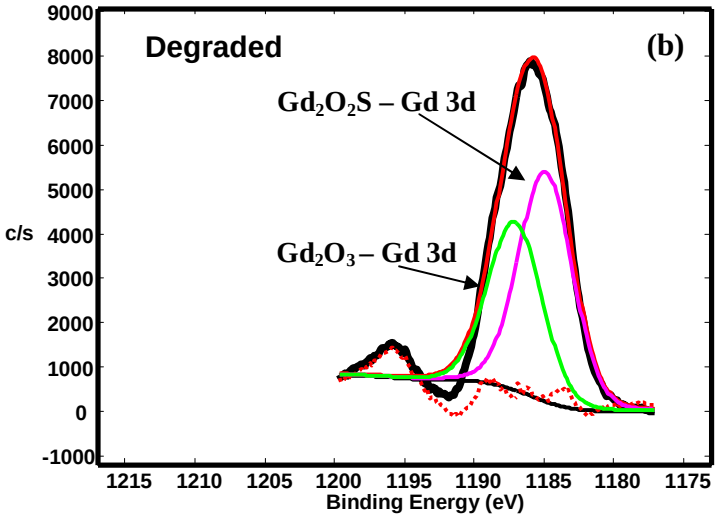

Figure 5.26 Fitted XPS for Gd 3d of $Gd_2O_2S:Tb^{3+}$ phosphor thin film peaks (a) before and (b) after degradation for $1x10^{-6}$ Torr

Figure 5.27 shows fitted XPS for O 1s peaks (a) before and (b) after degradation for $1x10^{-6}$ Torr obtained at 531.3 eV for Gd_2O_2S and 528.4 eV for Gd_2O_3. The Gd_2O_3 peak increased after degradation and it is clear that surface reactions have occurred. The extra peaks at 528.6 eV are assigned to SO_2 bondings in the matrix. The Gd_2O_3 peak increased after degradation and it is clear that surface reactions have occurred. Figure 5.28 shows Gd 4d peak position for the Gd_2O_2S-4d chemical state that was measured (a) before and (b) after degradation. Four peaks can be identified for the Gd 4d core level spectrum after deconvolution of the experimentally measured curve. Gd $4d_{3/2}$ and Gd $4d_{5/2}$ peaks of the Gd_2O_2S are located at 146.7 eV and 141.6 eV respectively which is in agreement with Datta et. al. [15] of chapter 4. Apart from above, there are two peaks measured at 142.2 eV and 147.3 eV associated with Gd_2O_3. There is also an increase in relative ratio of the peaks which also indicates that the surface reaction occurred after electron exposure. Both AES (shown previously in this section) and XPS showed a change in surface composition and a new non-luminescent surface layer of Gd_2O_3, with some indication of SO_2 bondings, which was responsible for the degradation in light intensity, formed during electron bombardment.

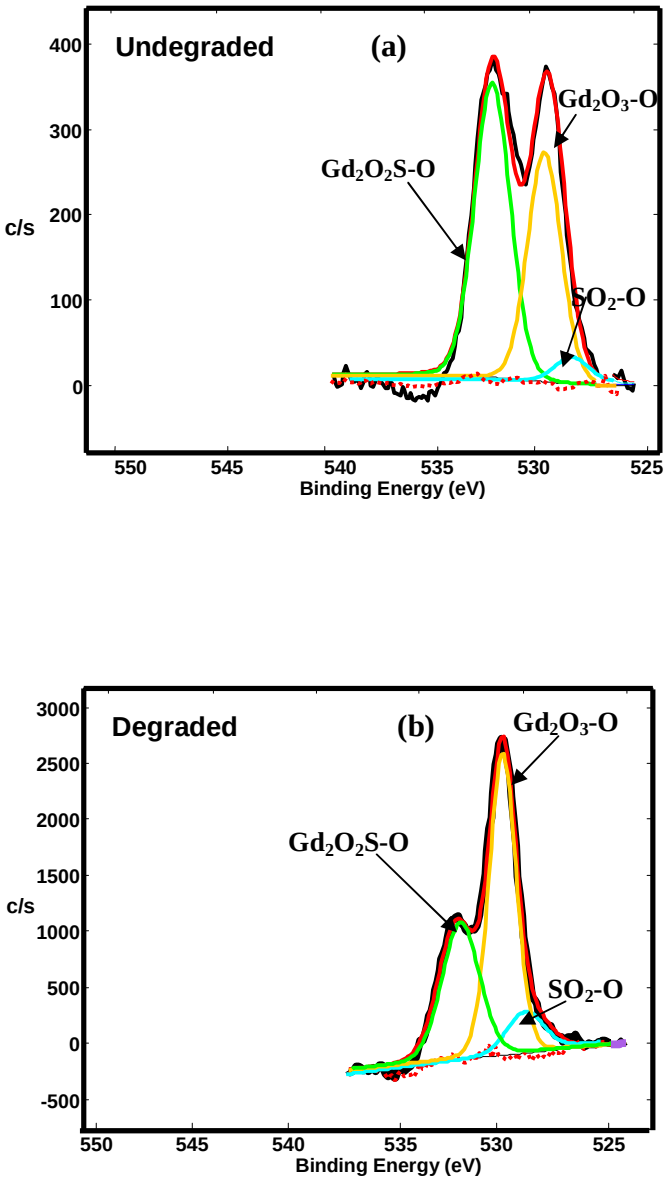

Figure 5.27: Fitted XPS for O 1s of $Gd_2O_2S:Tb^{3+}$ phosphor thin film peaks (a) before and (b) after degradation for $1x10^{-6}$ Torr

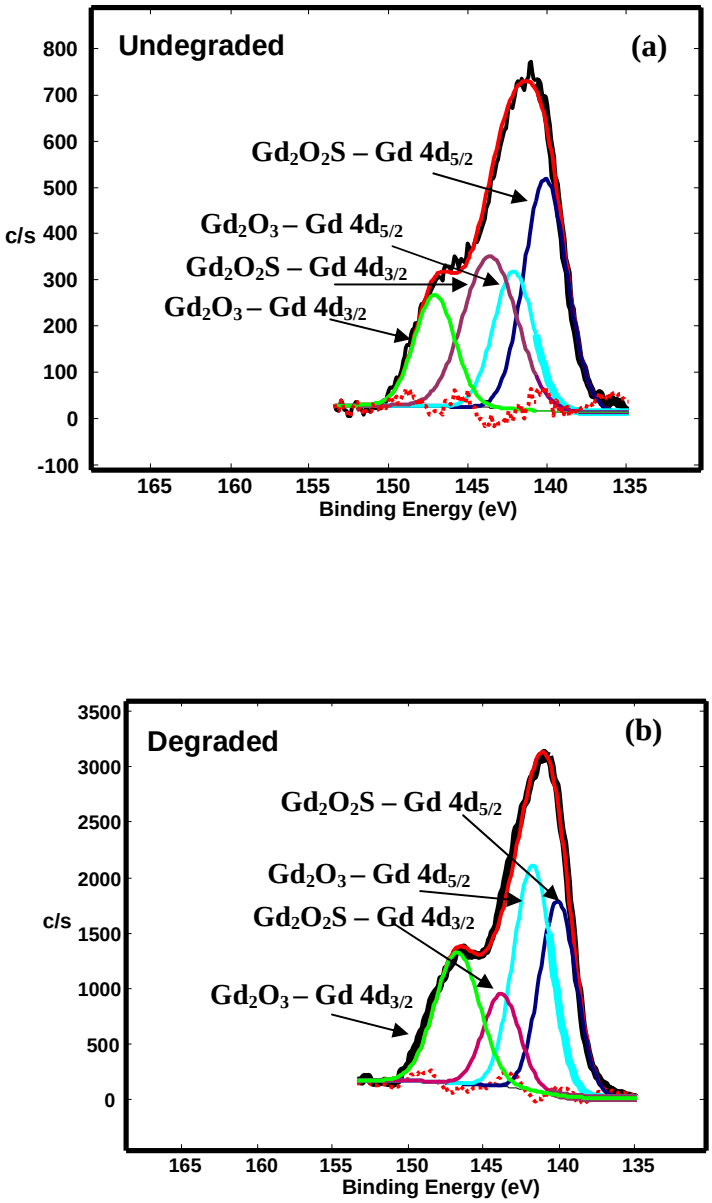

Figure 5.28: Fitted XPS for Gd 4d of $Gd_2O_2S:Tb^{3+}$ phosphor thin film peaks (a) before and (b) after degradation for $1x10^{-6}$ Torr

5.4 Conclusion

As mentioned before, luminescent $Gd_2O_2S:Tb^{3+}$ thin film phosphors were successfully grown by the pulsed laser deposition technique. The films grown in a higher O_2 ambient and higher annealing temperatures improve the PL intensity. It is clear from the AFM that spherical nanoparticles were deposited during the deposition process. Clearly from the XRD, we have seen that as the annealing temperature increases, the broadening of the peaks is reduced. The formation of an oxide layer during electron bombardment of PLD thin phosphor films were confirmed with XPS. The new non-luminescent layers of Gd_2O_3 and Gd_2S_3 that formed during electron bombardment were responsible for the degradation in light intensity. The adventitious C was removed from the surface as volatile gas species, which is consistent with the electron stimulated surface chemical reactions (ESSCR) model. $Gd_2O_2S:Tb^{3+}$ was converted to Gd_2O_3 due to ESSCRs. The effects of oxygen pressure and substrate temperature on the morphology and the PL emission intensity were investigated. The films grown in a higher O_2 ambient consist of smaller but more densely packet particles relative to the films grown at a lower O_2 ambient. The PL intensity of the films increased relatively with an increase in deposition O_2 pressure. The PL of the films grown at a higher substrate temperature was generally also more intense than those grown at a lower substrate temperature. The XPS results have proved the presence of Gd_2O_3 and Gd_2S_3 on the degraded film spots.

References

1. E-J. Popovici, L. Muresan, A. Hristea-Simoc, E. Indrea, M. Vasilescu, M. Nazariv, D.Y. Jeon, Opt. Mat., 27 (2004) 559

2. A.A. da Silva, M.A. Cebim, M.R. Davalos, J. Lumin., 128 (2008) 1165

3. S-K Kang, J-K Park, J-Y Choi, B-Y Cha, S-H. Cho, S-H Nam, Nuclear Instruments and Methods in Phys. Research A, 546 (2005) 242

4. Y. Tian, W-H Cao, X-X Luo, Y. Fu, J. of Alloy Comp., 433 (2007) 313

5. S.L. Jones, D. Kumar, K-G Cho, R Singh, P.H. Holloway, Display, 19 (4) (1999) 151

6. K.T. Hillie, C. Curren, H.C. Swart, Appl. Surf. Sci., 177 (2001) 73

7. Y. Tian, W.H. Cao, X.X. Luo, J. Chin. Rare earth Soc., 23 (2005) 271

8. H.L. Chung, M.H. Jilavi, Thin Solid Film, 388 (2001) 101

9. H.C. Swart, E. Coetsee, J.J. Terblans, O.M. Ntwaeaborwa, P.D. Nsimama, F.B.Dejene, J.J. Dolo, Appl. Phys. A, 101 (2010) 633

10. X. G. Rajan, K.G. Gopchandran, Appl. Surf. Sci. 255 (2009) 9112

11. E. Coetsee, H.C. Swart, J.J. Terblans, O.M. Ntwaeaborwa, K.T. Hillie, W.A. Jordaan and U. Butner, Opt. Mat., 29 (2007) 1338

12. G. Hodes, A. Albu-Yaron, F. Decker, P. Motisuke, Phys. Rev. B 36 (8) (1987) 36

13. M.S. Dhlamini, J.J. Terblans, O.M. Ntwaeaborwa, J.M. Ngaruiya, K.T. Hillie, J.R. Botha and H.C. Swart, J. of Lumin.,128 (12) (2008) 1997

14. D. Riabinina, F. Rosei, M. Chaker, J. Eng. Nanosci., 1 (1) (2005) 83

15. S.L. Jones, D. Kumar, P.H. Holloway, Appl. Phys. Lett., 71 (1997) 404

16. K.G. Cho, D. Kumar, S.L. Jones, D.G. Lee, P.H. Holloway, R.K. Singh, J. Electrochem. Soc., 145 (1998) 3456

17. K.G. Cho, D. Kumar, D.G. Lee, S.L. Jones, D.G. Lee, P.H. Holloway, R.K. Singh, J. Appl. Phys. Lett., 71 (1997) 3335

18. K.G. Cho, D. Kumar, P.H. Holloway, R.K. Singh, Appl. Phys. Lett., 73 (1998) 3058

19. C. Liu, S. H. Chang1, T. W. Noh1, J.-H. Song2, and J. Xie, phys. stat. sol. (b) 244, No. 5, (2007) 1528

20. J.J. Dolo, H.C. Swart, J.J. Terblans, E. Coetsee, M.S. Dhlamini,

O.M. Ntwaeaborwa, B.F. Dejene, Physica Status. Solidi C 5(2) (2007) 594

21. K.T. Hillie, O.M. Ntwaeaborwa, H.C. Swart, Phys. Stat. Sol., **C** 1 (9) (2004) 2360

22. H. Strandberg, L. Johansson, J. Electrochem. Soc. 81 (1997) 144

CHAPTER 6

Summary and Conclusion

The contents of this thesis might be divided into two main categories, namely (1) cathodoluminescence degradation of $Gd_2O_2S:Tb^{3+}$ powder and pulsed laser deposited $Gd_2O_2S:Tb^{3+}$ thin film phosphors and (2) Deposition of thin films with laser deposition.

In one set of experiments, AES and CL spectroscopy were used to study CL degradation of commercial $Gd_2O_2S:Tb^{3+}$ powder and the degradation of pulsed laser deposited thin film phosphors. Powder and thin film samples were irradiated with a 2 keV beam of electrons in a vacuum chamber maintained at 1×10^{-6}, 1×10^{-7} or 1×10^{-8} Torr O_2. The CL intensity of the samples was degraded considerably by prolonged electron beam irradiation. Among other things, oxygen-deficient non-luminescent layers of Gd_2O_3 could be responsible for the CL degradation of the $Gd_2O_2S:Tb^{3+}$ thin films and powders. A linear least squares (LLS) method was applied to resolve the peaks of Gd and S from the AES measurements. Elemental standards from Goodfellow were used in conjunction with the measured data to subtract the S and Gd peaks. A direct correlation between the surface reactions and the CL output was found. The CL decreased while the S was removed from the surface during electron bombardment. A new non-luminescent surface layer of Gd_2O_3 and Gd_2S_3 that formed during electron bombardment was responsible for the degradation in light intensity.

Luminescent $Gd_2O_2S:Tb^{3+}$ thin film phosphors were successfully grown by the pulsed laser deposition technique. The effects of oxygen pressure and substrate temperature on the morphology and the PL emission intensity were investigated.

The films grown in a higher O_2 ambient consist of smaller but more densely packet particles relative to the films grown at a lower O_2 ambient. The PL of the films grown at a higher substrate temperature was generally also more intense than those grown at a lower substrate temperature. The improvement in PL performance was not only from the change of crystalline phase leading to higher oscillating strengths for the optical transitions, but also reduced internal reflections of the emitted light due to rougher surfaces.

FUTURE PROSPECTS

The work presented in this thesis suggests that we have to understand the degradation phenomenon of oxide phosphors, it is important to do more experiments under different conditions. This include degrading in different gas mixtures (i.e. H_2, H_2O, CO_2), which are usually present in vacuum chambers and are known to influence degradation behavior of FED phosphors. It is important to investigate further why degradation behavior of $Gd_2O_2S:Tb^{3+}$ powders and $Gd_2O_2S:Tb^{3+}$ thin film phosphors is different, i.e. why does oxygen desorbs from the surface in the case of thin films and powders. Since mechanisms presented in this study about the correlation between desorption of oxygen from the surface and the decrease of CL intensity are based on speculations, it is imperative to do more experiments and monitor constantly the rate of desorption of oxygen and that of decrease of CL intensity during electron beam bombardment. This could help in developing a reasonable model to explain this correlation. Samples with different particles sizes and shapes must be prepared in order to determine the effects of size and shape on cathodoluminescence degradation as well as cathodoluminescence and photoluminescence intensity. Further future prospects must include the luminescence properties of $Gd_2O_3:Eu^{3+}, Tb^{3+}$ thin films produced by either sol-gel or solid state reaction techniques. An extensive research needs to be done to investigate between powders and thin films that which one has higher

efficiency for energy transfer from host to co-dopant. Transmission electron microscopy study must be conducted in order to determine particle sizes of Gd_2O_3:Eu^{3+}, Tb^{3+} thin films.

Thermo-luminescence (TL) is one of the most useful methods to study the trap level in long-lasting phosphors; and the measurement of the TL curves could reveal some new facts about the persistent luminescence mechanisms as a result there is a need to study that technique on phosphors. One most important technique is the Rutherford backscattering spectrometry (RBS), which is an analytical technique used in materials science, RBS is used to determine the composition of materials by measuring the backscattering of a beam of high energy ions impinging on a sample or the film thickness. Further future work could also include investigating the effect of temperature and a different ambient gas pressure (for example CO_2, etc.) on the CL intensity of both the powders and thin films, as it will contribute to the environmental effects for operation in the FEDs.

Other future work is to look in to Mössbauer effect on phosphor powder and thin films. If we succeed we need to look at the following:

The barium magnesium aluminates (BAM) phosphor activated by divalent europium ions BAM continues to be a subject of great interest in the fluorescence community because of its importance as an efficient blue-emitting phosphor. However, its relative instability in a variety of lamp-related processing conditions and also during the lamp life continues to be a major concern. A better alternative to this blue-emitting phosphor has yet to be developed. Therefore, a great deal of attention is focused worldwide on understanding the underlying mechanisms of various degradation processes. It is hoped that such an understanding could help in improving the maintenance of this phosphor, as a result we need to investigate the degradation of $BaMgAl_{10}O_{17}$:Eu^{2+} phosphor using cathodoluminescence and ^{151}Eu Mössbauer.

PUBLICATIONS

1. **J.J. Dolo**, H.C. Swart, J.J Terblans, E. Coetsee, M.S. Dhlamini, O.M. Ntwaeaborwa and B.F. Dejene, Degradation of commercial Gd_2O_2S:Tb phosphor. *Physica Status Solidi C, 5 no 2* (2008) *594-597*
2. H.C. Swart, E. Coetzee, J.J. Terblans, O.M. Ntwaeaborwa, P.D. Nsimama and **J.J. Dolo**, Cathodoluminescence degradation of PLD thin films, Applied Physics A, 101 (2010) 633-638
3. **J.J. Dolo**, O.M. Ntwaeaborwa, J.J. Terblans, E. Coetsee, B.F. Dejene, M-M Biggs and H.C. Swart, The effect of oxygen pressure on the structure, morphology and photoluminescence intensity of pulsed laser deposited $Gd_2O_2S:Tb^{3+}$ thin film phosphor, Applied Physics A, 101 (2010) 655-659
4. H.C. Swart, J.J. Terblans, E. Coetsee, V. Kumar, O.M. Ntwaeaborwa and **J.J. Dolo**, Auger electron spectroscopy and X-ray photoelectron spectroscopy study of the electron-stimulated surface chemical reaction mechanism for phosphor degradation, Surface and Interface Analysis, **Volume 42 Issue 6-7,** (2010) 922 – 926
5. **J.J. Dolo**, H.C. Swart, E. Coetsee, J.J. Terblans, O.M. Ntwaeaborwa and B.F. Dejene, XPS analysis and luminescence properties on the deposited thin films obtained by using Pulsed Laser Deposition, *Hyperfine Interact (2010)197:129-134*
6. J. Z. Msomi and **J. J. Dolo,** Heat treatment effects on spinel phase of $Zn_xNi_{1x}Fe_2O_4$ and $MnFe_2O_4$ nanoferrites, *Hyperfine Interact (2010)197:59-64*
7. J. Z. Msomi, H. M. I. Abdallah, T. Moyo and **J. J. Dolo,** Mössbauer and magneticstudies of bulk and nanophase $Mn_{0.1}Sr_{0.2}Co_{0.7}Fe_2O_4$ ferrites, 12^{th} Latin American Conference on the Applications of the Mössbauer Effect (LACAME 2010), to be held November 7^{th} - 12^{th}, 2010 in Lima, Peru, *Hyperfine Interactions submitted November 2010*

INTERNATIONAL CONFERENCES

1. Conference on Photonic Materials, Kariega Game Reserve, South Africa, 2-6 May 2007
2. International Conference on Nanotechnology and Advanced materials , 4th 7th may 2009, University of Bahrain, Bahrain
3. 13th European Conference on Application of Surface Analysis, 18th 23rd October 2009, Turkey
4. 10th International Conference on Laser Ablation, 22nd -27th November 2009, Singapore
5. International Conference on Hyperfine Interactions (under, Surfaces, Interfaces, Thin Films, Nano-structures), 13-17 September 2010, Geneva, Switzerland
6. 12th Latin American Conference on the Applications of the Mössbauer Effect (LACAME 2010), November 7th - 12th, 2010 in Lima, Peru

NATIONAL CONFERENCES

1. 48th South African Institute of Physics, 23-26 June 2003, University of Stellenbosch (Cape Town), "Polymer electrolyte Membrane Fuel cells using Molecular Dynamics Simulation Techniques" J.J. Dolo, P.E. Ngoepe and L. Ackermann.

2. 49th SAIP, June/July 2004, University of the Free State, Bloemfontein, Computational studies of polymers and penetrants by MD simulation study, J.J. Dolo, P.E. Ngoepe and L. Ackermann.

3. 50th SAIP, June/July 2005, University of Pretoria, Pretoria, “Molecular Modelling of Polymer electrolyte membrane fuel cells”, J.J. Dolo, P.E. Ngoepe and L. Ackermann.

4. 52nd SAIP, June/July 2007, University of the Witwatersrand, Johannesburg, Degradation of commercial Gd_2O_2S:Tb phosphor, J.J. Dolo, H.C. Swart, J.J Terblans, O.M. Ntwaeaborwa and E. Coetsee.

5. 53rd SAIP 8-11 July 2008, University of Limpopo, Polokwane, Characterizations of thin film phosphor, J.J. Dolo, H.C. Swart, J.J. Terblans, O.M. Ntwaeaborwa and E. Coetsee.

6. 54th SAIP June/July 2009, University of Kwazulu-Natal, Durban, Characterization and CL degradation of thin film phosphor of Gd_2O_2S:Tb, J.J. Dolo, O.M. Ntwaeaborwa, J.J. Terblans, E. Coetsee, B.F. Dejene, M-M Biggs, H.C. Swart

BIOGRAPHY

Jappie Jafta Dolo was born in (Mokopane) in the Limpopo Province and he grew up at Sandsloot, Republic of South Africa (RSA). He joined the University of the North in 1996 as a student and obtained his MSc degree in Physics in 2001. He was appointed as a Physics Lecturer at the University of the Free State (QwaQwa campus) in February 2006 and registered as a PhD student at the main campus (Bloemfontein).

Jappie Jafta Dolo has published four articles in internationally accredited journals.

He is an upcoming researcher working on luminescent nanoparticle materials for flat panel displays. The growth plan of his research is to explore optical, luminescent properties of thin films phosphor and Mossbauer effect. This work will be done in collaboration with Prof. H.C. Swart (Department of Physics, University of the Free State) and Dr. J.Z. Msomi (Department of Physics, UFS) respectively.

Jappie Jafta Dolo is the grant holder of the Thuthuka Programme from the NRF.